NANOSTRUCTURED GRAPHENE ON Si-TERMINATED SiC AND ITS ELECTRONIC PROPERTIES

A Thesis
Presented to
The Academic Faculty

by

Yuntao Li

In Partial Fulfillment
of the Requirements for the Degree
Doctor of Philosophy in
Physics

School of Physics
Georgia Institute of Technology
May 2016

NANOSTRUCTURED GRAPHENE ON Si-TERMINATED SiC AND ITS ELECTRONIC PROPERTIES

Approved by:

Professor Phillip N. First, Advisor
School of Physics
Georgia Institute of Technology

Professor Markus Kindermann
School of Physics
Georgia Institute of Technology

Professor Zhigang Jiang
School of Physics
Georgia Institute of Technology

Professor Edward H. Conrad
School of Physics
Georgia Institute of Technology

Professor Thomas Orlando
Department of Chemistry
Georgia Institute of Technology

Date Approved: February 29th, 2016

To my parents,

Lixin Li & Jinghui Xia,

to whom words always fail to convey my indebtedness and love

ACKNOWLEDGEMENTS

Looking back at my life over the past five years, I begin to perceive that the endless list of individuals I have relied on and gained help from goes well beyond the limited words in this paragraph. I would like, however, to attempt thanking at least some of them who offered the most mentoring, sparked the most inspirations, and devoted the most love to me. The first and foremost gratitude goes to my wonderful advisor Dr. Phillip N. First. I have learned so much from his amazing expertise in solid state and semiconductor physics, unbounded knowledge in every aspect of UHV instrumentation and electronic circuits, as well as surprising elegance in computer programming. I truly appreciate his availability for always being there to explore the problems we have and go through the nuts and bolts of every experiment, his patience and guidance in refining my experimental skills and academic knowledge, and his openness to all possible creative solutions and even trials and errors. Dr. First's passion about science and strictness about measurements will continue to impact me not only in conducting academic research, but also shaping my attitudes towards life. With reasons above and beyond, I feel extremely honored to stand among one of his students.

My sincere gratitudes are also due to other faculty members that have guided and inspired me in various ways. I thank Dr. de Heer for his pioneering leadership in the MRSEC program to provide so many insights in the field of graphene, Dr. Berger for her tremendous help in utilizing the resources in the Keck's Lab, Dr. Conrad for sharing his discoveries and fruitful discussions, Dr. Jiang for his constant guidance and support in studying many of the novel materials, Dr. Orlando and Dr. Kindermann for their precious time and efforts spent serving as my committee and revising my thesis. Undoubtedly, this thesis would not be possible without the selfless assistance and collaboration through my colleagues. Special thanks to my extraordinary former and present lab mates, Dr. D. Britt Torrance, Tien Hoang, Louis Wu, Di Chen, and Zachery Enderson, lab work becomes so much fun with your extra hands and laughters. Gracious additional thanks to Dr. Yike

Hu, Dr. James Palmer, Dr. Lede Xian, Dr. Zelei Guo, Dr. Sonam Sherpa, Dr. Wenlong Yu, Dr. Feng Wang, Dr. Lei Ma, Meredith Nevius, Matthew Conrad, and Jean-Philippe Turmaud, learning and working with you are my greatest pleasure.

But of course, this long yet rewarding journey is only more colorful and meaningful in the presence of my lovely friends. I did feel a sense of home and will forever grave on my mind those good old days with you all, in no particular order — Patrick Gartland, Wenchao Jiang, Keenan Zhuo, Giz Kaev, Shangguo Zhu, Chen Yang, Xiaofeng Meng, Feifei Qian, Chao Shi, Ruomeng Yu, Chang Liu, Cong Qiao, Lin Li, Xingjian Wang, Anshuman Vinit. Especially, I thank Niao He, for being there, holding my hands, and making me complete.

And lastly, to my family, who have been supporting me and nurturing me ever since I have come to this world, I want to express my heartfelt gratitude. I want to thank Uncle Jeffrey Tung and Aunt Jean Xia, for being my guide and role model. I want to thank my most loving and caring parents, who have poured themselves out all life long so that I would have opportunities that they could not, you deserve everything and anything I could do for you. May god bless you, forever ever.

This work was supported in part by the National Science Foundation through grants DMR-1106131 and DMR-0820382 [MRSEC].

TABLE OF CONTENTS

LIST OF TABLES

LIST OF FIGURES

SUMMARY

Graphene has been considered as a possible alternative to silicon in building the next generation electronic devices. The one atom thick carbon material is mechanically stronger, electronically superior, and chemically more stable than most materials used in the modern electronics. Despite the various technological hurdles to be overcome, numerous advances have been made in theoretical investigations of this low dimensional system, large scale graphene production, as well as novel graphene-based transistor design. Therefore, there is a reason to believe that graphene can play a key role in the future semiconductor industry.

Graphene's unique linear band structure at low energies suppresses carrier back scattering, thus leading to large coherence length and high carrier mobility; however it lacks a band gap, which greatly hinders the material's potential application in digital electronics because the on/off ratio of such devices would be extremely low. Quantum confinement in graphene nanoribbons is a possible means to introduce a band gap into graphene, but conventional lithography creates atomically rough edges, which degrades the mobility. Epitaxial sidewall graphene nanoribbons (GNR) grown on SiC provides a promising approach to overcome this issue in that it is a naturally confined graphene system with high degrees of freedom for tuning and has shown tremendous transport properties when transplanted into real electronic devices.

In this thesis, we study graphene nanoribbons by utilizing both nano-lithography and natural step bunching to control the step morphology of the SiC(0001) surface in order to guide the growth of graphene which initiates at step edges, and study their respective characteristics. With scanning tunneling microscopy and spectroscopy (STM/STS), we explore the local atomic and electronic structures of the graphene nanoribbons down to atomic scale. It is found that nanoribbon formation depends critically on nanofacet orientation, nanofacet density, and growth conditions. Under some conditions, nanoribbons grow predominantly on the nanofacet. Significant electronic density-of-states features, resolved by

STS, are found to depend strongly on proximity to strained graphene near the step edge. Experimental results are compared to Molecular Dynamics simulations to better understand the origin of the discrete electronic states.

CHAPTER I

INTRODUCTION TO GRAPHENE

1.1 Motivation

Silicon has dominated the semiconductor industry in the past few decades, producing highly integrated and fast speed electronic devices. However, the ever-growing demands of low power consumption and high density for electronic devices such as mobile and wearable products in recent years has put the future of silicon-based devices into great doubts [1]. More precisely, as the density and complexity of the integrated circuits increase, physical size limit, heat consumption, as well as quantum interference all serve as fundamental barriers that are difficult to overcome. The foreseeable failure of Moore's Law has prompted people to search for alternative materials with excellent electronic/thermal transport characteristics and unique quantum properties to be directly exploited in transistor/interconnect design.

Various novel materials have been proposed to succeed silicon as electronic materials [2, 3], III-V compound semiconductors, topological insulators, 2D materials, just to name a few. Among all the alternates, graphitic carbon materials stand out as a highly promising candidate due to their natural abundance, easy production, and unique physical and chemical properties. As the thinnest graphitic material, graphene has attracted tremendous scientific interests since its first isolation from graphite in 2004. By far, people have developed multiple ways to isolate the material [2, 4], room temperature ballistic transport is achieved in graphene [5], its unique optical and mechanical properties are also actively explored [6, 7]. Over the past ten years, graphene-related publications has boomed from 161 in 2004 to over $18,000$ in 2014

Moreover, being called the wonder material, graphene is already seeking it's way into people's lives. Applications in sporting equipment, batteries, and flexible electronics etc. are readily available; biological sensors, LED lighting devices and numerous other products are also rolling out in the next few years. Semiconductor giants like Samsung [8]

and IBM (sensors/transistor) recently announced breakthroughs in wafer-scale high quality graphene production, bringing graphene one big step closer to large-scale commercialization. European Commission has established the Graphene Flagship Project [9] with 1 billion investment to facilitate graphene-related research. Institutions around the world including Bill & Melinda Gates Foundation, Sony, and Sandisk are also actively investing billions of dollars in graphene-based products and equipment.

With all the excitement about the potential of graphene, there are however two main roadblocks in the way [10]. On one hand, it is unclear yet how to achieve large scale graphene production without compromising the intrinsic high mobility. Epitaxial Graphene grown on SiC is considered a promising route to address this issue, but detailed understanding of microscopic morphologies/properties of epitaxial graphene such as step bunching and edge smoothness with respect to different growth conditions remain controversial. On the other hand, a reliably successful way of band gap engineering has not been developed. While quantum confinement by various geometric configurations such as graphene nanoribbons is able to impose band gaps up to 0.5 eV [11, 12], it remains a question as to how this behavior can be exactly controlled and what will happen to the electronic transport properties of the material.

In this thesis we try to investigate both the morphological and electronic properties of epitaxial graphene formed on SiC(0001) in a nanoribbon configuration, in the hope of understanding the different GNR formation methods and how they will alter the transport characteristics in such systems. Chapter.2 explains the main experimental techniques involved in this study, namely Scanning Tunneling Microscopy (STM), Auger Electron Spectroscopy (AES), and Low Energy Electron Diffraction (LEED). The basic theory and experimental implementation will be covered to facilitate later discussions. Chapter.3 will focus on analyzing and understanding the experimental results obtained from GNRs grown in different ways. I will show that GNRs form differently along different step directions and different sample preparation methods also changes the overall topography of GNRs. In order to understand the electronic behavior as probed by Scanning Tunneling Spectroscopy (STS), one has to take into account the various components present in the system, including

quantum confinement, local doping, and non-uniform strains. Experimental data are also compared to theoretical simulations for further investigations. Lastly, Chapter.4 summarizes the findings in this work and outlines possible future directions to gain more insights into the epitaxial graphene nanoribbon system.

1.2 What is Graphene

Graphene is not a normal material, just like the sole element that leads to its existence - carbon. As one of the most abundant chemical elements on earth, carbon has been studied for hundreds of years and a handful of various forms of carbon have been discovered and synthesized. Diamond, graphite, amorphous carbon, and fullerene are just some of the well known allotropes of carbon. Carbon has an atomic number 6 meaning that the corresponding 6 electrons span between $1s$ and $2p$ atomic orbitals ($1s^2 2s^2 2p^2$). Such electron configuration equips the element with an affinity for bonding with other small atoms, including other carbon atoms. In fact, it is the strong covalent bonding carbon tends to form with other elements that primarily explains its ubiquity on our planet. However, carbon's electron configuration does not always stay the same, which can actually interact differently with other species under different chemical environment leading to hybridized orbitals including sp^3, sp^2, and sp. The sp^2 hybridization is a particularly interesting form in that it groups electron orbitals into two types, namely the σ orbital and the π orbital, which directly alters the electronic structures of materials and leads to unique macroscopic properties. More concretely, sp^2 hybridization in carbon promotes one of the $2s$ electron into the last empty $2p$ orbital resulting in four half-filled states. Such electron rearrangement further triggers combinations of the four states that eventually form 3 identical sp^2 orbitals and 1 remaining p orbital. The 3 sp^2 orbitals, when one carbon atom concatenates with another, forms planar σ bonds that are 120° separated from each other while the last p orbital extends perpendicular to this plane and overlaps with the neighboring p orbitals forming π bonds. Electrons in the σ bonds are covalently tied to the host atom and are only shared with the nearest neighbors, thus do not overlap as much as the electrons in π bonds, which are loosely bound to the atom and can easily tunnel to other neighboring

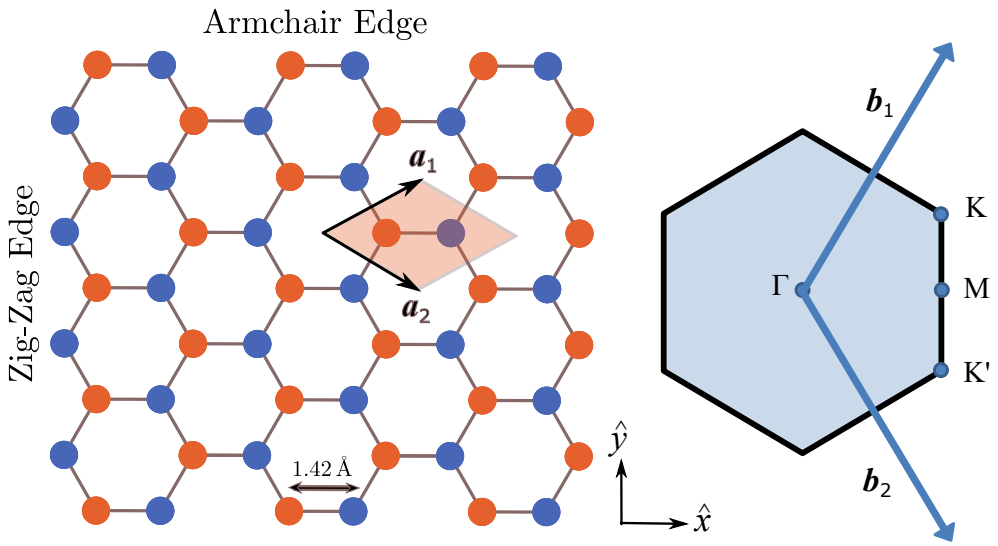

Figure 1: Graphene lattice (left) and its first Brillouin zone (right) in reciprocal space.

atomic sites.

Graphene is a special form of sp^2-hybridized carbon. With the atoms hexagonally arrayed together forming a 2-dimensional network, graphene is an atomically thin material that are solely made of carbon. Graphene is not the only appearance of sp^2-hybridized carbon, which in fact includes buckminsterfullerene, graphite, and carbon nanotubes. Despite of being discovered much earlier than graphene, such materials are all considered derivatives of graphene since they can be formed by wrapping, stacking, or rolling of the one-layer carbon material.

Studies on graphene date back to 1947 when Wallace [13] first treated a single-layer graphite problem with tight-binding calculations and showed its potential unique band structures. After almost 60 years, electrical transport was finally measured in graphene [14, 15], and in 2010, the Nobel committee recognized its potentially profound influence on future generations of electronics photonics, spintronics, and other technologies. Scientific research and development related to graphene has since gone on a tremendous and exciting journey.

1.2.1 Lattice Structures

As mentioned above, graphene is made of carbon atoms arranged into 2D hexagons with a triangular symmetry. A schematic of its atomic lattice is drawn in Fig. 1. It then immediately follows that the graphene lattice consists of two sets of triangular sublattices colored blue and orange in Fig. 1. The primitive unit cell is defined by two in-plane lattice vectors ($\mathbf{a_1}$ and $\mathbf{a_2}$) and contains two sublattice atoms:

$$\mathbf{a_1} = \frac{3a}{2}\hat{x} + \frac{\sqrt{3}a}{2}\hat{y} \tag{1}$$

$$\mathbf{a_2} = \frac{3a}{2}\hat{x} - \frac{\sqrt{3}a}{2}\hat{y} \tag{2}$$

where a is the carbon-carbon bond length and equals 1.42 Å. The size of the unit cell is then $|a_1| = |a_2| = 2.46$ Å. Correspondingly, the reciprocal lattice vectors ($\mathbf{b_1}$ and $\mathbf{b_2}$) can be written as:

$$\mathbf{b_1} = \frac{2\pi}{3a}\hat{x} + \frac{2\sqrt{3}\pi}{3a}\hat{y} \tag{3}$$

$$\mathbf{b_2} = \frac{2\pi}{3a}\hat{x} - \frac{2\sqrt{3}\pi}{3a}\hat{y} \tag{4}$$

According to Wigner-Seitz's convention, the first Brillouin zone can be constructed and drawn in Fig. 1, also forming a hexagon, rotate 90° (or 30°) from the real space hexagons. Several important locations have to be noted, which are the K and K' at the corner of the Brillouin zone , M the midpoint between K and K', and Γ in the center. K and K' are of particular interest because they are where the unique linear band structure lies and are often referred to as the Dirac point. The positions of K and K' can be derived from the reciprocal lattice vectors:

$$\mathbf{K} = \frac{2\pi}{3a}\hat{x} + \frac{2\pi}{3\sqrt{3}a}\hat{y} \tag{5}$$

$$\mathbf{K'} = \frac{2\pi}{3a}\hat{x} - \frac{2\pi}{3\sqrt{3}a}\hat{y} \tag{6}$$

Additionally, there are two unique directions in graphene lattice that, as will be discussed later, can greatly affect graphene's intrinsic band structure. Pointed out in Fig. 1, these two directions are often labeled as the [100] zigzag direction and [110] armchair direction in terms of the lattice vectors defined above.

Some of graphene's superb physical properties can be readily explained by the lattice structure and the associated C-C bonds that form it. Graphene is ultra thin and flexible because it only has one atomic layer. Graphene conducts electricity incredibly well because the electrons in the π orbitals can move essentially freely between atoms. Graphene is mechanically the strongest material in the world at the same thickness because the in-plane strong covalent bonding and its geometry ensures atoms are tightly connected.

1.2.2 Electronic Structures

The band structure of monolayer graphene can be analytically calculated based on the tight-binding model [13]. The covalent nature of the C-C bonds in graphene ensures that the tight-binding model will be a reasonable approximation to this system. Since graphene's unit cell contains two atoms or sublattices A and B, the overall electron wave function can be expressed as the combination of the two atoms each of which has a Bloch wave representation and follows the Schrödinger equation:

$$\Psi(\mathbf{k},\mathbf{r}) = \sum_n (c_{n,A}\Phi_{n,A}(\mathbf{k},\mathbf{r}) + c_{n,B}\Phi_{n,B}(\mathbf{k},\mathbf{r})) \tag{7}$$

$$\Phi_{n,\alpha}(\mathbf{k},\mathbf{r}) = \frac{1}{\sqrt{N}}\sum_{\mathbf{R}} e^{-i\mathbf{k}\mathbf{R}}\phi_{n,\alpha}(\mathbf{r}-\mathbf{R}), \qquad \alpha = A,B \tag{8}$$

$$(H_{at} + \Delta U)\Psi = \varepsilon\Psi. \tag{9}$$

where Ψ is the overall graphene wave function, Φ is the wave function from orbital n in sublattice α, H_{at} is the atomic Hamiltonian, and ΔU is the addition potential from the interaction between atoms. Since each carbon atom has four outershell orbitals ($n = 1,2,3,4$), the eigen-energy equation above would give an electronic structure containing 8 bands. However, since the 3 in-plane sp^2 orbitals are identical and strongly covalent, the corresponding wave functions are highly bound to the carbon atom. Therefore, for the highest energy valence states, we only need to consider the last out-of-plane p_z orbital for each atom and the overall system, reducing the wave functions to:

$$\psi(\mathbf{k},\mathbf{r}) = c_A\phi_{p_z,A}(\mathbf{k},\mathbf{r}) + c_B\phi_{p_z,B}(\mathbf{k},\mathbf{r}) \tag{10}$$

$$\phi_{p_z,\alpha} = \frac{1}{\sqrt{N}}\sum_{\mathbf{R}} e^{-i\mathbf{k}\mathbf{R}}\phi_{p_z,\alpha}(\mathbf{r}-\mathbf{R}), \qquad \alpha = A,B \tag{11}$$

To solve the Schrödinger equation, a simplifications can be made by assuming that the overlap among p_z orbitals is predominantly between nearest neighbors. The mathematical form follows:

$$\langle \phi_{p_z,\alpha} | \phi_{p_z,\beta} \rangle = \delta_{\alpha-\beta,n.n} \tag{12}$$

$$\langle \phi_{p_z,\alpha} | \Delta U | \phi_{p_z,\beta} \rangle = t\delta_{\alpha,\beta} \tag{13}$$

Straightforwardly, if $\langle \phi_{p_z,\alpha}|$ is multiplied on both sides in Eq. 9), we can rewrite it in a matrix form:

$$\begin{pmatrix} \varepsilon_0 & tg(\mathbf{k}) \\ tg^*(\mathbf{k}) & \varepsilon_0 \end{pmatrix} \begin{pmatrix} c_A \\ c_B \end{pmatrix} = \varepsilon \begin{pmatrix} c_A \\ c_B \end{pmatrix}, \tag{14}$$

where $g(\mathbf{k}) = 1 + e^{-i\mathbf{k}\mathbf{a_1}} + e^{-i\mathbf{k}\mathbf{a_2}}$, $\varepsilon_0 = \langle \phi_{p_z,\alpha} | H_{at} | \phi_{p_z,\alpha} \rangle$, and t is the hopping parameter defined in Eq 41, usually around 2.7 eV [4]. Since the two atoms A/B are identical, ε_0 should be a constant across the lattice, which can, without losing generality, be set as zero. Thus we can have an analytic relationship between momentum k and energy ε (band structure):

$$\varepsilon(k_x, k_y) = \pm\sqrt{t^2|g(\mathbf{k})|} = \pm t\sqrt{4cos\frac{3k_x a}{2}cos\frac{\sqrt{3}k_y a}{2} + 4cos^2\frac{\sqrt{3}k_y a}{2}} \tag{15}$$

A contour plot based on the above equation is listed in Fig. 2, whose symmetry about the zero energy axis is due to the nearest-neighbor approximation. There are six particularly interesting k points in the band structure, namely the K and K' points, and symmetry-identical replicas, where the valence band below zero touches the conduction band above zero. Therefore, graphene does not support a bandgap like semiconductor materials, instead it is a semimetal with degenerate bands at zero energy. In addition, graphene's Fermi level is also situated here, meaning that the whole bands are exactly half-filled in intrinsic graphene. Equation 15 can be expanded around the K (or K') point, assuming $|\mathbf{q}| = |\mathbf{k} - \mathbf{K}| \ll \mathbf{1}$, thus $g(k) \approx -\frac{\sqrt{(3)}}{2}a_0(q_x - iq_y)$ and the band structure becomes:

$$\varepsilon(\mathbf{k} = \mathbf{K} + \mathbf{q}) = \pm\hbar v_F|\mathbf{q}|, \tag{16}$$

where $v_F = \frac{3a|t|}{2\hbar} \approx 10^6 m/s$ is the Fermi velocity. Expansion around K' is the same. Apparently, around the K and K' points, energy is linearly dependent on the momentum and such

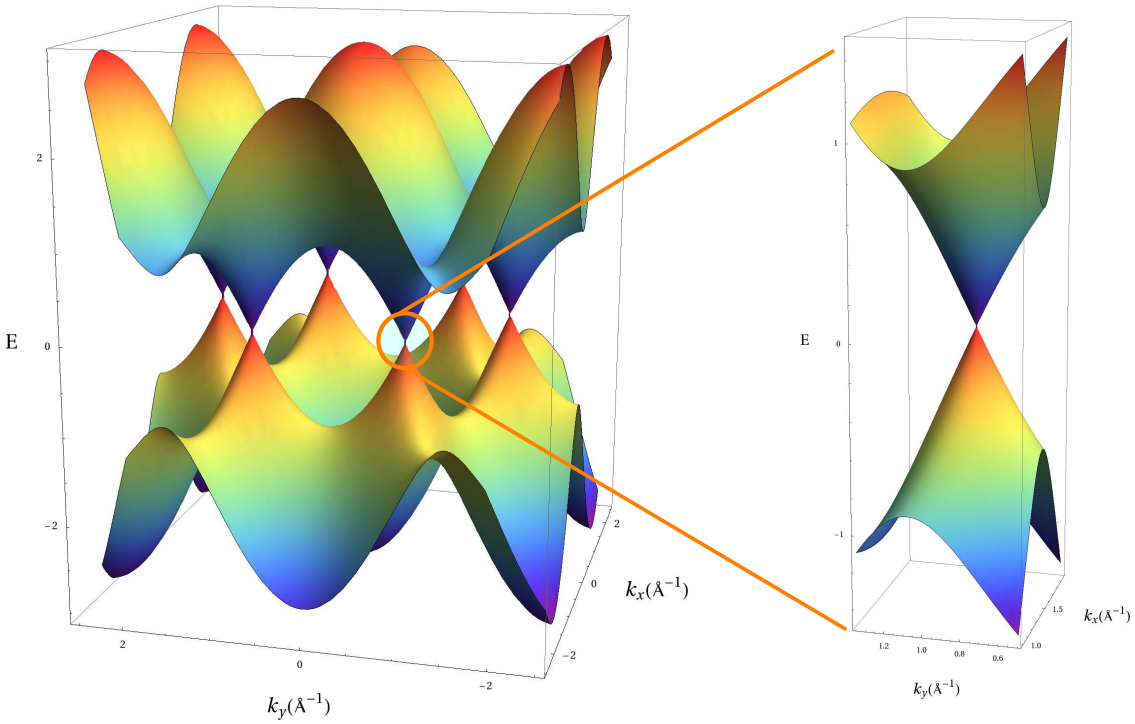

Figure 2: Band structure of Graphene from nearest-neighbor tight-binding model. The inset on the right shows the linear dispersion close one the K point.

unique linear band structure is the backbone of many of the surprising properties graphene exhibits. It is interesting to note that linear $\varepsilon - k$ dispersion is only found in massless particles following the Dirac Equation. Hence, carriers represented by $\psi = (c_A, c_B)^T$ in graphene can be thought of massless in the vicinity of K and K', often labeled as valley K and valley K'. Indeed, substituting q into the Hamiltonian matrix H in Eq. 14) leads to:

$$H_K(q) = \hbar v_F \begin{pmatrix} 0 & -(q_x + iq_y) \\ -(q_x - iq_y) & 0 \end{pmatrix} \tag{17}$$

It very much resembles the Dirac Hamiltonian, though not quite the same. However, if the wave functions are redefined by:

$$\Psi^K = \begin{pmatrix} -ic_{A,K} \\ c_{B,K} \end{pmatrix}, \qquad \Psi^{K'} = \begin{pmatrix} c_{A,K'} \\ -ic_{B,K'} \end{pmatrix} \tag{18}$$

then $H_{K(K')}$ has to been modified as well to ensure the equality $H_{K(K')}\Psi^{K(K')} = \varepsilon\Psi^{K(K')}$:

$$H_K(q) = \hbar v_F \vec{\sigma} \cdot \mathbf{q}, \qquad H_{K'}(q) = -\hbar v_F \vec{\sigma}^* \cdot \mathbf{q} \tag{19}$$

where $\vec{\sigma}$ is the vector of Pauli matrices. Now it becomes clear that quasi-particles represented by the wave function Ψ^K are indeed described by the Dirac Hamiltonian around K point, which can be consequently called the Dirac point. The same conclusion goes to the K' point as well. This is a significant observation in that Ψ^K coincides the form of a spinor where the coefficients measure the probability of finding an electron on sublattice A or B in valley K, serving as pseudo spins. This additional sublattice degree of freedom can lead to various anomaly effects as observed in normal spin-$\frac{1}{2}$ systems. A handy example is that the pseudo spin always changes sign along with momentum following Eq. 19, hence intra-valley scattering is strongly suppressed in graphene. As inter-valley scattering requires large change in momentum that is also unlikely to happen, graphene is largely free from backscattering which explains why it can achieve the record-high carrier mobility.

Although the discussions above are for the π bands, their counterpart σ bands do contribute to graphene's band structure. Full band structure calculation including the both bands has shown that σ bands reach their extrema at the Γ point in k-space, which evaluates at $\pm 4\,\mathrm{eV}$ [16–19], meanwhile, the π bands are at their maximum. Therefore, σ bands only serve as secondary sources for the transport characteristics on graphene because they are typically far away from the Fermi-level (K point) where most electronic conduction takes place.

1.2.3 Graphene under External fields

External fields can greatly alter the band structures near Dirac points in graphene, which is potentially useful in controllably engineering graphene's electronic properties. Generally, field effects that are significant in the graphene system come from electric fields, magnetic fields, and strain fields. While vertical electric field can possibly open an energy gap around Dirac points [20], it only applies to AB-stacked bilayer graphene, which is beyond the scope of this thesis. In this section, Landau levels formed by magnetic effects and Pseudo Landau levels emerging from strain effects will be discussed.

1.2.3.1 Magnetic effects

Magnetic fields are known to affect electron motions from the very early Hall Effects experiment. As the temperature approaches zero and the material becomes 2-dimensional, the classical Hall Effects is turned into Quantum Hall Effect (QHE) which produces a discrete spectrum of Hall conductivity with either integer (IQHE) or fractional (FQHE) increment (a.k.a the filling factor) depending on the nature of interactions present in the system (single particle or many-body effects). Although graphene is also a 2-dimensional system, the effectively massless electrons are completely different from the normal 2D materials which consists of massive 2D electron gas. Such distinct nature of carriers lead to the Quantum Anomalous Hall Effect (QAHE) observed in graphene (also in other special materials like topological insulators) where the quantization is shifted by $\frac{1}{2}$ and can be observed even at room temperature. While many factors contribute to the anomalous results, graphene's modified band structure by an magnetic field plays a central role.

From investigations of free electrons in magnetic field, the Hamiltonian has to be adjusted to include the magnetic effects by means of a vector potential $\mathbf{B} = \nabla \times \mathbf{A}$. The Hamiltonian is thus rewritten as:

$$H = \frac{1}{2m}\hat{\mathbf{p}}^2, \qquad \hat{\mathbf{p}} = \hat{\mathbf{p}}_0 - \frac{e}{c}\hat{\mathbf{A}} \tag{20}$$

If the magnetic field is aligned along the z-axis, $\mathbf{B} = (0, 0, B)$, then only p_x and p_y will experience the effects from magnetic forces. Hence, it is convenient to work with the Landau gauge, $\mathbf{A} = (-By, 0, 0)$ and neglect the p_z component.

Hamiltonian in graphene is different from the free electron case, but the gauge technique deployed is the same. From Section.1.2.2, it is known that K and K' are decoupled from each other in the Hamiltonian, so we can treat them separately. Close to K point, we have:

$$v_F \begin{pmatrix} 0 & -(p_x + ip_y) \\ -(p_x - ip_y) & 0 \end{pmatrix} \begin{pmatrix} \Phi_A \\ \Phi_B \end{pmatrix} = \begin{pmatrix} \varepsilon & 0 \\ 0 & \varepsilon \end{pmatrix} \begin{pmatrix} \Phi_A \\ \Phi_B \end{pmatrix} \tag{21}$$

By decomposing the above matrix into two individual equations and inserting one into the

other, the equations reduces to:

$$\varepsilon^2 \Phi_A = v_F(p_x - ip_y)(p_x + ip_y)\Phi_A \tag{22}$$

$$\varepsilon^2 \Phi_B = v_F(p_x + ip_y)(p_x - ip_y)\Phi_B \tag{23}$$

At this point, it is straight forward to solve for ε for Φ_A and Φ_B. Note that the Landau gauge implies p_x commutes with H, satisfying $[H, p_x] = 0$, hence for Φ_B, we can write:

$$\frac{1}{2m}\left(\frac{\varepsilon^2}{{v_F}^2} + \frac{\hbar e B}{c}\right)\Phi_B = \left(\frac{1}{2}\frac{eB}{c\sqrt{m}}\left(\hat{y} - \frac{p_x c}{eB}\right)^2 + \frac{\hat{p}_y^2}{2m}\right)\Phi_B, \tag{24}$$

which describes a harmonic oscillator with oscillation frequency ω_c and thus has discrete energy levels $\hbar\omega_c(n + \frac{1}{2})$. Substituting the appropriate values from the above equation, the energy ε satisfies:

$$\varepsilon = sgn(n)\sqrt{\frac{2\hbar e B}{c}} v_F \sqrt{|n|}, \qquad n = 0, \pm 1, \pm 2, ... \tag{25}$$

Similarly, for Φ_A, we can extract the expression for energy ε:

$$\varepsilon = sgn(n)\sqrt{\frac{2\hbar e B}{c}} v_F \sqrt{n}, \qquad n = 1, 2, ... \tag{26}$$

Both equations provide the expression for quantized Landau levels in graphene given an out-of-plane magnetic field. It is important to note that Landau Levels differ between sublattice A and B. The $n = 0$ Landau level has zero-amplitude on one the sublattices while all the other Landau levels have finite amplitude on both sublattices. In this treatment, $n = 0$ Landau level appears on B as tied to valley K, or A as tied to valley K'.

1.2.3.2 Strain effects

Graphene is strong material with an effective Young's modulus up to 1 TPa, which means it can be significantly deformed without being broken apart. Such impressive mechanical property has triggered a lot of efforts trying to understand its potential effects on the electronic properties of graphene.

When graphene is physically stretched or compressed, atomic spacings will change, as shown in Fig. 3, which in effect changes the hopping parameters in the off-diagonal element of the Hamiltonian [4, 22–24]. It has been well-understood that such changes usually lead to

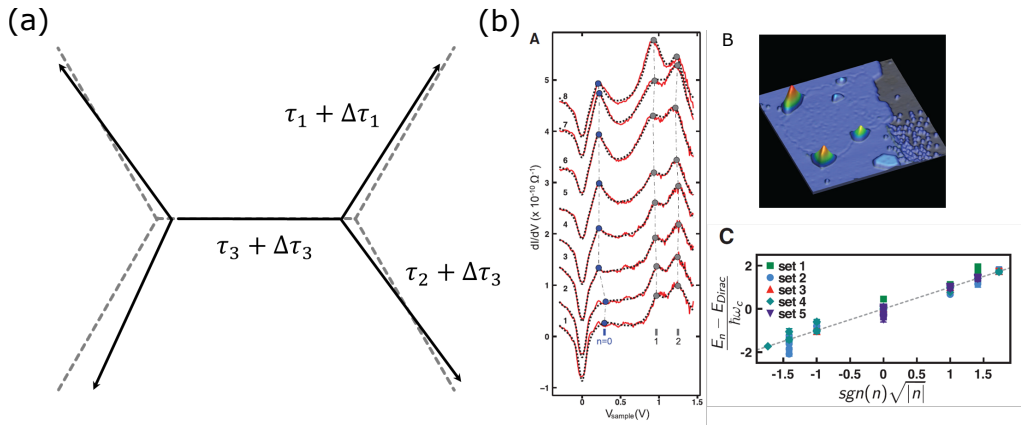

Figure 3: (a) schematic showing a distorted graphene lattice, with 3 new nearest neighbor vectors $\boldsymbol{\tau}_j$. (b) Adapted from [21], strained graphene protrusions giving rise to pseudo-Landau levels in dI/dV by STM. The corresponding pseudo-magnetic field is more than 300 T.

an effective gauge field added to the system, just like the magnetic effects discussed earlier. To see the effect, we rewrite the tight-binding Hamiltonian (Eq. 14):

$$H = \begin{pmatrix} 0 & -t\sum_{j=1}^{3} e^{-i\mathbf{k}\cdot\boldsymbol{\tau}_j} \\ -t\sum_{j=1}^{3} e^{i\mathbf{k}\cdot\boldsymbol{\tau}_j} & 0 \end{pmatrix} \tag{27}$$

where $\boldsymbol{\tau}_j{}'s$ are the three nearest neighbor vectors. In the low energy limit, H can be expanded around the Dirac points K and K'. The key difference to the normal Taylor expansion is that as strain is present, the atomic distances, hopping amplitude, as well as the reciprocal lattice distance all have to be adjusted. Let's denote that $t_j = t + \delta t_j$, $\boldsymbol{\tau}_j \to \boldsymbol{\tau}_j + \Delta\boldsymbol{\tau}_j$, $\mathbf{k} = \mathbf{K} + \Delta\mathbf{K} + \mathbf{q}$, then the summation in H at K point becomes:

$$-t\sum_{j=1}^{3} e^{i\mathbf{k}\boldsymbol{\tau}_j} \to -\sum_j t_j e^{i(\mathbf{K}+\Delta\mathbf{K}+\mathbf{q})\cdot(\boldsymbol{\tau}_j+\Delta\boldsymbol{\tau}_j)} \tag{28}$$

$$\approx -\sum_j (t+\delta t_j) e^{i\mathbf{K}\cdot\boldsymbol{\tau}_j} e^{i\Delta\mathbf{K}\cdot\boldsymbol{\tau}_j} e^{i\mathbf{K}\cdot\Delta\boldsymbol{\tau}_j} e^{i\mathbf{q}\cdot\boldsymbol{\tau}_j} \tag{29}$$

$$\approx -\sum_j (t+\delta t_j) e^{i\mathbf{K}\cdot\boldsymbol{\tau}_j} [1 + i(\Delta\mathbf{K}\cdot\boldsymbol{\tau}_j + \mathbf{K}\cdot\Delta\boldsymbol{\tau}_j + \mathbf{q}\cdot\boldsymbol{\tau}_j] \tag{30}$$

$$\approx -\sum_j t e^{i\mathbf{K}\cdot\boldsymbol{\tau}_j}(1 + i\mathbf{q}\cdot\boldsymbol{\tau}_j) - \sum_j \delta t_j e^{i\mathbf{K}\cdot\boldsymbol{\tau}_j} \tag{31}$$

Higher order terms are neglected from Taylor series and linear terms in $\Delta\mathbf{K}$ are also neglected since it has been shown lattice correction does not contribute to the artificial gauge

defined later[22, 24]. Similarly, the complex conjugate counterpart gives the result for K'. The off-diagonal element now consists of two terms, the first of which is what eventually leads to the linear $\varepsilon(k)$ dispersion. Apparently, the only extra term is the second part of the above expression, which has the expected dependence on the altered hopping parameter. If a vector potential is carefully chosen as having its x and y components correspond to the real and imaginary parts of the additional term, then the original Hamiltonian will be consequently modified into one that looks exactly the same as Hamiltonian under an external magnetic field introduced in the previous section:

$$\sum_j \delta t_j e^{i\mathbf{K}\cdot\boldsymbol{\tau}_j} = \frac{\sqrt{3}}{2}(\delta t_1 - \delta t_2) - \frac{1}{2}(\delta t_1 + \delta t_2 - 2\delta t_3)i \tag{32}$$

$$= A_x + iA_y \tag{33}$$

$$\mathbf{A} = \frac{\hbar^2}{\sqrt{3}aet}\begin{pmatrix} A_x \\ A_y/\sqrt{3} \end{pmatrix} \tag{34}$$

$$H = \hbar v_F \vec{\sigma}(\mathbf{q} - \frac{e\mathbf{A}}{\hbar}) \tag{35}$$

Interestingly, Eq. 35 suggests that strain enters the Hamiltonian of graphene in the form of an effective magnetic field which would lead to highly quantized electronic states. Such effects are referred to as pseudo-magnetic field and pseudo Landau levels. However, the pseudo-magnetic field is not entirely the same as a real one. It is important to note that the vector potential $\mathbf{A}$ is complex due to the lack of inversion symmetry in nearest neighbor hopping. Therefore, going from K to K', A_y will change sign leading to pseudo-magnetic field in the reverse direction, which essentially makes the total effective magnetic field of the system zero.

Equation 35 quantitatively describes the strain effect in graphene, but it is not yet in a useful format because in reality strains are usually slowly varying over a length scale much larger than the individual unit cell, thus the exact relation between the atomic level Hamiltonian and the macroscopic strain field needs to be established. In order to achieve so, a formal definition of strain is necessary.

When a system is strained, every point $\mathbf{r} = (x, y, z)$ is displaced to $\mathbf{r'} = (x', y', z')$,

such spatially varying displacement is called a deformation field $\mathbf{u}(\mathbf{r}) = \mathbf{r}' - \mathbf{r}$ and can be characterized by:

$$\mathbf{u}(\mathbf{r}) = \mathbf{r}' - \mathbf{r} = \begin{pmatrix} \epsilon_{xx} & \epsilon_{xy} & \epsilon_{xz} \\ \epsilon_{yx} & \epsilon_{yy} & \epsilon_{yz} \\ \epsilon_{zx} & \epsilon_{zy} & \epsilon_{zz} \end{pmatrix} \begin{pmatrix} x \\ y \\ z \end{pmatrix} \tag{36}$$

$$= (u_x(\mathbf{r}), u_y(\mathbf{r}), u_z(\mathbf{r})) \tag{37}$$

By applying first-order Taylor expansion to each axis of $\mathbf{u}(\mathbf{r})$ and comparing the results to the three equations above, we can define a new quantity named strain tensor that can be more easily calculated:

$$\begin{cases} u_{xx} = \epsilon_{xx} = \frac{\partial u_x}{\partial x} \\ u_{yy} = \epsilon_{yy} = \frac{\partial u_y}{\partial y} \\ u_{zz} = \epsilon_{zz} = \frac{\partial u_z}{\partial z} \end{cases}, \quad \begin{cases} u_{xy} = \frac{1}{2}(\epsilon_{xy} + \epsilon_{yx}) = \frac{1}{2}(\frac{\partial u_x}{\partial y} + \frac{\partial u_y}{\partial x}) \\ u_{yz} = \frac{1}{2}(\epsilon_{yz} + \epsilon_{zy}) = \frac{1}{2}(\frac{\partial u_y}{\partial z} + \frac{\partial u_z}{\partial y}) \\ u_{zx} = \frac{1}{2}(\epsilon_{zx} + \epsilon_{xz}) = \frac{1}{2}(\frac{\partial u_z}{\partial x} + \frac{\partial u_x}{\partial z}) \end{cases} \tag{38}$$

Based on the u_{ij} defined above, it is only needed to relate them to the change of hopping amplitude δt_j. As the hopping parameter highly depends on the inter-carbon distance, an accurate parametrization of its variation is given by $t(\tau) = exp[-\beta(\frac{\tau}{a} - 1)]$ with $\beta \approx 2$ being the Gruneisen parameter [4] and $a = 1.42\,\text{Å}$ the nearest atomic spacing. Hence, by expanding both $t(\tau)$ and $\boldsymbol{\tau} = \mathbf{r}_A - \mathbf{r}_B$ at the undeformed position, one can have:

$$t' = t - \frac{\beta}{a} t \Delta\boldsymbol{\tau} \tag{39}$$

$$\Delta\boldsymbol{\tau} = \boldsymbol{\tau} \cdot \nabla\mathbf{u}(\mathbf{r}) \tag{40}$$

$$\delta t_j = -\frac{\beta}{a} t \boldsymbol{\tau}_j \cdot \nabla\mathbf{u}(\mathbf{r}) \tag{41}$$

Combining Eq. 41 and Eq. 34, the vector potential $\mathbf{A}$ originated from the deformation field $\mathbf{u}(\mathbf{r})$ can be written as:

$$\mathbf{A} = \big(\kappa\frac{\beta t}{a}(u_{xx} - u_{yy}), \mp\kappa\frac{2\beta t}{a}u_{xy}, 0\big) \tag{42}$$

$$\mathbf{B} = \nabla \times \mathbf{A} = \big(0, 0, \mp\kappa\frac{\beta t}{a}[2\frac{\partial u_{xy}}{\partial x} + \frac{\partial(u_{xx} - u_{yy})}{\partial y}]\big) \tag{43}$$

where κ is dimensionless factor depending on the local bonding environment and $\mp$ is for K (-) and K' (+). Therefore, as long as the spatial variation in strain is known, the associated pseudo-magnetic field can be explicitly calculated. It should be noted that lattice

corrections clearly do not contribute to the pseudo-magnetic field, only the changed hopping amplitude does [22]. However, the spatial deformation does shift the Dirac points in k-space which would need to be accounted for in describing electron-momentum related processes. Lastly, experimental evidence has confirmed the existence of pseudo-Landau levels in graphene, as discrete density-of-states peaks are observed situated at energy positions that follows the $\sqrt{|N|}$ trend, but such measurements are mostly conducted on irregular graphene structures like graphene protrusions [21] and ridges [25]. A more general experimental study of graphene structures that are useful for fabricating electronic devices are needed.

1.3 Production Methods

Ever since graphene's first discovery, extraordinary progress has been made in creating bigger, better, and flatter graphene thin films. As of today, this atomic thin material are mainly fabricated in four ways, namely exfoliation, epitaxial growth, chemical vapor deposition(CVD), and oxide reduction. While each method proposes their unique strengths, none are perfect. Therefore, a comprehensive understanding and comparison among the different techniques would be extremely helpful in developing new fabrication methods that take the best of all worlds.

Exfoliated Graphene

Exfoliation is the first method [14, 26] to isolate graphene and is still widely used today for some of the fundamental research. The method works by preparing mesas of different sizes on highly oriented pyrolytic graphite(HOPG) and subsequently repeated peeling-off using scotch tape on the photoresist-attached surface. The peeled-off flakes are then transfered onto a Si/SiO_2 substrate. Monolayer graphene can be identified via an optical microscope when an appropriate SiO_2 layer thickness is used.

Advantages of exfoliation [27, 28] comes from the nature of its simplicity and decent-quality outcome. In addition, as monolayer graphene is already visible under optical microscopes, it greatly speed up the experimental procedures. However, there are serious drawbacks to this method. firstly, graphene flakes produced in this manner are usually

small, only about a few microns, while it takes a long time to reproduce samples of similar quality. What's more, as SiO_2 is known to be non-flat [27], the transferred graphene film exhibits a large surface roughness on the order of nanometers. Such surface corrugation often results in strained lattice, scattering centers, and so on. Lastly, interactions between graphene and the substrate also impose charge puddles on the surface that further degrades the carrier mobility in the thin film [29, 30].

Several routes have been proposed to circumvent the aforementioned problems such as suspending graphene by etching away the substrate. While it does provide considerably higher carrier mobility, suspended graphene [30, 31] still suffers from high stress and can be fragile during measurements. Another option is using a 'clean' substrate like hexagonal Boron Nitride (hBN) [32, 33], which provides good lattice match and little interaction. This method has proven to be promising as flat and intact graphene lattice has been imaged by STM with observed long ballistic transport length, but more work is needed to achieve large scale production and bandgap engineering.

CVD Graphene

CVD graphene has become more and more popular for graphene creation due to its low cost and scalability [34]. The method works by injecting hydrocarbon gas such as methane or ethylene into the CVD reactor and growing graphene on metals surfaces as the gas passes over and carbon radicals are released from decomposition in a hot zone. Large areas of graphene have been produced via this method on a variety of metallic substrates (Cu, Ni, Ru, Pt, Ag, etc.) [30, 34]. In fact, a recent report by an European research project demonstrates a cost-effective roll-to-roll production tool that is capable of growing graphene on a 300mm-style wafer simply based on the CVD method [35]. However, issues with this approach are also obvious. As graphene is typically grown on metallic surfaces which lack the circuit isolation when used in electronic devices, the top graphene layer has to undergo a transfer process which usually brings substantial damage to and leaves residue on the surface, resulting in lower carrier mobility. Moreover, CVD graphene is often found to have multiple domains rotated at different angles and various wrinkle structures as well [30]. Such inhomogeneity can give rise to significant scattering and non-uniform strain in the lattice

[34, 36]. Doping and interaction from the metals can also impact the linear band structures of graphene that could potentially affect some of its properties related to the Dirac point [34, 36]. Some techniques has been developed to improve the transfer process such as the vapor-trapping method for large-grain graphene growth and using metallic nanoparticles for direct graphene growth on insulating substrates. Nonetheless, CVD is considered to be a highly promising method for large scale and high quality graphene production, a great number of companies and research institutes are going in the direction.

Reduced Graphene Oxide

Producing graphene by reducing graphene oxide provides an attractive alternative [30] for mass production of the materials. It has primary application in composites, coatings, paint/ink, and energy storage, though still faces a number of challenges to be solved. The method works in the following procedures. Graphite oxide are firstly prepared using Hummer's method or its modified versions [37] and then immersed into water. Being hydrophilic, the bulk material fully disperses in water by stirring or ultrasonicating, breaking up into monomoelcular sheets, or the graphene oxide. In the subsequent process, various reduction methods are applied to the separated graphene oxides to reduce the carbon-oxygen functionalities in the material and heal the structural defects to form graphene. The key of the method lies in the wide range of reducing agents, which have to be optimized in chemical groups, solution environment, and treatment time for effectiveness [38]. Reduction methods [39] include thermal reduction, chemical reduction, electrochemical reduction, laser-based reduction, and so on. While it has been successful in some applications, the large quantity of defects and uncontrollable surface inhomogeneity must be overcome to make it a viable way for real production [38].

Epitaxial Graphene on SiC

From the previous discussions, graphene can be grown either on a large scale but with compromised quality, or in a clean and pristine form but with limited domain size. Therefore, a better substrate that can ensure both scalability and reliability is highly desired. Silicon carbide (SiC) emerges as a seemingly perfect choice for such requirements. Growing graphene on SiC dates back to 1975 when Van Bommel [43] first demonstrate that when a

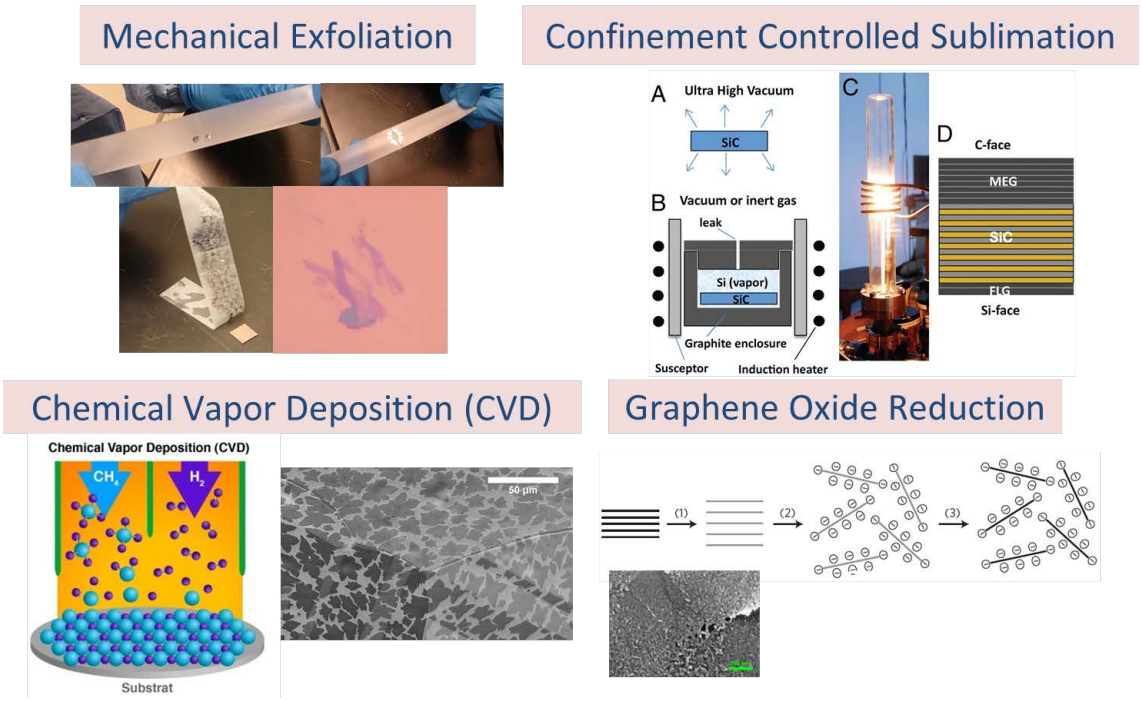

Figure 4: Four main approaches to create graphene. Adapted from Refs. [26, 40–42]

hexagonal SiC piece is heated to a high temperature, Si atoms would sublimate from the surface, leaving the excess carbon migrating and reconnecting to form a 'monolayer graphite'. However, it is the Georgia Tech team led by Dr. Walter de Heer (and other researchers [18, 44–48]) that really reinvent the method, put extensive efforts into understanding the growth, and improve the outcome. It is now understood that graphene can be epitaxially grown on both Si-terminated (Si-face) and C-terminated (C-face) polar faces of SiC with commensurate lattice match. Due to the extreme flatness of SiC, the graphene layer largely maintains its uniformity and exhibits reproducibly more ordered electronic structures. By far, using the method developed in Georgia Tech, graphene on SiC has shown wafer-scale growth [49], ultra-high carrier mobility (on C-face) [50], micron-scale ballistic transport [5], high-quality quantum Hall effect [51], and sidewall nanoribbons with variable band gaps [11]. With the rapidly increasing availability of SiC substrates, this method is believed to be a powerful force behind the graphene revolution.

SiC has more than 200 polytypes due to its unique structure. Within the crystal, Si(C) is bonded with four other C(Si) atoms and therefore can be regarded as Si-C bilayers stacked

together. SiC has two important polytypes, namely the 4H-SiC where every other bilayer changes the stacking order, and the 6H-SiC where every three bilayers change the stacking order. On these two polytypes, two crystal facets are of crucial significance to graphene growth, which are the SiC(0001) surface terminated with a layer of silicon atoms (Si-face), and the SiC($000\bar{1}$) surface terminated with a layer of carbon atoms (C-face).

The original Si-sublimation growth process has evolved and developed over the time into what is called a Confinement Controlled Sublimation (CCS) method today. This method aims at creating a quasi-equilibrium environment for the graphene growth to avoid non-uniform formation due to low temperature fast graphitization. To achieve such target, CCS limits the Si-sublimation rate by spatially confining the sublimated silicon to create a Si-rich closure in a low vacuum. The high and lasting Si vapor pressure ensures that surface carbon migration takes place in thermodynamic equilibrium where the graphitization process is slowed down. Usually before growth, a high temperature hydrogen etching procedure is performed in order to clean and smoothen the original SiC surface.

Graphene forms differently on the two polar faces on SiC, partly due to the different terminations. On the **Si-face** [52], graphene growth exhibits an inverted procedure where new layers form at the graphene-SiC interface lifting up the previous grown layers. The bottom graphene layer is found to be electronically different from free monolayer graphene in that it is strongly bonded to the SiC substrate becoming non-conductive. Various measurement including STM and ARPES has indeed shown a small gap around the Fermi level. In addition, because of the strong interaction, a commensurate ($6\sqrt{3} \times 6\sqrt{3}\,\mathrm{R}30^\circ$) surface reconstruction with a quasi 6×6 periodicity is observed in both STM and LEED whose high symmetry points are formed by (near) perfect vertical alignment between graphene lattice and SiC. Such structures cause monolayer graphene under STM showing additional height variation up to 1 Å. However, such layer can be decoupled from the substrate becoming a quasi-freestanding layer by hydrogen passivation underneath. Above this interfacial layer (also called buffer layer or layer 0), monolayer graphene maintains the intrinsic linear band structure but electron-doped placing its Dirac point around $-400\,\mathrm{meV}$ in STS because of

the charge transfer from the SiC substrate, whereas bilayer graphene shows quadratic energy dispersion. An interesting observation is that graphene layers on the Si-face follows the same AB-stacking order as graphite, thus making few-layer graphene on this face similar to graphite in various properties. Lastly, since graphene grows much slower on Si-face, the layer thickness can be carefully controlled which partly explains the extensive research interest on such face.

In contrast, graphene grows much faster on the **C-face** [52], which can easily accomplish a few tens of layers and can even induce 3D structures like carbon nanotubes in UHV growth. Unlike the Si-face, such layers manifest a so-called stacking disorder where each layer is slightly rotated from its neighbors, although two principle rotation angles, 0° and 30°, do exist. The relative rotation has given rise to interesting Moire patterns resolved by STM changing the apparent heights of the surface. Another important consequence of the unique stacking disorder is that neighboring graphene layers are electronically decoupled meaning that few-layer graphene on C-face behaves just like monolayer graphene individually added together as has been evidenced by ARPES, Raman, and other measurements. Similar to the Si-face, graphene on C-face are also highly electron-doped with the doping level decaying rapidly from the bottom layer to the top. The bottom layer is also an interfacial layer but is not well understood since monolayer graphene growth has only been achieved for a limited time, though it has been shown to be the dominant layer in transport properties.

1.4 Graphene Nanoribbons (GNRs)

An extensively studied form of graphene is the graphene nanoribbons (GNRs). Because the lack of intrinsic bandgap in graphene, various ways have been proposed to alter the linear band structure for bandgap engineering, among which graphene nanoribbons draws particular attention. The thin-stripe geometry of GNRs naturally ensures that a band gap can be opened due to the quantum confinement effects where only discrete electronic modes are allowed in the system. In addition, the various boundary conditions in the one-dimensional system can greatly alter graphene's pristine electronic structures. Their ideally flat and regular shape also makes GNRs easier to be integrated into standard circuit design

and lithography techniques for large scale fabrication.

Theoretical study has confirmed that quantum confinement of the transverse momentum across the ribbon width can lead to band gap inversely proportional to the width $E_{gap} = \frac{\alpha}{W_G}$ where W_G is the width and α ranges between 0.2 – 1.5 eVnm depending on the details of the system [53, 54]. This energy gap comes purely from the geometric configuration regardless of the edge terminations. What's more, since new boundary conditions are imposed by the abrupt edges of the ribbon, the original 2D wave functions for bulk graphene becomes 1D and is highly sensitive to the different types of edges or the chirality and hence show differently altered band structures. GNRs support 3 types of edges, armchair edges that are parallel to the C-C bond, zigzag edges which rotates 30° from the previous one, and chiral edges consisted of mixtures of armchair and zigzag edges. The graphene lattice in Fig. 1 illustrates their directions. Based on tight-binding calculations, it is predicted that zigzag GNRs possess flat bands that lie between $[\frac{2\pi}{3a}, \frac{\pi}{a}]$ in k-space near zero energy in addition to the band gap from quantum confinement [55]. Such conducting channels are called edge states, which primarily comes from the fact that only one set of the two sublattices is present along the zigzag edges. Therefore, zigzag GNRs are always metallic. Armchair GNRs, however, are metallic if the width follows $N = 3M + 2$ where M is an integer and N is the number of unit cells the GNRs span across, but are semiconducting from the confinement effects otherwise [56, 57]. In addition, first principle calculations have shown that even $N = 3M + 2$ Armchair GNRs are semiconductors as well, although with the smallest bandgap compared the other two families. The origins of such band gaps are primarily due to the fact that the two Dirac cones of the pristine graphene, in this orientation, approaches each other when projected into the one-dimensional Brillouin zone leading to a vanishing density of states in the edge states [58]. As for chiral GNRs, since it contains zigzag components, edge states are also supported on such ribbons thus making them metallic, too, although the amplitude of which would depend on the proportion of zigzag components [59]. An important consequence of the edge states is that such GNRs may possess perfect conducting channels because the flat bands only occurs near the Dirac point without bulk band components that allow various scattering processes. Hence, electrons

in this state can potentially move without interference along the ribbon independent of the length, which on the macroscopic scale turns into ballistic transport. When electron-electron interactions are added in, the degeneracy of the edge states are lifted creating a bandgap at the charge-neutral point [57]. Such interactions give rise to a peculiar type of magnetic ordering where the magnetic moments on the edges are ferromagnetic along the edge direction but anti-ferromagnetic across the ribbon width [60]. What is more, spin-orbit interactions, though weak in the graphene system have also been investigated and are predicted to also open a gap around zero energy lifting the edge states, which contributes to the absence of backscattering in the conduction edge channels [57]. However, the spin-orbit gap is only on the order of 1×10^{-5} eV in graphene, hardly observable. Despite of the different natures of the potential band gap opening in the different types of GNRs, the inverse width dependence is always valid [53] exhibiting the power of controlling electronic properties of GNRs via different widths. Lastly, local structures of the GNRs edges can also dramatically affect their overall band structures, such effects include edge functionalization, substrate interaction, and so on.

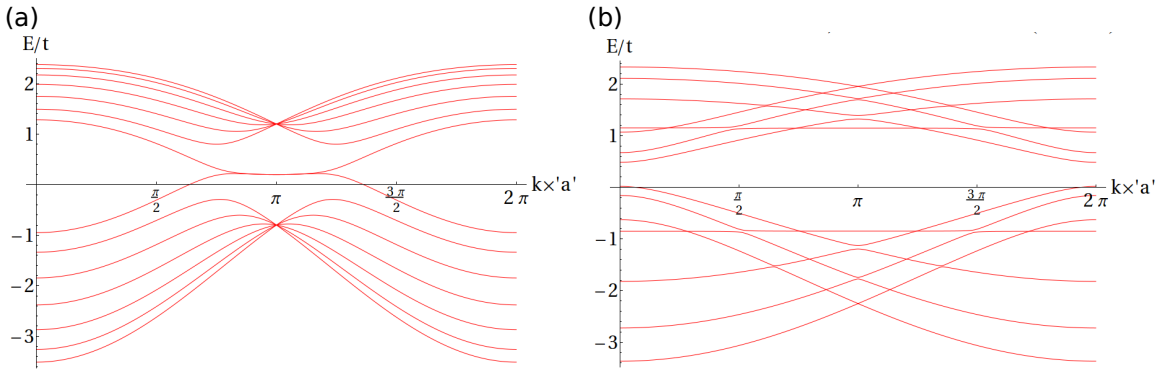

Figure 5: Band structure of graphene nanoribbons 9 unit cells wide, calculated using tight-binding model with next nearest neighbor hopping $t' = 0.1t$ included, (a) along the zigzag direction, (b) along the armchair direction.

GNRs have been so far fabricated using different approaches. Inconsistent yet interesting characteristics are observed between the methods. Standard electron-beam lithography is among one of the first efforts to produce GNRs [61, 62]. The etching procedure serves as sharp scissors that can cut out GNRs from bulk graphene sheet with controllable width. Despite of the observed semiconducting characteristics on such GNRs, the results do not

depend on the edge directions and exhibit unexpectedly large on/off ratios on wide GNRs. It turns out that, localized electronic states arising from disorders along the two opposite GNRs edges have to be included in the model in order to explain such anomalies, thus leading to the distinction of different energy gaps [63]. A transport gap, seen as suppressed conductance within a voltage range, is caused by quantum dots formation due to edge and bulk disorders. These quantum dots introduce additional randomized local electronic states and lead to Coulomb blockades that lower the carrier mobility and appear to be a larger band gap in the transport measurement. A true band gap, however, is generally smaller than the transport gaps and can be more affected by them on narrow GNRs. Unfortunately, disorders are usually inevitable from the residuals and chemical reactions during the lithography process, therefore, GNRs made from this approach is not ideal for high speed electronic devices.

CVD and unzipped carbon nanotubes are two other options for making GNRs [34, 64, 65]. Both methods make use of chemical precursors to either preferentially form elongated graphene thin stripes or cut longitudinally along multiwalled carbon nanotubes to create graphene nanostructures. Unlike the lithography process, these methods produces atomically smooth edges along the GNRs, therefore have demonstrated much higher carrier mobility and high on/off ratios on prototype transistor devices. However, there is a key difference between the two methods. GNRs from unzipping inherit the width and chirality of the carbon nanotubes, which, as the cutting direction is not well-defined, mostly lead to chiral edges. This explains why localized states near the Fermi level are observed in STS measurements [66]. Additionally, atomically resolved edges are not observed on such ribbons partly due to possible residual oxygen functional groups left on the edges, which can negatively impact the overall electronic structures. In contrast, CVD is a bottom-up approach to from GNRs, which provides full control of the edge termination and ribbon size by choice of different precursors. Indeed, GNRs as narrow as 1 nm has been synthesized and atomically resolved edges along both armchair and zigzag directions are seen under STM [66, 67]. Also, bandgaps inversely proportional to ribbon widths are in good agreement with theoretical predictions. Although the two methods are able to overcome the edge

roughness, they suffer from randomly oriented GNRs on the substrate, and the length of such ribbons can not be arbitrarily long. Therefore, while an ideal platform for prototyping and fundamental research, CVD and unzipped carbon nanotubes are not viable for scalable digital electronics.

Another way for producing GNRs is epitaxially growing graphene along step facets on SiC [68]. This selective growth is possible because graphene nucleation usually start near surface step edges. By carefully control the temperature and growth time, graphene formation can be limited only along the step facets and the top flat terraces near them. The power of this method lies in the experimental indication that the edges of such stripes are strongly interacting with the SiC substrate thus providing atomically sharp boundary terminations without compromising the orderliness or losing the connections to the other surface areas [11, 69]. Transport measurement has shown micron-scale ballistic transport on these GNRs confirming their high-quality [5]. However, the origin of the exceptional conducting behavior remains mysterious. In addition, as the ribbon edge is not a physical termination in graphene lattice, such distinct deviation from the aforementioned approaches can potentially introduce more complicated but interesting electronic structures. From the perspective of applications, sidewall GNRs are readily placed on the insulating SiC substrate without the need for transfer. The method can be easily scaled up in GNRs array fabrication [68] and also provides a large parameter space for tuning the GNRs geometry. Obviously, it is one of the most promising direction for integrating graphene into modern electronics, hence a more systematic understanding of the system is imperative.

CHAPTER II

EXPERIMENTAL METHODOLOGY AND SETUP

In order to study 2D materials like graphene and in particular GNRs, surface science techniques play a central role in exploring and understanding material properties concentrating on the top layers of a sample within a few nanometers. In this thesis, various surface-sensitive measurements are conducted in conjunction with one another. The primary experimental methods involve Scanning Tunneling Microscopy (STM), Low Energy Electron Diffraction (LEED), and Auger Electron Spectroscopy (AES), all integrated in a Ultra High Vacuum system (UHV). Other tools such as Atomic Force Microscopy (AFM), Electrostatic Force Microscopy (EFM), Raman Spectroscopy, E-beam Lithography, Ion Sputtering, E-beam Heating, as well as Mechanical Grinding are also used for different parts of the research, but in limited occasions. In this chapter, the UHV environment will be firstly introduced, followed by detailed discussions of three primary surface science techniques, namely LEED, AES, and STM. Instrumentations and applications specifically for the graphene/SiC system will be included. At the end of the chapter, the other measurement techniques will be briefly discussed aiming at a complete understanding of the full array of methods that make this research possible.

2.1 UHV Systems

Vacuum systems are widely built across various industries from surface characterization to particle accelerators, from crystal growth to outer space research. In the condensed matter physics community, ultra clean sample surfaces are mostly crucial in exploring material properties isolated from external contaminants, but physical and chemical adsorptions take place within a fraction of second in ambient environments. What is more, surface spectroscopy measurements often desire certain particles such as ions and electrons travel to and from the sample surface without colliding with other molecules while the viscous flow in atmosphere makes it impossible for such movements. In contrast, vacuum environments

well meet the aforementioned experimental requirements due to the fact that gas molecules in a low pressure setting maintain much longer mean free paths, defined in the following equation:

$$\lambda = \frac{k_B T}{\sqrt{2}\pi\xi^2 P,} \tag{44}$$

where k_B is the Boltzmann constant, T is the temperature of the gas, ξ is the average diameter of gas molecules, and P is the pressure. In other words, the number of particles in a fixed volume is significantly reduced and it becomes much less likely for two particles to directly interact with each other. However, in a normal vacuum system (10^{-4} to $10^{-6} mbar$), although the typical mean free path at room temperature (300 K) is on the order of 10 m to 1000 m (assuming a molecule size of several angstroms), the rate of impinging molecules, defined by:

$$R = \frac{P}{\sqrt{2\pi M k_B T}}, \tag{45}$$

where M is the molecular mass, is on the order of $10^{14} cm^{-2} s^{-1}$, which means for a millimeter-size surface building up a complete layer of adsorbate it only takes a few seconds, an impractical time scale for most experiments. Therefore, UHV environments ($< 10^{-9} mbar$) become the primary choice for surface sensitive measurements, which provides much longer mean free paths than the physical dimensions of UHV chambers and allows much longer experimental time up to tens of hours.

Well-designed pumping mechanisms are required to achieve UHV pressure. However, as vacuum technology extends on such a wide range of pressures, it is not yet possible for a single pump to achieve UHV range directly from atmospheric pressure. Instead, different stages of pumping connected in series are required. A typical UHV system is equipped with a roughing pump working in the usual gas flow regime down to $10^{-6} mbar$, a turbo-molecular pump further reducing the pressure to $10^{-6} mbar$, and an ion pump finally achieving pressure less than $10^{-9} mbar$. Usually an additional titanium sublimation pump (TSP) is also mounted to help maintain the base pressure at times. Before entering the working mode, a thorough bake-out is performed to fully desorb gas molecules from chamber walls and surfaces. This procedure requires heating up the entire system to roughly 150°C for at least 24 hours and filament outgassing during the cooling process. Once UHV is

achieved, materials for use in the chamber have to be carefully chosen. Any high vapor-pressure material like most organic compounds and some metals (Zn, In, Pb) can potentially degrade the vacuum quality by liberating gases and reabsorbing on other surfaces. Normally, UHV systems incorporate several experimental instruments in one chamber or connected chambers aiming at in-situ characterization or monitoring, most prevalent ones include MBE, RHEED, LEED, XPS, ARPES, TEM, STM and so on. In this project, two UHV systems are mainly utilized for relevant measurements. Figure 6b shows a home-built room temperature STM system (RT-STM) with base pressure held at $1 \times 10^{-10} mbar$. Other than the equipped ion pump, turbo molecular pump, diaphragm pump,and TSP for UHV maintenance, the system also includes LEED, AES, Field Emission Microscopy (FEM), Residual Gas Analyzer (RGA) and a Besocke-style STM head. For sample preparation, an e-beam bombardment heater is mounted on the manipulator with a K-type thermocouple connection. An ion gun for sputtering and metal deposition is also available. This system is designed for batch loading and unloading which can transfer 5 STM tips and 2 samples at a time. STM tips can be annealed and characterized by in-situ FEM. In addition, a customized sample holder and vacuum transfer suitcase are designed for transferring as-grown graphene samples from an external growth chamber in the lab to the UHV system maintaining an inside pressure about $10^{-8} mbar$.

Figure 6a shows a second commercial low temperature STM system from Createc (LT-STM) with rest gas pressure around $10^{-11} mbar$. It has a preparation chamber and an STM chamber that can be isolated from each other. Two pairs of ion pumps and TSPs are mounted for the respective chambers. On the manipulator there is an e-beam bombardment heater and a multiple contact position for direct current heating, both connected with nitrogen cooling channels. An external electron gun for AES, an ion gun along with Neon-filled leak valve for sputtering, and an analog Mass Spectrometry Analyzer are also added. The key component is the STM/AFM head that enables fast cooling and direct optical access while maintaining ultra high resolution imaging. The STM works at low temperatures down to 4 K with optional vertical magnetic fields up to 2 T. More details about STM will be covered in the STM section to come.

(a)

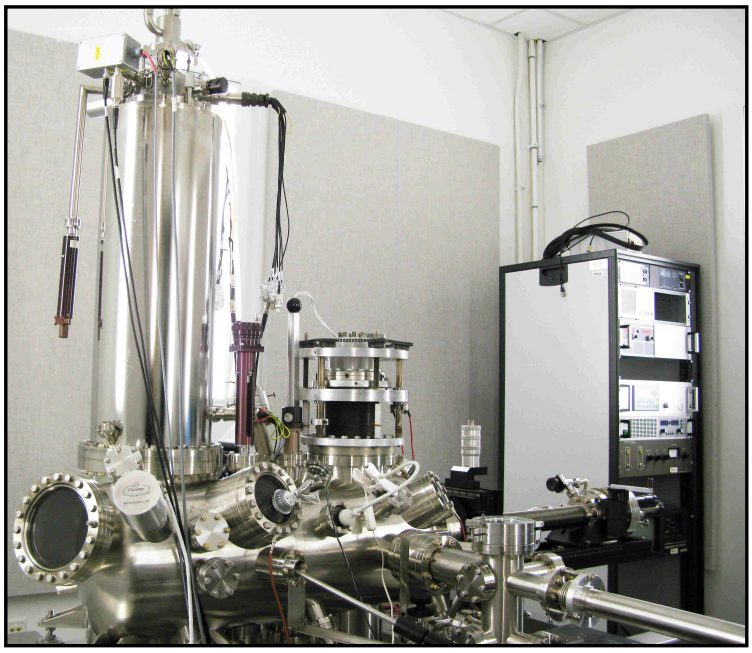

(b)

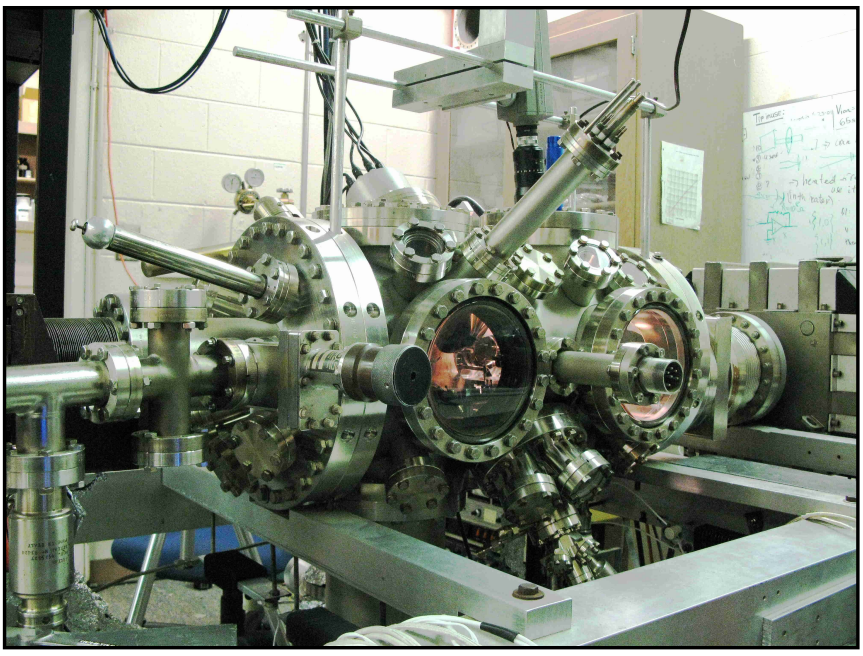

Figure 6: UHV systems. (a) Low temperature STM from Createc. The STM head sits under the cylindrical dewar. (b) Room temperature STM home-built in the lab. The STM head is located in the second compartment to the right of the image.

2.2 Low Energy Electron Diffraction (LEED)

2.2.1 Basic Theory

LEED is historically first reported by Davisson and Germer in 1927 for their study of electron scattering on nickel [70]. Ever since its invention, LEED has become a popular technique for surface characterization due to its fast data acquisition process, relatively intuitive analysis, and great microscopic accuracy. Just like XPS is a powerful tool to determine crystal structures of bulk solid materials, LEED is analogously the 2D version of XPS that is capable of determining crystal structures of material surfaces within a few atomic layers by emitting electron beams at sample surfaces and collect the elastically reflected electrons. The main reason that LEED is so surface-sensitive lies in the low energy beams used in the measurement. Within typical LEED operating energies between 10 eV and 300 eV, electrons impinging on the surface have small mean free paths (λ_e) on the order of 1 nm, which captures the strong complex elastic and inelastic scattering events between them and the surface atoms. Using the attenuation model for elastic electron flux and substituting the above mean free path in $I \sim I_0 e^{-d/\lambda_e}$, it immediately gives a penetration depth d at most several nanometers long. Therefore, the low energy electron beams ensure that collected signals are dominantly from the top few atomic layers from the sample surface and achieve microscopic resolution due to the small mean-free paths.

For qualitative understanding of the LEED patterns, the diffraction process in solids must be explained. When an incident beam arrives in a three dimensional lattice, the Bragg condition governs all possible reflected wave vectors,

$$\Delta\mathbf{k} = \mathbf{k}' - \mathbf{k} = \mathbf{G}, \tag{46}$$

where $\mathbf{k}$ is the incident wave vector, $\mathbf{k}'$ is the reflected wave vector, and $\mathbf{G}$ is the reciprocal lattice vector. Only $\mathbf{k}'$s satisfying such equality are valid reflection directions. A better visualization is given by the Ewald sphere shown in Fig. 7a. The Ewald sphere has a radius equal to $|\mathbf{k}|$ and is drawn such that at least one reciprocal lattice site falls on it. Following Eq. 46, any possible reflected wave vector $\mathbf{k}'$ must start from the center and end in one of the other reciprocal lattice sites on the sphere. Such approach works well in bulk solids where

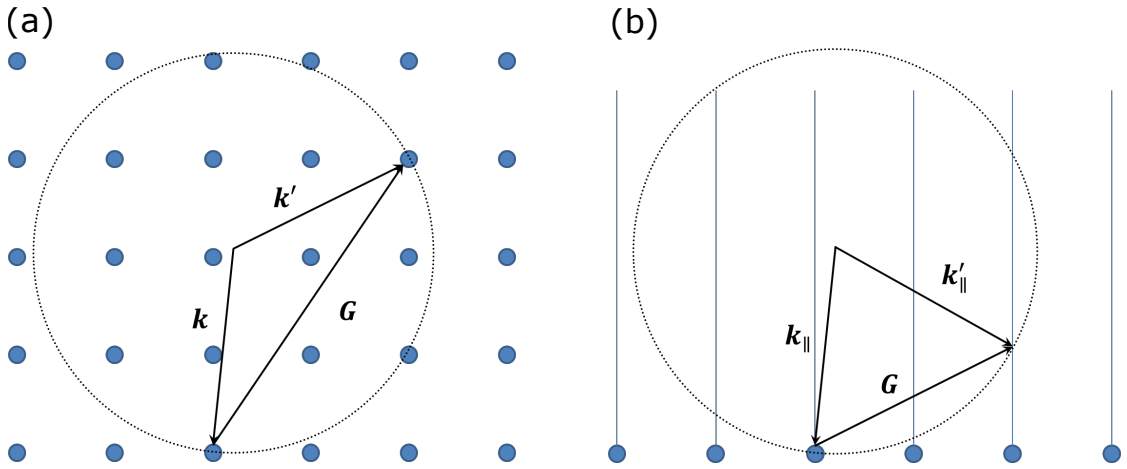

Figure 7: Cross sections of Ewald spheres in 3D and 2D cases. (a) 3D Ewald spheres with the blue circles as the reciprocal lattice sites, $\mathbf{k}$ is the incoming wave vector, $\mathbf{k}'$ is the scattering wave vector, $\mathbf{G}$ is a reciprocal lattice vector. (b) 2D Ewald spheres with the blue lines as the vertical rods extending from each reciprocal lattice sites, only the parallel components of the wave vectors have to comply with the Bragg condition.

the reciprocal lattice is three-dimensional. However, in the case of LEED, a 2D adaption must be taken. Reciprocal lattice for material surfaces is two-dimensional, hence the Bragg condition becomes:

$$\Delta\mathbf{k}_{\parallel} = \mathbf{k}_{\parallel}{}' - \mathbf{k}_{\parallel} = \mathbf{G}, \tag{47}$$

where only the parallel components to the surface plane are used. The vertical component is not constrained due to the lack of periodicity in that direction. To illustrate using Ewald sphere (Figure 7b), rods are placed perpendicular to the surface plane from each reciprocal lattice site, similarly, whenever the sphere intersects with the modified 3-dimensional reciprocal lattice other than the chosen zero-order $(0, 0)$ point, a reflected wave vector forms. It is obvious that all rods will at least intersect with the sphere once when the magnitude of the incident vector becomes infinitely large, which means an ever-increasing beam energy in LEED. Therefore, LEED diffraction patterns are essentially a mapping of the reciprocal lattice points that meet the 2D Bragg condition given an incident energy. As the beam energy increases, more and more higher-order diffraction can be observed (more intersections on the Ewald sphere).

The above treatment entirely follows Kinematic scattering theory assuming only single

scattering event for each incident electron. By including more details about the diffraction process such as multiple inelastic scattering and inter-layer scattering, quantitative analysis on the intensity variation of diffraction patterns with respect to the perpendicular momentum (wave vector) of the incident electron beam becomes feasible, which is able to provide structural information of unit cells and its ordered arrangement. Such analysis is often referred to as dynamic LEED theory.

2.2.2 Instrumentation

A typical LEED system is consisted of three components, an electron gun, a collector with screen and grids, and the controller electronics. In this thesis, the rear-view LEED system from Princeton Research Instruments is added onto the RT-STM chamber. The electron gun and the collector are integrated together into a retarding field analyzer (RFA), the diagram of which is shown in Fig. 8, reproduced from the hardware manual. The electron gun (filament inside) sits at the back of four hemispherical grids G1 through G4, coaxially aligned. Two connections F1 and F2 goes to the controller for adjusting the filament current. Thermionic emission and beam focus controls lie between the grids and the filament, which provides fine tuning of the secondary emission and beam size. On the detector, grid G1 and G4 are grounded for electrostatic shielding, while G2 and G3, the retarding grids, are shorted together and held at a negative potential with respect to G1 and G4 to block the low energy inelastically scattered electrons and only allow those elastic electrons to pass through, which is crucial for generating LEED signals. The dual grid setup is particularly powerful for resolution enhancement in that it reduces the potential variations in the vicinity of the grids [71]. At the very end of the grids, a spherical phosphorous screen is placed, whose screen voltage is supplied through C on the controller. The system works by generating a focused electron beam at a given energy through thermionic emission from the heated filament and striking the sample placed at the common center of the hemisphere, backscattered electrons are then collected and high-pass filtered via the retarding grids, which get accelerated by the high positive potential difference between the collector screen and the grounded G4 with diffraction patterns appearing on the screen by phosphorescence. Typically, the beam

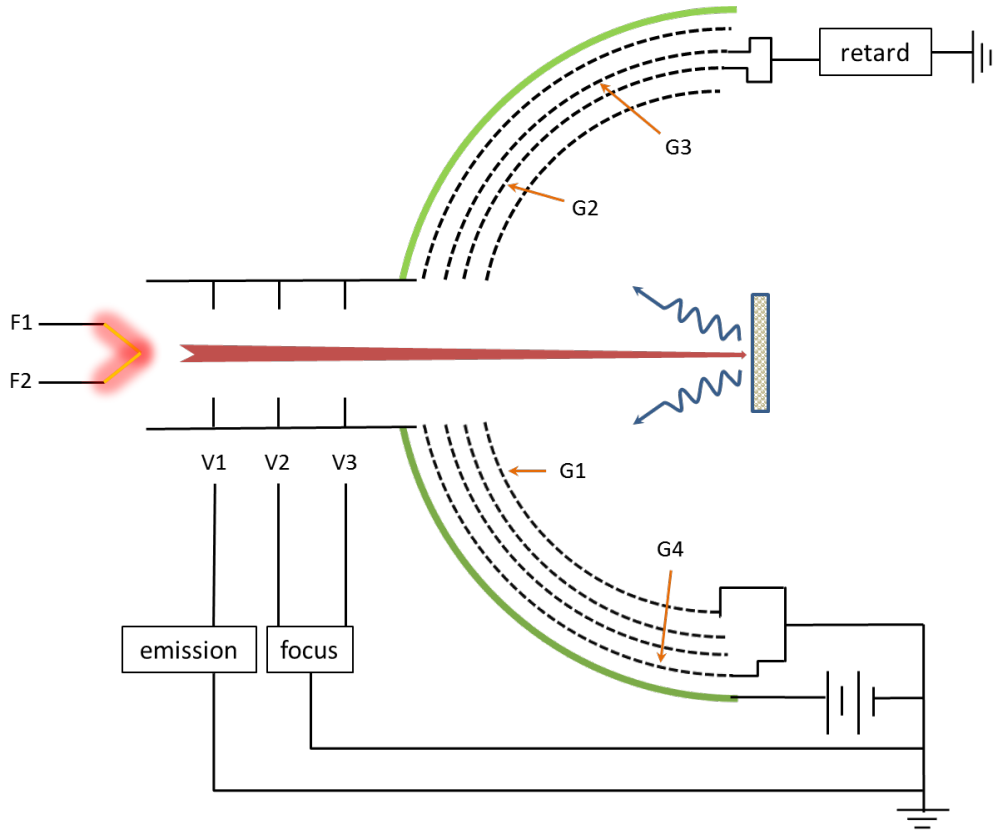

Figure 8: Diagram of the rear-view LEED system, reproduced from the hardware manual. F1 and F2 control the filament current. V1–V3 are the controls for adjusting the electron emission and focusing the beam. G1–G4 are the four grids where G2 and G3 are connected together for retarding the backscattered electrons. A phosphorous screen sits at the back of the grids, held at a high positive potential with respect to ground so that filtered electrons can be accelerated towards the screen to generate the diffraction patterns. Sample is placed at the common center of the spherical grids and screen, and is generally perpendicular to the incident direction.

energy is between 40 eV and 200 eV for studying graphene on SiC and the beam size is about 0.5 mm in diameter. It is important to point out that since the ratio of the total number of electrons being backscattered per incident electron is highly dependent on the incident energy, samples that are not properly grounded or are insulating itself can easily get charged up and generate a large amount of reflected electrons which greatly hinders the differentiability of diffraction patterns on the screen. To study graphene on SiC, the otherwise insulating substrate therefore has to be highly doped.

2.2.3 LEED on Graphene/SiC(0001)

In general LEED images on Gr/SiC samples indicate the degree of surface order. Bright backgrounds with reduced contrast usually imply some long-range disorder on the surface and blurry diffraction spots are indications of small domains with different rotation angles and possibly some contaminants present as well. In addition, approximate graphene layer thickness can be obtained by comparing the relative intensity change between diffraction spots from SiC and the graphene on top. Lattice information can also be easily extracted from the diffraction patterns based on the geometric setup of the LEED optics. On SiC surfaces, measuring the positions of $(1, 0, l)_{SiC}$ rods reveals the backscattering directions of electrons, which can be then compared to the Ewald sphere construction to determine the reciprocal lattice constant; After the inverse transform, real space lattice constant becomes readily known. In reality, such technique is usually used the other way around to calibrate a LEED system based on the known lattice constant. For studies on graphene on SiC, such calibration helps to identify particular diffraction spots corresponding to different kinds of surface reconstruction phases during and after the growth procedures.

As graphene grows very differently on the Si-terminated and C-terminated faces of SiC, LEED images taken from the respective basal planes exhibit distinct characteristics. Figure 9 shows two representative images taken on the two faces. On C-face, graphene grows much faster and usually forms multiple layers on the substrate. However, such graphene layers suffer from stacking disorder that gives arbitrary commensurate interlayer rotation angles. Such phenomenon is easily seen by LEED in Fig. 10a from a multilayer graphene on SiC$(000\bar{1})$ surface, where the diffused ring pattern is consisted of a distribution of $1 \times 1_{Gr}$ spots corresponding to the more or less continuous rotation angles. The six fold symmetry inside the graphene ring is from the SiC substrate $(1 \times 1_{SiC})$, whose weak intensity is a consequence of attenuation from the top graphene layers. Before graphene is formed, the SiC$(000\bar{1})$ surface undergoes a series of reconstructions dependent on the temperature, namely 1×1, 3×3, and 2×2. Such trending is shown in Fig. 10a, from Reference [72]. In contrast, graphene grows much slower on the Si-face where one or two layers of graphene can be controllably formed on the surface, whose LEED pattern are shown in Fig. 10b.

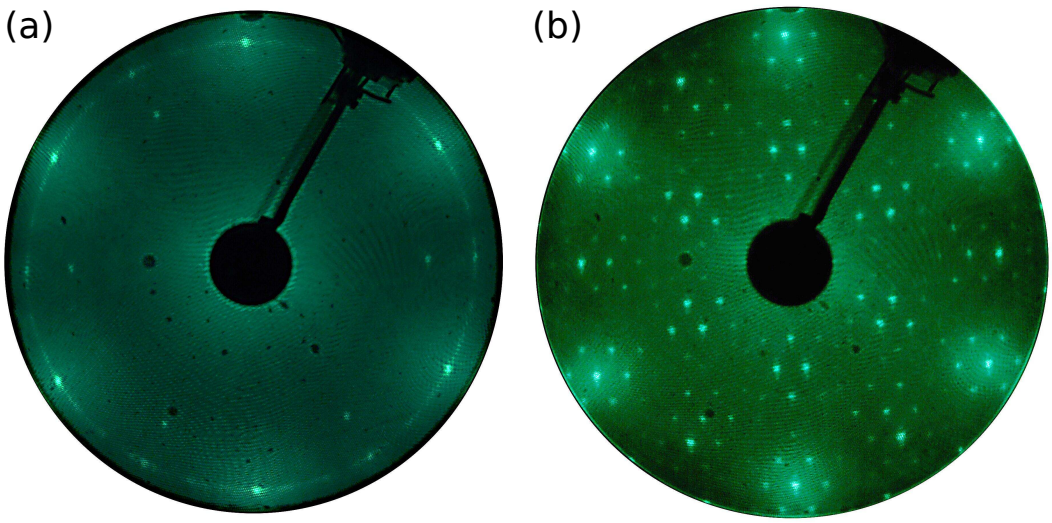

Figure 9: LEED images on (a) C-face SiC surface showing graphene ring outside the weak SiC(1×1) spots and (b) Si-face SiC surface showing clear SiC($6\sqrt{3} \times 6\sqrt{3}\,\mathrm{R30}^\circ$) around SiC($1 \times 1$) and graphene($1 \times 1$). Electron energy is set at 72 eV.

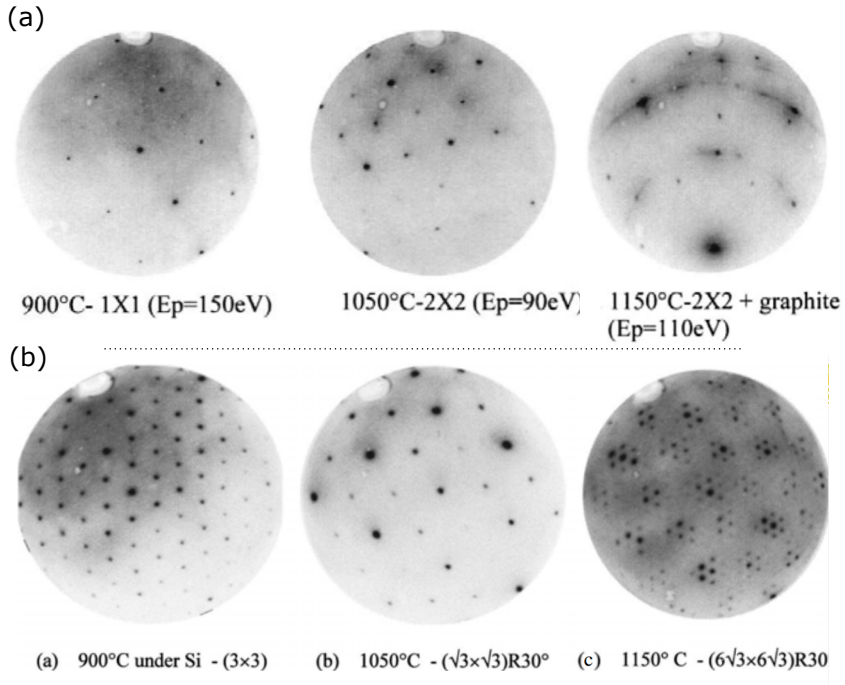

Figure 10: Different surface reconstruction phases during graphene growth on (a) C-face SiC, and (b) Si-face SiC. The figure is adapted from Reference [72].

Similarly, it shows the six fold symmetry from $1 \times 1_{SiC}$ but with a clear $1 \times 1_{Gr}$ rotated at 30°. Such rotation comes from the epitaxy between graphene lattice and SiC. In addition to the primary graphene and SiC rods, satellite spots surrounding them are also observed

associated with the $(6\sqrt{3}\times 6\sqrt{3}\,\mathrm{R30}^\circ)$ reconstructions, which is a unique characteristic of Si-face graphene growth. The SiC substrate also goes through different reconstruction phases during the stages of annealing, the possible LEED patterns including 1×1, $(\sqrt{3}\times\sqrt{3}\,\mathrm{R30}^\circ)$, and $(6\sqrt{3}\times 6\sqrt{3}\,\mathrm{R30}^\circ)$ at different temperatures are shown in Fig. 10b, from [72].

Unfortunately, it is not easy to distinguish GNRs from the rest of the surface under LEED due to the large beam size (0.5 mm). Micro-LEED and LEEM, with much narrow electron beams, will be useful to probe local graphene structures on the surface, and can even provide information about the tilted facets by rotating the sample surfaces.

2.3 Auger Electron Microscopy (AES)

2.3.1 Basic Theory

While LEED is routinely used for getting quick and accurate structural information on 2D surfaces, it lacks the ability of providing fingerprints of chemical compositions. AES, on the other hand, is capable of singling out each chemical element present on the surface and can provide more detailed information about their compound types and layer thickness. The technique is developed in 1960s based on the Auger radiation-less process earlier in 1925 by Pierre Auger. Similar to LEED, AES is making use of impinging electron beams to acquire useful information from the backscattered electrons within a shallow depth from the top surface. A major difference though comes from the fact that AES electrons undergoes inelastic interactions with the surface atoms while LEED is assuming elastic scattering from the samples. The Auger process involves two stages. When an external electron with sufficient energy (a few keV) approaches a surface atom, it excites the atom by creating a vacancy in the core level electrons. The excited atomic state is not stable and quickly decays to a lower energy state by an electron of higher shell levels filling the vacancy. The energy difference between the two states is then adsorbed by another electron from another shell level (Auger electron) to get ionized. When the excitation takes place within a few atomic layers from the top surface, the Auger electron can be possibly emitted from the surface and subsequently collected by the AES detectors. Such process is chemically sensitive because the kinetic energy of the ejected Auger electron is usually characteristic of the parent atoms

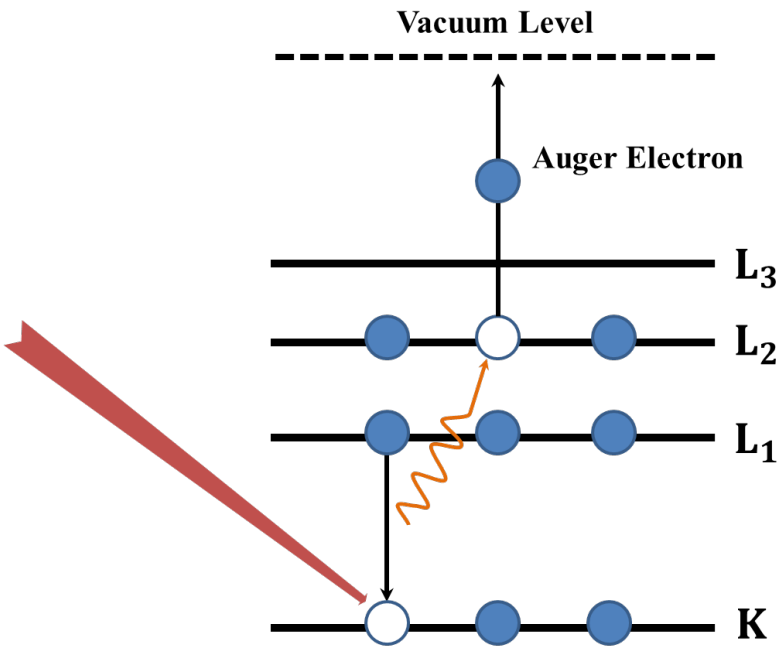

Figure 11: Schematic of a typical KLL process. An incoming electron (red) leaves the surface in a doubly ionized state with the Auger electron acquiring the energy form the electronic transition to leave the surface.

and appears as energy peaks in the detected electron spectrum. This process is highly surface-sensitive because Auger electrons generated in deeper atomic layers undergo a series of scatterings before leaving the surface and thus fail to show the characteristic energy in the collected spectrum. For example, energies in the KLL process follow the relationship:

$$E_{kin} = E_K - E_{L_1} - E_{L_2}, \tag{48}$$

where E_{kin} is the kinetic energy of the Auger electron, E_K is the binding energy of the core level K, E_{L_1} and E_{L_2} are the binding energies for the respective L shells. Cartoons in Fig. 11 better illustrate the Auger process.

Collecting high quality AES spectrum can be challenging. The Auger peaks are usually buried in a rather large background from the as-collected electron spectrum ($N(E)$) due to interferences from the secondary scattering and Auger electrons who lost energies when ejected from the surface. Therefore it would be much easier to collect the derivative ($\frac{dN(E)}{dE}$) of such electronic distributions to enhance the peak features. An alternative derivative ($\frac{d(E \cdot N(E))}{dE}$) is also widely used to account for the higher intensity from the low

energy end associated with secondary electrons. The derivative spectrum can be measured by the modulation technique with an additional lock-in amplifier, where an input energy modulated by a small AC component is used to strike the surface. When the modulation amplitude is small compared to the primary current intensity, higher-order terms in the Taylor expansion of the collected current signal in terms of energy can be neglected, leaving the corresponding output proportional to the derivative $\frac{dN(E)}{dE}$. Figure 12 shows the effectiveness of the technique and is adapted from Reference [73].

2.3.2 Instrumentation

Typical Auager systems are made of an electron gun for generating electron beams, an energy analyzer for sweeping and the beam energy and detect the signals. The RT-STM system is equipped with a Cylindrical Mirror Analyzer(CMA) from Perkin-Elmer PHI model, an Auger Control unit from Physical Electronics, a lock-in amplifier from Princeton Applied Research, and a high voltage supply from NIM for the electron multiplier. A schematic is shown in Fig. 13. While RFA, as introduced in the previous section can also work in the AES mode, it suffers from a poor signal to noise ratio because it only filters out the backscattered electron below a certain energy level. On the contrary, CMA is a much better design for AES in that the two-cylinder structure, labeled as 1 and 2 in Fig. 13, only allows a narrow energy range of electrons to travel through and be detected while both low and high energy electrons will be adsorbed on the two cylindrical walls. By carefully tuning the distance between the two cylinders and their potential difference, such energy bandwidth can be adjusted. The CMA energy resolution is approximately 0.6% of the electron energy. The above statement is based on a one-pass CMA, more advanced designs let electrons 'double pass' through the inner and outer cylinders in a figure-of-eight path, whose second stage filtering aims at eliminating noisy background signals from interactions within the analyzer. By design of CMA, it is much easier to reduce the large background through limited electron passage; and the AC output component from the voltage modulation method can be enhanced by use of a subsequent electron multiplier. Coupling the final output signal to a lock-in amplifier enables direct detection of the differentiated electron spectrum.

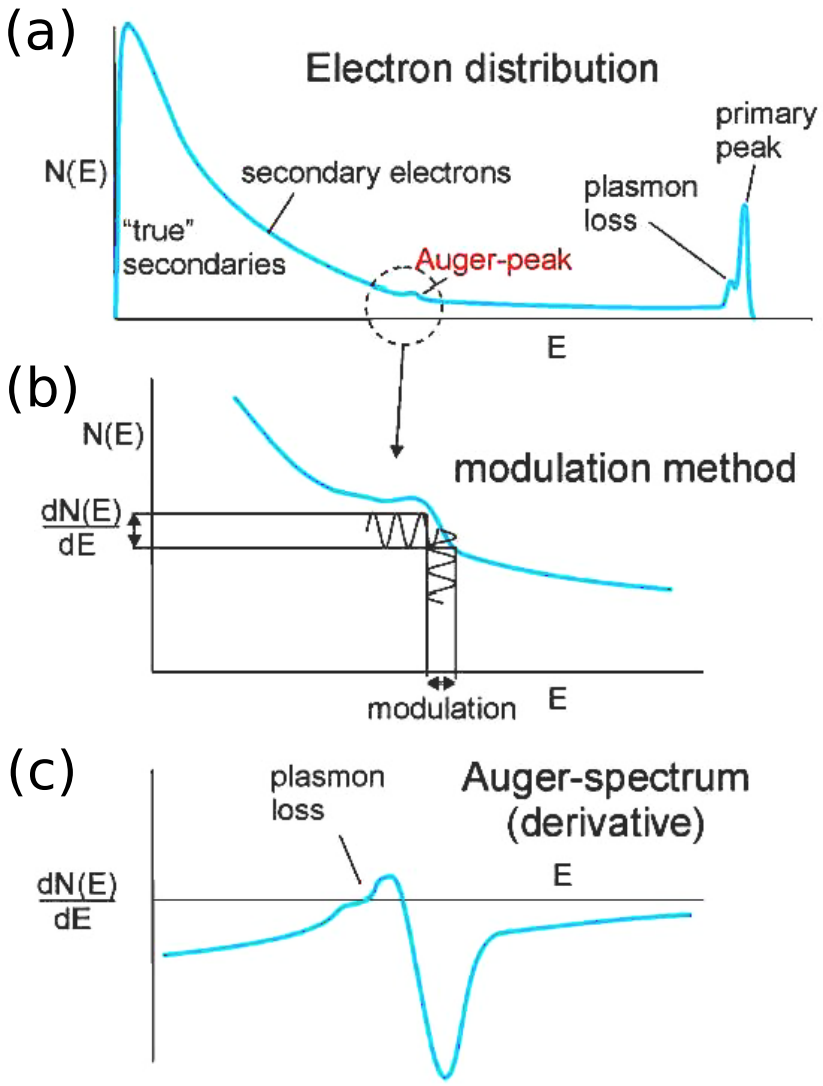

Figure 12: Use of modulation modulation for Auger peak enhancement. (a) an $N(E)$ example with high intensity at low and high energy ends with Auger peaks superimposed. (b) Using the modulation method, local integral of energy distribution is measured at each point. (c) the differentiated spectrum greatly magnifies the Auger peak without energy shift. The figure is adapted from Reference [73]

Similar to LEED, AES requires the sample to be conductive and properly grounded, otherwise the surface charging will add significant background noise to the signals. For insulating surfaces, a grazing incidence can be used to reduce the charging effects. In addition, CMA is particularly sensitive to the spacing and angle between it and the sample surface. For the RT-STM system, the CMA is able to collect reflected beams about 42° from the surface normal. Position of the sample has to be carefully adjusted to maximize

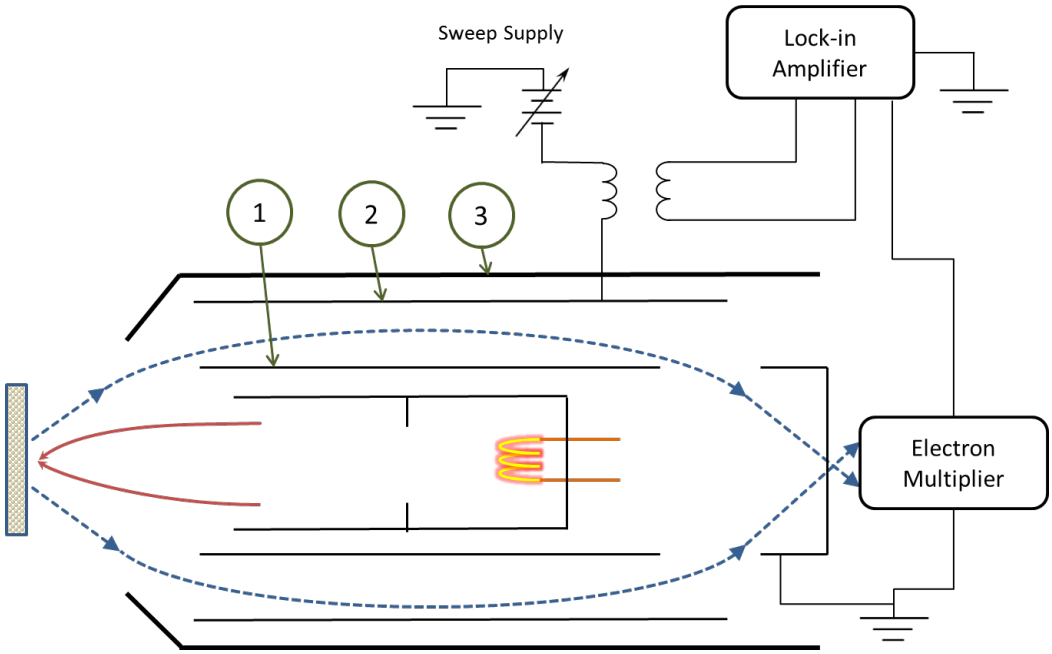

Figure 13: Schematic of the AES setup in RT-STM. The system consists of a CMA analyzer in the center where 1 and 2 are the two cylindrical walls kept at negative potential from the outer cylinder 2 to the inner cylinder 1 and cylinder 3 serves as the overall magnetic shield. Heated filament inside CMA generates the electron beam with emission current around 1.2 mA, the beam undergoes a series of focusing lenses as traveling on the coaxial axis and bombard on the surface. Auger electrons are then emitted towards cylinders 1 and 2 with only those carrying allowed energies can travel through and arrive at the electron multiplier on the other side. Output signal is amplified and transmitted to the lock-in amplifier to by synchronously collected with the energies to form the AES spectrum.

the primarily interested elemental peak intensity prior to full spectral scan.

2.3.3 AES on Graphene/SiC(0001)

AES is particularly useful in obtaining information about surface cleanliness and graphene coverage for studies on graphene on SiC. Normally, AES spectrum on such sample carry three distinctive peaks, namely silicon(LMM) at 88 eV/92 eV, carbon(KLL) at 270 ∼273 eV, and oxygen(KLL) at 502 eV. Oxygen is usually associated with silicon-related oxides with silicon peak appearing around 92 eV in such cases. As the SiC substrate approaches different temperatures during the growth process, it is found that the characteristics of the respective peaks also change significantly with respect to the number of graphene layers formed on the surface. The inset in Fig. 14 shows AES spectrum taken on one sample (HRT002) but heated to different temperatures, from being hydrogen-etched bare SiC , to buffer layer

graphene, and then to more than one layer of graphene. It is obvious that as more and more graphitic carbon forms on the surface, the carbon peak tend to move to a lower energy than the that found on SiC. Moreover, the peak to peak width could grow from 9.6 eV to 22 eV [74, 75]. corresponding to SiC and graphite. Therefore, for a few-layer graphene sample, it is expected that an asymmetric two peak feature near the primary carbon peak could be seen in AES. Lastly, as the peak intensity of specific element is proportional to its surface coverage, it is would be useful to investigate the ratios of silicon to carbon peaks, which indeed varies substantially across samples. As will discussed below, such ratios can be used to quantitatively estimate the number of graphene layers on the surface under the area of the electron beam, and it is factually a standard method for determining thin film thickness grown on a substrate.

Many factors could affect Auger peak intensities including but not limited to sample quality, beam energy, Auger emission probability, efficiency of the analyzer, and modulation parameters (sensitivity, amplitude, and RC constant). Therefore, quantitative analysis of AES data usually deals with relative intensities. One of the most employed quantity is the elemental peak ratios between the thin film and the substrate, which reduces uncertainties pertaining to many of the measurement errors. Since the Auger electrons are attenuated exponentially between each atomic layer, the overall peak intensity is simply the weighted superimposition of contributions from each atomic layer, the calculation of which only relies on three important parameters. Firstly, the averaged electron traveling distances need to be known in order to evaluate the decaying factor. Inelastic mean free paths (IMFP) is usually a reasonable approximation, but it does not account for the possible elastic scattering as the electron travels along, which can be addressed by using the electron attenuation length (EAL) instead. Secondly, the angle that CMA is able to collect electrons with respect to the surface normal is needed for corrections on the IMFP, which is 42° in the setup used here. Lastly, the backscattering matrix factor needs to be identified for each possible chemical environment. To this point, Auger signal intensity for both carbon and silicon under different environment settings can be analytically expressed as a function of the number of atomic layers converted from either IMFP or EAL, the corresponding curve is

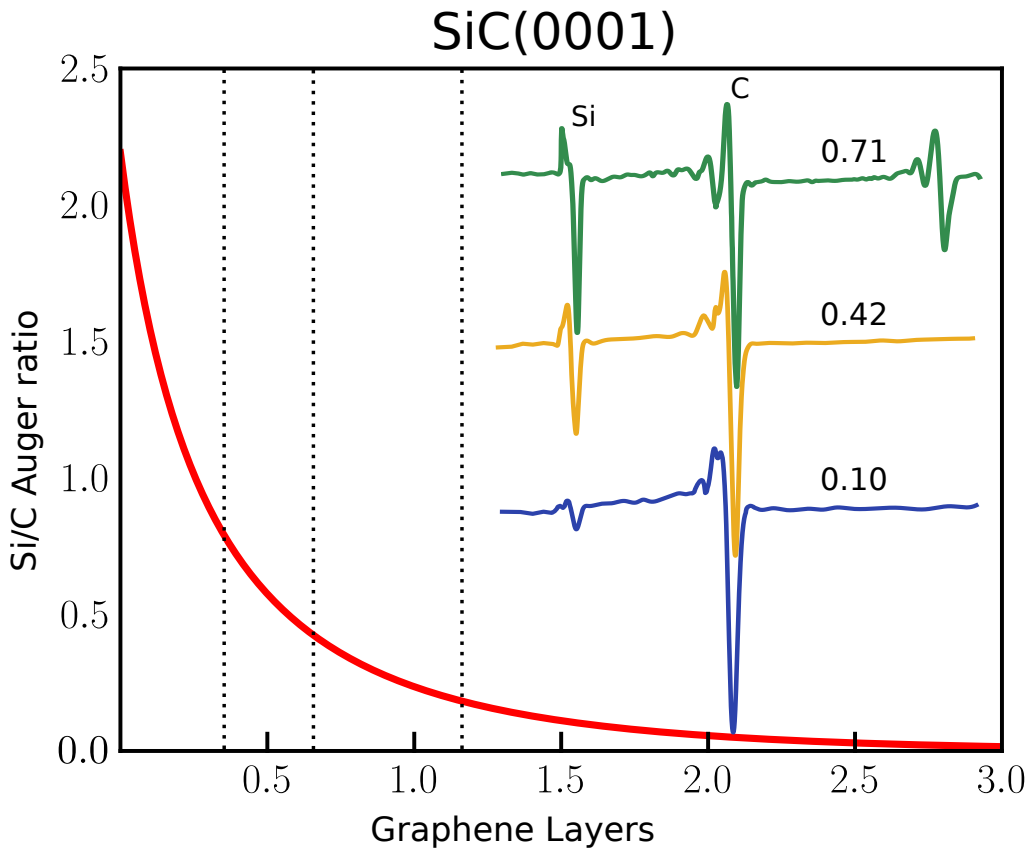

Figure 14: AES attenuation model for graphene thickness estimation. The red curve shows the exponential relationship between Si/C ratio and graphene thickness. The inset shows evolution of AES peaks from one sample being transformed from hydrogen-etched SiC to buffer layer graphene and finally to monolayer graphene. The vertical dashed lines shows the corresponding thickness based on the Si/C ratio values.

plotted in Fig. 14. It is important to note that the model works well only if the film thickness does not exceed the electron escape length, where the Si/C ratio is not approaching zero. More details about the attenuation model can be found in Reference [73].

2.4 Scanning Tunneling Microscopy (STM)

LEED and AES, along with a lot of other popular surface science techniques, haven proven the extraordinary power of electron-based microscopy in accurately uncovering both structural and chemical information at a vertical resolution of a few atomic layers on various materials. However, such techniques still lack the ability to directly visualize atomic lattices of matter and probe the electronic properties on the same scale at the same time. In pursuit of the longstanding dream of seeing the true atoms, Gerd Binnig and Heinrich

Rohrer invented Scanning Tunneling Microscopy (STM) in 1981 and were awarded Nobel prize in physics for their revolutionary masterpiece in 1986, only five years after the first atomic images came out. Ever since then, tremendous efforts have been granted into both experimental and theoretical development of the STM technique. As of today, more than 30 year later, STM is still regarded as the gold standard for exploring materials at the atomic scale.

2.4.1 Principles of Working

STM works by placing a metallic atomically sharp probe/tip close to a conductive sample surface, typically within 10 Å and make various kinds of electric measurements. A voltage difference V is applied between the tip and the sample and the tunnelling current I through the vacuum gap is collected. The sign of the voltage determines the type of electronic surface states explored, which investigates the empty states at positive sample bias and the filled states on the negative side. By the nature of tunnelling, STM current is extremely sensitive to the vacuum gap distance Z, the bias voltage, and the electronic properties on both the tip and the sample. For every 1 Å distance the tip departs the sample surface, the observed current decreases by approximately one order of magnitude. Therefore, although the STM tip radius can be large, up to a few hundred angstroms, atomic scale resolution can still be realized due to fact that the dominant contribution to the tunnelling current usually comes from the apex at the very end of the tip rather than the bulk material. On the other hand, such ultra high sensitivity also means sophisticated mechanical and electronic design are crucial for stabilizing the tunnelling junction between the tip and the surface, which will be discussed later. STM can operate in ambient environment, but maintaining sustainable surface order and reliable high imaging resolution usually requires vacuum and even UHV conditions. One of STM's greatest advantages is its versatile modes of operation other than topographic imaging. Frequently utilized modes include multi-bias imaging, dI/dV spectroscopy, dI/dV mapping, and I-Z measurements.

STM is largely based on the quantum mechanical tunnelling phenomenon, which states that electrons are able to tunnel through an energy barrier between the tip and sample at

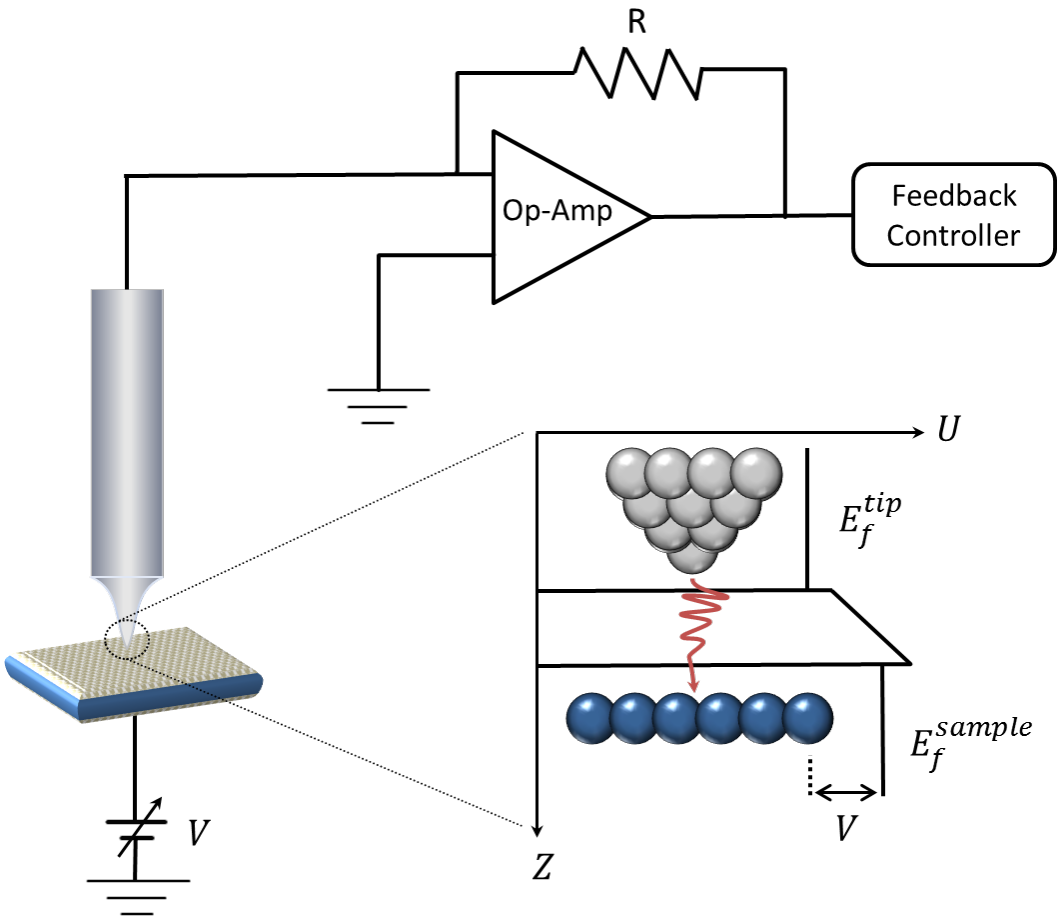

Figure 15: Schematic of a STM tunnel junction. The tip and sample is separated by about 10 Å with the sample connected to a DC voltage supply and the tip connected to an operational amplifier to amplify and convert the tunneling current. The lower right panel shows the energy diagram within the tunnel junction with respect to position.

finite probabilities forming a weak but macroscopically static current. This problem can be simplified into a one-dimensional rectangular quantum barrier problem, which can be easily solved by solving the Schrödinger's Equation,

$$-\frac{\hbar^2}{2m}\frac{\partial^2\psi(z)}{\partial^2 z} + U_B\psi(z) = E\psi(z) \tag{49}$$

$$\psi(z,E) = \psi(0,E)e^{-\kappa z} \tag{50}$$

$$P(z,E) = |\psi(z,E)|^2 \tag{51}$$

$$= |\psi(0,E)|^2 e^{-2\kappa z} \tag{52}$$

$$\kappa = \frac{\sqrt{2m(U_B - E)}}{\hbar} \tag{53}$$

where z is the coordinate perpendicular to the surface, E is the electron energy, U_B is the rectangular barrier height, $\psi(z, E)$ is the electron wave function within the barrier width, and $P(z, E)$ is probability of finding electron at position z, depending exponentially on z. In STM, a bias voltage V is added to one side of the barrier lifting the Fermi level E_f by eV. Hence the tunnelling current is then the overall contribution from electrons going through the lifted barrier with all possible energies E between $E_f - eV$ and E_f.

$$I \approx \sum_{E=E_f-eV}^{E=E_f} |\psi(z, E)|^2 = |\psi(0)|^2 e^{-2\kappa z} \tag{54}$$

Using the local density of states (LDOS) at position z defined by,

$$\rho(z, E) = lim_{\epsilon \to 0} \frac{1}{\epsilon} \sum_{E-\epsilon}^{E} |\psi(z, E)|^2 \tag{55}$$

We can express the current in terms of the LDOS on the sample surface by,

$$I \approx V \rho_s(0, E_f) e^{-2\kappa z} \tag{56}$$

In κ, the barrier height U_B changes as z and V changes ($U_B(z, V)$), but the above derivation assumes the applied bias is much smaller than E_f and thus κ remains constant for all electrons. The expression immediately follows that tunnelling current is exponentially dependent on the tip height from the surface revealing the origin of the ultra high surface sensitivity mentioned earlier.

A more rigorous description of STM tunnelling is from Bardeen and then extend by Tersoff and Hamann based on perturbation theory and Fermi's golden rule. In this approach, the general tunnelling current ($I_{t \to s}$ and $I_{s \to t}$) flowing in both ways between sample (s) and tip (t) are simply the summation of electrons of all energies transition between sample states

and tip states, weighted by the transition probabilities ($R_{t\to s}$ and $R_{s\to t}$):

$$R_{i\to f} = \frac{2\pi}{\hbar}|M_{fi}|^2\delta(E_i - E_f) \tag{57}$$

$$I_{t\to s} = \frac{2\pi e}{\hbar}\int |M_{ts}|^2\rho_t(E-eV)\rho_s(E)f_t(E-eV)[1-f_s(E)]dE \tag{58}$$

$$I_{s\to t} = \frac{2\pi e}{\hbar}\int |M_{ts}|^2\rho_t(E-eV)\rho_s(E)f_s(E)[1-f_t(E-eV)]dE \tag{59}$$

$$I(T,V,z) = |I_{t\to s} - I_{s\to t}| \tag{60}$$

$$= \frac{2\pi e}{\hbar}\int |M_{ts}|^2\rho_t(E-eV)\rho_s(E)[f_s(E) - f_t(E-eV)]dE \tag{61}$$

$$I(T=0) \approx \int_{E_f}^{E_f+eV} |M_{ts}|^2\rho_t(E-eV)\rho_s(E)dE \tag{62}$$

where $f(E)$ is the Fermi-Dirac distribution, $\rho(E)$ is density of states on either sample or the tip, M_{fi} is the symmetric transition matrix between the initial state and the final state, which depends on the barrier height and width as well as temperature. At low temperatures, $f(E)$ is basically a step function, hence comes the approximated zero-temperature tunneling current in Eq. 62, which is a much simplified form but it only becomes useful when a concrete expression is found for M_{ts}.

In Bardeen's approach, sample and tip are treated completely separately as the basis set of the whole tip-sample system, so that the potential U from either one does not affect the electrons near the other. Using time-dependent perturbation, the transition matrix can thus be evaluated as:

$$M_{ts} = \langle\psi_t|U_t|\psi_s\rangle = \frac{\hbar^2}{2m}\int_S (\psi_s\nabla\psi_t^* - \psi_t^*\nabla\psi_s)dS \tag{63}$$

where S is the surface separating tip and sample regions. Such treatment works well for large tip-sample separations where the interaction is indeed weak between them, but it is invalid in the case of a narrow tunnelling barrier. Up to this point M_{ts} is still not in a concrete form that can be easily calculated because the wave functions ϕ_s and ϕ_t are not known.

Tersoff and Hamann made additional assumptions to simplify the M_{ts} calculation. They assume that the primary atom that generates the tunnelling current is in the s state giving rise to an s-wave-function, $\psi_t(r) = \kappa R e^{\kappa R}\frac{e^{-\kappa|\mathbf{r}-\mathbf{r_0}|}}{\kappa|\mathbf{r}-\mathbf{r_0}|}$, where R is the curvature of the tip with

respect to the center $\mathbf{r_0}$ and κ defined earlier. The separating surface S also is presumed to be a 2D plane. For ψ_s, it can be written as a 2D Bloch wave expansion. Using such assumptions, the matrix elements fall into a very simple form:

$$M_{ts} \approx \psi_s(\mathbf{r_0}) \tag{64}$$

The above equation provides a simple description of STM images, which is essentially a map of the density of states on the sample as can be deduced from Eq. 62. However, this approach oversimplifies the tip structure and ignores the finite bias effects of the tunneling current. While the approximated tunnelling current neglects some of the physical details, it still serves as a reasonably good interpretation of STM images.

Finally, a widely-adopted semi-classical solution using one-dimensional WKB approximation states that the potential barrier can be assumed to be trapezoidal and thus the matrix element becomes:

$$|M_{ts}|^2 = e^{-2\int_0^z \sqrt{\frac{2m(\phi+\frac{eV}{2}-E)}{\hbar^2}}dz}, \tag{65}$$

where the equivalent U_B in Eq. 56 is replaced by the averaged work function ϕ from the tip and sample plus contributions from the sample bias $eV/2$. Combining Eq. 62 and Eq. 65, the tunneling current is rewritten as:

$$I \approx \int_{E_f}^{E_f+eV} \rho_t(E-eV)\rho_s(E)e^{\frac{-2z}{\hbar}\sqrt{2m(\phi+\frac{eV}{2}-E)}}dE. \tag{66}$$

2.4.2 Experimental Design

Since the tunnel junction between the tip and the sample is the key to STM, all experimental designs centers around making such junction more *structurally stable*, *mechanically accurate*, *electronically noise-free*, and *chemically clean*. The first thing to consider is the environment an STM would work in. Although STM was originally introduced in air and achieved atomic resolution, ambient environment can be detrimental to reactive surfaces like semiconductors, metals and other functionalized forms due to the rapid surface contamination; in addition, humidity, circulation, and mobile molecules from the air can add obscuring and noisy background in the collected current. Therefore, STM scanner head is

most often placed in UHV chambers so that the insulation layer between the tip and the sample contains almost nothing but emptiness and other useful experimental techniques are readily accessible. In some circumstances, other types of insulating medium becomes better than UHV, such as inert gas for studying chemical processes and liquid-phase materials for exploring biological processes.

In order to operate, the STM tip and sample have to be brought close enough to each other for measurable tunneling current, but not too close for crashing into each other. The normal operating distance is on the order of 10 Å, which means any external mechanical perturbation, if not avoided, could significantly affect the stability of the tunnel junction. What is more, STM aims at achieving lateral resolution equal or better than 1 Å and vertical resolution 0.1 Å, implying potential performance degradation from vibrations in the surrounding environment. Therefore, vibration isolation is the first step to ensure the feasibility of STM. Vibrations come from various sources. Buildings and walls usually give rise to low resonance frequencies below 50 Hz while acoustic waves from people running, air circulation, and etc. can add additional excitations. Line noise around 60 Hz from running electrical machines like vacuum pumps is another common vibration source. Additional sources specific to individual environments also need to be identified, such as spoiling inside dewars and periodic elevator operations. Fortunately, several routes exist to damp out the unwanted mechanical noises. For low frequency vibrations (below 20 Hz), they can be possibly avoided by suspending the STM scanner on massive table supported by pneumatic systems. For medium frequencies ($20 - -200Hz$), tension springs or stacked plates of materials can be used for stage-by-stage damping. Lastly, high-frequency noises (higher than 200 Hz) are usually filtered out by electrical filters, although the best solution is to have the scanner head carrying a high enough resonance frequency so that it can not be easily excited. Both the LT-STM and LT-STM systems used in this study make use of all the strategies as the entire chamber is held on massive air table with the scanner head held by tension spring and viton inserts serving as additional damping; RT-STM is equipped with magnetic damping mechanisms as well. Electrical amplifiers with band-pass filters are used before the signal is recorded.

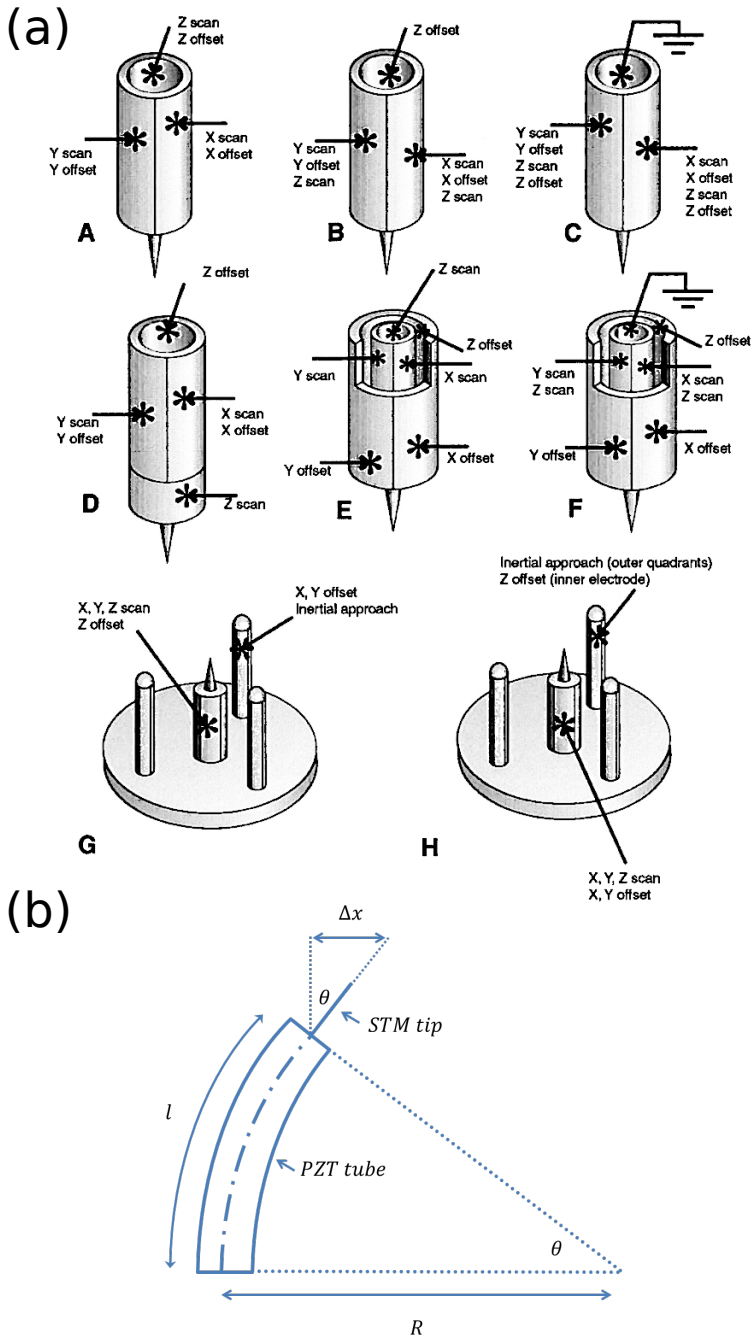

Figure 16: Piezoelectric effects used in STM. (a) Possible scanner designs with single piezo tube and multiple piezo tubes, figure adapted from the RHK-900 manual. (b) Piezo tube bends as a voltage difference is applied across its surface, the horizontal displacement is used for scanning or offsetting in the XY plane. A simple geometric calculation can determine the planetary movement as a function of piezoelectric coefficient, tip length, and voltage

To raster over the sample surface at atomic scale, the STM scanner must be capable of infinitesimal movements. However, to bring the sample and surface close over mm range,

it also need the ability to do coarse motion. Therefore, the movements on a STM stage are jointly controlled by two positioners, a coarse positioner and a fine positioner, both of which are made of Piezoelectric actuators. Piezoelectric effects are the only type of electromechanical effects that provides the high sensitivity STM requires. The most common material is PZT ($Pb[Zr_xTi_{1-x}]O_3$), which can be made UHV-compatible and is free from magnetic effects. The most important factor is that PZT operates at all temperatures from well-above room temperatures to mK range. The PZT coated positioners work by the reverse Piezoelectric effect, where an applied voltage difference (several hundred volts) across the material induces a strain that makes it contract/expand. The type of deformation depends on the direction of the electric field being parallel or anti-parallel to the polarization vector in the material, which is predefined by applying a large electric field to form net ferroelectric polarization, reorient-able through heating. Typical resolution for Piezoelectric materials (Piezoelectric coefficient or PC) is approximately 1 – 4 Å/V at room temperature.

Actual usage of PZT in the STM fine positioner involves one or more PZT tubes that provide all XYZ motions of the tip. Depending on the connection geometry, different types of STM scanners can be designed. In Fig. 16a, some of the possible designs are listed, which is adapted from the RHK-900 controller manual [76]. In our systems, the scanner is made of a single PZT tube with the outer surface consisted of four individual quadrants of PZT and the inner surface a uniform layer. The outer surface controls the XY motions by electrically bending the tube to one side whereas the inner surface uniformly contracts/expands the entire tube to make Z adjustments. Figure 16b shows the movement details. By the nature of the design, XYZ offsets are added to the scanning movements resulting a xy-scan area up to 4 µm by 4 µm and a z-range of 2 µm. It is important to note all the above discussions are for room-temperature scenarios. As the temperature goes lower and lower, scanning become more and more challenging. The key problem stems from much weakened PC and increased friction from frozen adsorbates. For instance, PC on the LT-STM XY scanner is 160Å/V at room temperature but drops to 40Å/V at helium temperature, a factor of 4 difference. It means that low temperature motion is only 25% effective at most compared to the room temperature counterpart. Thus, a higher voltage is need for scanning at low

temperatures and proper calibrations are essential at different working temperatures.

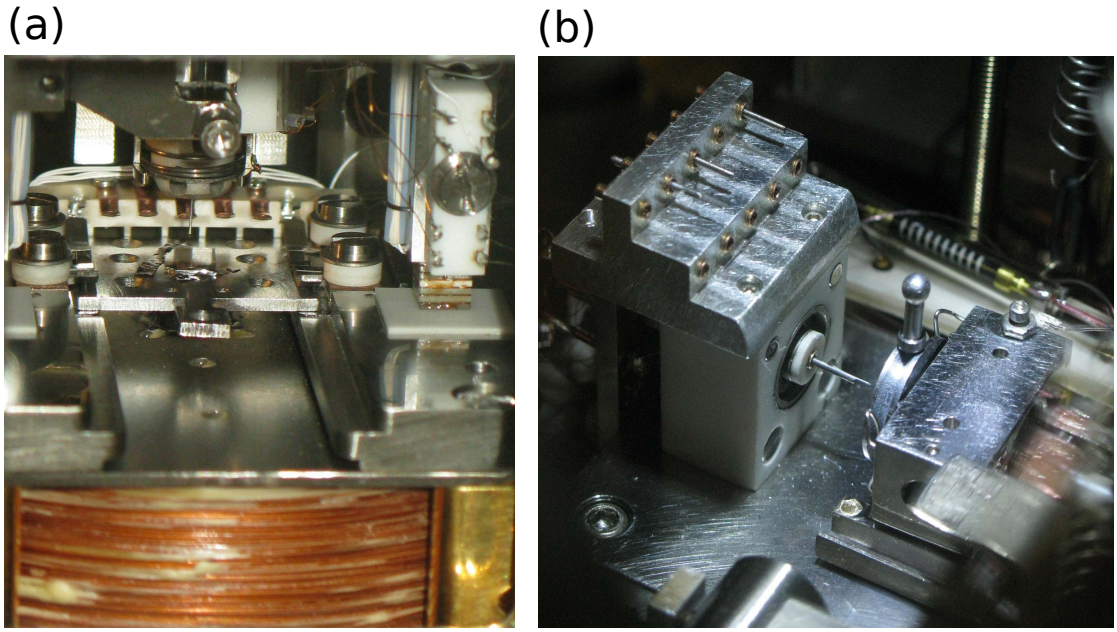

Figure 17: STM scanner head used in this study. (a) LT-STM scanner places the tip vertically and the sample can be slided in and out horizontally in. Multiple contacts are available at the back of the sample insert that enables local transport measurements. A double-layer Dewar is mounted on top that can cool the tunnel junction quickly from elevated temperature to 77 K or 4 K; the copper coils in the bottom provides an vertical magnetic field up to 2 T. (b) RT-STM scanner placed the tip horizontally and the sample can be vertically inserted into a coarse positioner as the Inchworm stepwalker is connected from behind. A single piezo tube is used for the tip that is mounted onto a Macor block with high resonance frequency. Up to ten STM tips can be stored on top of the tunnel junction.

The STM scanner heads for LT-STM and RT-STM are shown in Fig. 17a and b. In RT-STM the sample is pushed horizontally in and out of the tip by a sliding holder connected with a coarse positioner called Inchworm step walker. In contrast, it is the tip in LT-STM that moves vertically via a more modern coarse positioner that avoids the creaking between clamp changes in the stepwalker. Coarse approach brings the tip-sample distance down to μm scale when fine positioners take over to achieve actual tunnelling. Different coarse approach designs have been developed over the years, which categorizes STM into various styles. Two famous ones are the beetle-style rotation design taking advantages of inertial forces and the Pan-style design capable of working in either stepwalker or inertial mode.

Electronics play an instrumental role in STM as it controls the scanning head and collects imaging data simultaneously. The electronics is usually consisted of two parts, a servo that

provides a feedback loop for controlling the tunnelling junction and a high voltage supply sending the voltage signals to the scanner head. The feedback loop in our systems is based on an infinite PID controller loop that compares the collected tunnelling current with a setpoint and calculates an output response from the error voltage based on proportional and accumulated deviations. The response signal is then sent to the Z-channel of the tip for maintaining a constant current (discussed in Section. 2.4.3). In addition to the PID loop, stages of current-to-voltage amplifiers, digital-to-analog converters, and analog-to-digital converters also contribute to the servo construction. More details about building a digital servo can be found in a previous thesis [77].

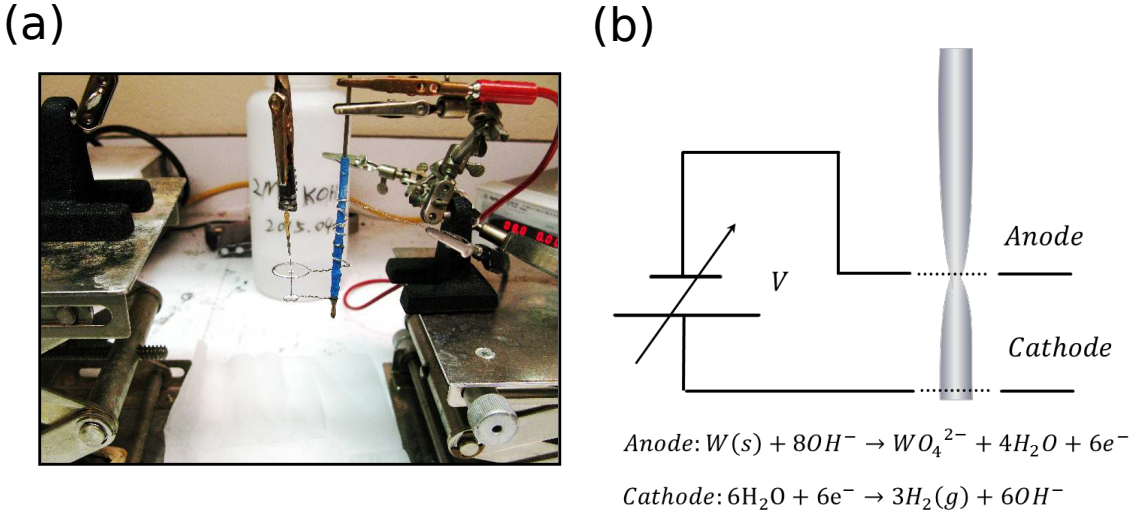

Figure 18: Tip-etching using the double lamellae method. (a) Experimental setup with 2 M KOH used as the etching solution and a 8 V DC voltage supply. The two rings are made of stainless steel wires fixed onto an insulating rod. (b) Equivalent circuit shows the chemical reactions on each electrode. Real etching takes place on the anode while most hydrogen gas is generated from the cathode.

Another important aspect of STM is tip and sample preparation. Sample surfaces are usually either freshly cleaved or grown in-situ shortly before STM measurement. Samples loaded in through air will undergo outgassing at mild temperatures or be sputtered to remove the contaminants on top. Heating in UHV can be achieved by electron bombardment where electrons are accelerated onto the back of samples from a hot filament held at a large negative potential with respect to the samples. Direct current heating is also performed

for some the studies on semiconductors. While recipes for sample preparation are well-investigated depending on the properties of materials present, the STM tip-forming process is not yet fully understood. Typically, STM tips are mainly fabricated from two methods, namely cutting and electrochemical etching. Tips made by using a sharp tip cutter oriented at 45° to basal metal rod are easy and fast to fabricate but frequently suffer from multiple tip imaging and lacks control of the final shape. Therefore, a lot of efforts have been put into developing reliable electrochemical tip etching techniques [78] among which the drop-off method stand out because of its speed, simplicity, and controllability. In this thesis, the double lamellae drop-off method [79] is primarily used for the tip fabrication, whose experimental setup and equivalent circuit are drawn in Fig. 18a and b. A metal rod to be etched is placed vertically on the co-axis of the two rings. By supplying a positive potential on the upper ring and a negative potential on the lower ring with a drop of OH^--containing solution in the ring creating an electrolytic cell the setup forms a complete circuit loop, where sharpening takes place on the upper ring. When the etched part becomes thin enough, gravity pulls the lower rod between the two rings off the rest of the rod creating a taper shape at the end serving as the tip. Advantages of such technique comes from the fact that most tiny bubbles from the hydrogen formation during etching are on the lower ring thus preserving a uniform etching rate on the rod. In addition the mechanical force free electrical connection provided by the two ring setup minimizes the possibility of hook-shaped tip formation. Finally, as the lower part drops off, etching is immediately cutoff due to the incomplete circuit, which does not require any sophisticated circuit breaker and avoids further etching as compared to traditional drop-off methods. After etching, tips are cleaned by water/ethanol streams and put into the loading chamber at 10×10^{-8} mbar. Before STM, tips need to be flashed to a high temperature to break the possible oxide and any other residue on the end. It is also possible to reform and sharpen the tip during tunneling such as dipping into atomic flat silver or gold with field emission performed afterwards. Sometimes, the tip picks up clusters of material from the surface which are loosely attached to the end, such features may be eliminated by mechanical perturbation such as fast scanning at high bias or rapid change in Z positions.

A worthy note on tip formation is that it is not just the sharpness that matters, tip geometry, shape, and chemical composition all contribute to the stability and achievable resolution in STM imaging. Potential improvement on the utilized setup include reducing the thickness of the lamellae so that a smaller contact area between the solution and the tip rod leads to a final taper shape with larger cone angles, more sturdy support of the electrical circuit to avoid vibrations that could break the lamellae, fine control of the distance between the lamellaes to find the optimal length of metal rod that gives sharper and shorter tip ends when dropping off, and additional inert coating on the metal rod near the upper lamellae that can further reduce the contact area giving shorter cone shapes. Usage of single-crystalline metals for STM tips has also been investigated [80].

2.4.3 Modes of Operation

STM is quite versatile in its operation modes. Its primary application is **Topographic Imaging**, which can be achieved in two ways (sample bias is fixed). In Constant Height mode, vertical position of the tip stays unchanged while the current variations as a function of XY spatial positions are recorded as the STM images. However, this mode resembles a slow feedback loop which means it is only useful for imaging atomic flat surfaces but can be operated at high scanning rate. In Constant Current mode, the tunnelling current remains the same by frequent adjustment on the tip z-positions recording STM images of tip heights as a function of XY spatial locations. This mode is widely used by default since it can promptly respond to height variations on the surface without sacrificing the lateral resolution. From Eq. 66, more simplifications can be made to better understand the topography mode. Since most STM tips are made of metals that have relatively flat density of states near their Fermi Levels, $\rho_t(E)$ stays constant and can be extracted from the integral. The barrier height can also stay unchanged as it is largely determined by the sample work function when the sample bias V is much smaller compared to it. So the tunnelling current becomes:

$$I \approx e^{\frac{-2\sqrt{2m\phi}}{\hbar}z}\rho_t(E_f)\int_{E_f}^{E_f+eV}\rho_s(E)dE \tag{67}$$

Under such approximations, STM images under both Constant Current and Constant Height modes are essentially proportional to a constant LDOS map, with extremely high sensitivity to the physical height corrugation due to the exponential factor. Therefore, STM images are always mixtures of true topography and surface electronic states, which are often difficult to distinguish from each other. One possible solution is repeated scanning of identical areas with different biases. examining stationary features between images can provide clues to real structural information.

Point Spectroscopy is another powerful aspect of STM. By fixing the tip height and sweeping the sample bias between a certain voltage range, tunneling current changes can be recorded as one-dimensional $I - V$ curve. However, most of the time it is the first derivatives of such spectroscopic profiles that provide more detailed information about the surface electronic structures, which are typically measured in conjunction with a lock-in amplifier. The dI/dV or differential conductance can be calculated analytically from Eq. 66 as:

$$I(z, V) \approx \rho_t(E_f) \int_{E_f}^{E_f+eV} \rho_s(E) T(z, V, E) dE \tag{68}$$

where,

$$T(z, V, E) = e^{\frac{-2\sqrt{2m\phi + \frac{eV}{2} - E}}{\hbar} z} \tag{69}$$

$$\frac{dI(z, V)}{dV} \approx \rho_t(E_f)[\rho_s(E) T(z, V, E)|_{E=eV} + \int_{E_f}^{E_f+eV} \rho_s(E) \frac{dT(z, V, E)}{dV} dE \tag{70}$$

$$\approx \rho_s(eV) T(z, eV) \tag{71}$$

It follows the assumption that $\rho_t(E)$ stays constant as discussed earlier and $T(z, V, E)$, equivalent to the tunnelling matrix, does not vary much at small biases. Thus, the $dI/dV - V$ spectra is directly related to the surface LDOS at energy eV with z in height, but modulated by the tunnelling matrix. To get rid of the modulation effect, it is sometimes useful to

normalize the spectra by dividing I/V:

$$\frac{dI/dV}{I/V} \approx \frac{T(z,eV)\rho_s(eV)}{1/V\int_{E_f}^{E_f+eV}\rho_s(E)T(z,V,E)dE} \tag{72}$$

$$\approx \frac{\rho_s(eV)}{1/V\int_{E_f}^{E_f+eV}\rho_s(E)dE} \tag{73}$$

$$\frac{dI/dV}{I/V} \propto \rho_s(eV) \tag{74}$$

$T(z,V,E)$ is approximately canceled from the numerator and the denominator to the first order. Also the denominator in the last step can be treated as a constant because it is the average LDOS within the integration range. So it becomes clear that such normalization indeed eliminates the effect of the tunnelling matrix. However, it relies on a continuous finite LDOS of the sample on the denominator, which means semiconducting materials with energy gaps can not use this technique.

Although temperature has not been much involved in the previous formulation, it does play a vital role in limiting the energy resolutions of the spectroscopy data and the voltage values for modulation (V_mod) in dI/dV measurements. Morgenstern, et al [81] have stated that the thermal broadening typically makes the LDOS features wider with a Gaussian width of:

$$\Delta E = \sqrt{(3.3k_BT)^2 + (2.5eV_{mod})^2}. \tag{75}$$

Therefore, at $4.2K$, the best energy resolution is limited at a few meV and the modulation voltage should be on the same scale. At $300K$, however, broadening effects become significant as the best energy resolution is on the order of 100 meV.

Point spectroscopy can be easily extended into a 2D version which is often referred to as **Differential Conductance Mapping** (dI/dV mapping). In this mode, dI/dV spectroscopy is recorded at each location the STM tip scans across a surface area and a topographic image is taken simultaneously. The actual process can be performed in two distinct fashions, namely the open-loop and closed-loop approaches. The open-loop method is usually good for high energy resolution mapping but takes a tediously long time to finish while the closed-loop method is often used for getting quick LDOS information on a large

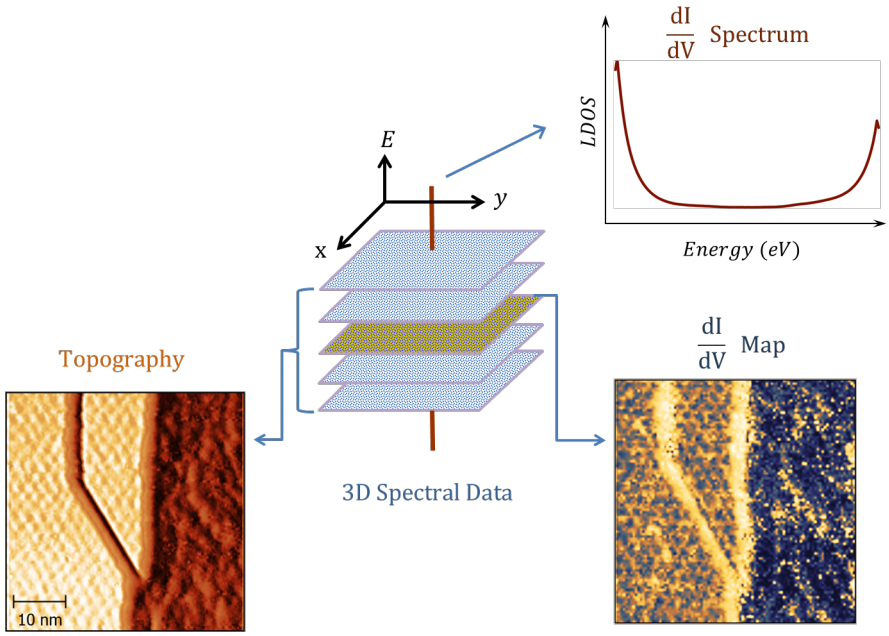

Figure 19: dI/dV mapping in STM. The collected data is 3-dimensional with the xy being the spatial locations and E being the energies in each spectra at each location. An topography image is taken at the same time so that correlations between space and density of states can be deduced. Point STS can be extracted at each location along the energy axis while DOS maps can be extracted at each energy point slicing parallel to the xy plane.

scale at energies around the bias setpoint. The collected data is then essentially three-dimensional with the XY dimensions showing the spatial information and the Z dimension covering the LDOS features. One therefore can think of the dI/dV mapping as taking energy slices of spatial distributions of LDOS on the surface which has proven to be extremely helpful in understanding carrier scattering process, electron density distribution, defects, and so on. In addition to examining dI/dV maps directly, Fourier transform analysis is also a great tool for extract more information in the data. Since the LDOS are measured against spatial positions, Fourier transformation results in showing features in the momentum space, which is directly related to wave vectors of electrons. By combining such transformed maps at different energies, an $E(k)$ relationship can be established providing direct insights into the band structures of materials at nanometer scale. A schematic in Fig. 19 better illustrate the mapping mode.

I-Z measurement mode is the last operation mode will be discussed, though a lot more can be found within the STM community. The $I - Z$ mode involves pulling the STM tip

away from the sample at fixed z-steps while collecting the changing current (feedback loop on hold). The physical meaning of such measurement can be easily seen from $d(lnI)/dz$:

$$\frac{d(lnI)}{dz} \approx \frac{d(ln(\rho_t(E_f)\int_{E_f}^{E_f+eV}\rho_s(E)dE + \frac{-2\sqrt{2m\phi}}{\hbar}z))}{dz} \tag{76}$$

$$\approx \sqrt{\phi} \tag{77}$$

Apparently, the logarithmic derivative $d(lnI)/dz$ measures the equivalent work function of the sample surface. By measuring such spectra at decreasing sample biases until an ohmic contact is observed, a good estimate of the tunneling gap Δz can be obtained. It is also possible to map the work function distribution within a scanning area, this is particularly helpful in studying heterostructure and their interfacial effects.

The original STM has inspired numerous new STM designs for exploring additional information such as chemical potential, magnetic structure, and but not limited to transport properties. Popular modified STM setups include spin-polarized STM, 4-probe point contact STM, scanning tunneling potentiometry, and so on. The core vibration control and feedback loop also simulated development of other related microscopy techniques, such as Atomic Force Microscopy, Magnetic Force Microscopy, Lateral Force Microscopy, just to name a few. After almost 40 years of invention, STM research is still a booming and exciting field, whose future can only be brighter.

2.4.4 STM on Graphene/SiC(0001)

The Graphene/SiC(0001) system can appear quite differently under STM depending on its growth environment and number of graphene layers on top. High resolution STM image are typically more easily acquired on UHV-grown graphene on SiC(0001), which is believed to be much cleaner than the furnace-grown alternative. As has been discussed in the previous chapter, graphene forms an interface buffer layer on SiC(0001) underneath the first electronically real graphene monolayer. The buffer layer which gives $6\sqrt{3}\times 6\sqrt{3}$ reconstructions in LEED are however typically imaged as 6×6 periods under STM, as can be seen from the larger scale hexagonally distributed depressions in Fig. 20a. The discrepancy is mainly caused by the tunneling condition where high bias imaging tends to give more pronounced

6×6 periods while low bias imaging ($< 1.5V$) uncovers the detailed $6\sqrt{3} \times 6\sqrt{3}$ structures. In addition, the 6×6 intensity also weakens quickly as more graphene layers form on top. Figure 21a, with sample bias set at $-1.5V$, shows the fine details in the $6\sqrt{3} \times 6\sqrt{3}$ reconstruction which mainly represent protrusions in the local electron density. True atomic structure of buffer layer graphene is not fully understood and not directly imaged by STM either. For layer-1 graphene, the first graphene layer on top of buffer layer, atomic lattice are usually imaged with a background corrugation from the buffer layer. This is best illustrated in Fig. 20c that individual graphene hexagons are clearly identified but the longer-range height variations assume a18.7 Å (6×6) periodicity. Top left corner of Fig. 20c shows abnormal periodic patterns that correspond to the commonly observed $\sqrt{3} \times \sqrt{3}$ electron scattering at graphene boundaries, which is along the armchair direction in this case. STM has been widely used for studying such scattering processes along inhomogeneous boundaries and around surface defects. Another type of boundary comes from surface steps, STM has given evidences that graphene lattice can grow continuously over small step edges as seen in Fig. 21b from a 2.5 Å atomic step, but for large steps tens of nm in height, related work is deficient and it is going to be a key question this thesis is dedicated to answer. For few-layer graphene samples, triangular lattice features can be found under STM due to the Bernal stacking order of graphene layers on SiC(0001), in comparison to the rhombohedral stacking scheme on SiC($000\bar{1}$).

Spectroscopy also shows rich features in the Graphene/SiC(0001) system. Due to the charge transfer between SiC substrate and graphene, an n-type doping is typically observed in STS which appears as a shoulder around $-0.5V$. Figure 20b and d both show such features. Apart from this common observation, STS on buffer layer usually renders a considerably low density of states around $0V$ indicating its strong interaction with the substrate, whereas monolayer graphene samples show the theoretical linear dispersion in STS at low energies approximately between ± 500 mV. At higher voltages, the STS is usually asymmetric with the negative bias side lower than the positive side, which can be explained as the nonequivalence in filled and empty states in the tunneling matrix. As more graphene layers are added, the system's band structure heavily deviates from the

linear dispersion with STS usually giving parabolic curves.

Various quantized electronic states can also rise up as a result of different graphene geometries. For example, Fig. 20b shows a bandgap around 0.3 V on the graphene island because of the quantum confinement effect. Localized states due to edge terminations on GNRs are also frequently observed. In addition surface strain, substrate interaction, and defects can all add features in STS data. As a reference, typical appearance of STS taken on buffer layer and monolayer graphene on SiC can be found in [82–85].

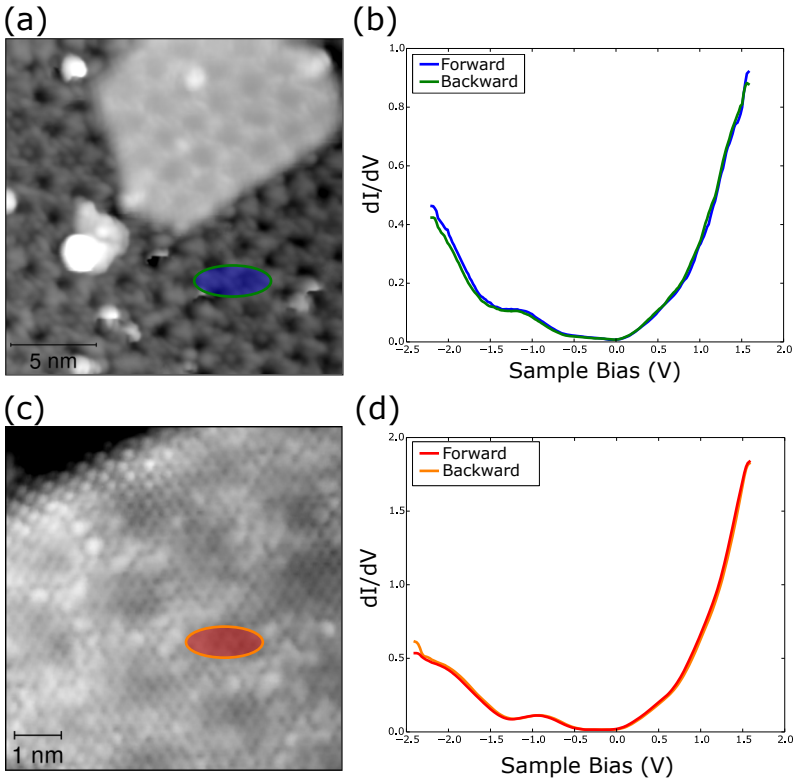

Figure 20: STM on monolayer and buffer layer graphene. (a)Topography image showing a graphene island in the top right corner surrounded by buffer layer, 6×6 patterns can be resolved ($-2\,\mathrm{V}$, $40\,\mathrm{pA}$). (b) Spatially averaged STS on buffer layer in a. (c) Atomic imaging near the edge of the graphene island in a showing the graphene lattice on top of the 6×6 periods; edge scattering is observed along the edge in the top left corner of the image ($-1\,\mathrm{V}$, $40\,\mathrm{pA}$). (d) Spatially averaged STS on the graphene island in c; a bandgap is observed near the center.

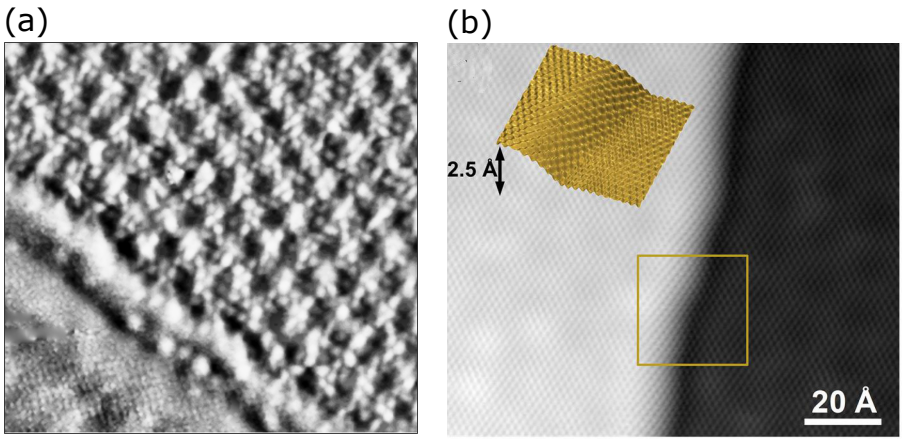

Figure 21: STM on graphene near step edges. (a) Topography image taken at sample bias $-1.5V$ shows more fine structures related to $(6\sqrt{3} \times 6\sqrt{3}\,\mathrm{R30°})$ in addition to the 6×6 periods. (b) Graphene lattice grows seamlessly over a small step edge,2.5 Å high. A 3D cartoon is shown for the inset region. b is adapted from [82].

CHAPTER III

GRAPHENE NANORIBBONS GROWN ON SiC(0001)

As discussed in previous chapters, graphene nanoribbons open up the door for integrating bandgap engineering with the intrinsic transport properties of bulk graphene. In particular, epitaxial sidewall graphene nanoribbons grown on SiC, unlike the other alternatives, reduces edge roughness, provides better width control by the nanostep heights, and shows ballistic transport properties. However, the GNR structural dependence on the step directions, its electronic structures, as well as origins of the ballistic transport channels remain unclear. To understand the epitaxial sidewall graphene system in more detail, a local experimental method is required. STM is an ideal choice to probe both the topographical and electronic structures of this system. In this chapter, we discuss different ways of imposing nanosteps of different heights on the SiC(0001) surface from which graphene nanoribbons are grown using the confinement controlled sublimation method. From STM imaging, we observe different step formations and graphene growth near the steps. Significant electronic states are also observed by STS and are explained by various local effects present in the system.

3.1 Sample Preparation

People have found evidence that the growth of graphene preferably starts at step edges on SiC and hence the graphene nucleation density is high [68]. If the growth temperature, time, and atmosphere can be carefully controlled, it is possible that graphene would form in a stripe form along the step directions and eventually grow into nanoribbons on large scale surface steps [68]. Therefore, imposing step structures on SiC surface serves as a crucial role in controlling the morphology and quality of graphene nanoribbons grown on top of them.

An important advantage of epitaxial sidewall graphene nanoribbons is the ability of controlling the ribbon width through SiC step heights. One way to create large SiC steps

($\geq$ 10 nm in height) is by controlling the experimental conditions during the hydrogen-etching phase or graphene growth process so that the initial atomic steps quickly flow and self organize into a single uniform step, which is also called step bunching [168, 177]. The other way of achieving a large step height is to use standard lithography and ion etching techniques to define vertical trench structures on the SiC surface that will later evolve into low-energy nanofacets during the high temperature annealing.

3.1.1 Self-organized GNRs

Step bunching on 4H- and 6H- SiC has been observed and studied for more than 2 decades. Research has found that the normal Si-C bilayer steps (2.5 Å) on the surface tend to coalesce into larger steps such as half or full unit cell high steps (microsteps) after high temperature annealing [168, 179] Under certain conditions, they can form even larger steps with increased heights up to tens of nanometers (macrosteps) [111, 168]. While it is an interesting observation, anisotropic step bunching is detrimental to traditional electronic devices in that the step-bunched SiC substrates introduce undesirable microroughness at the junctions of terraces which greatly lowers carrier mobility and affects additional device overlayers, resulting in degraded performances [104, 144]. In the case of epitaxial GNRs, however, one can instead make use of the otherwise problematic step bunching process to establish regularly stepped arrays on the surface with controlled heights to grow GNRs only along the step edges. Transistor circuits can be built on these GNRs by depositing dielectric layers and metal gates [68].

To understand the mechanism behind the observed step-bunching process, one has to note that atomic steps present on SiC substrates tend to diffuse (stepflow) at different rates under elevated temperatures including hydrogen etching and epitaxial growth processes, due to surface instabilities such as step kinetics, step stiffness, step-step interactions, and so on [164, 167]. Monte Carlo simulations [160] have shown that there are six different stepflow velocities corresponding to the three inequivalent terraces and two distinct step edges on a 6H-SiC(0001) surface. Similar conclusions can also be made for 4H-SiC surfaces. Different surface energies can be explained as the reason for different diffusion velocities between Si-C

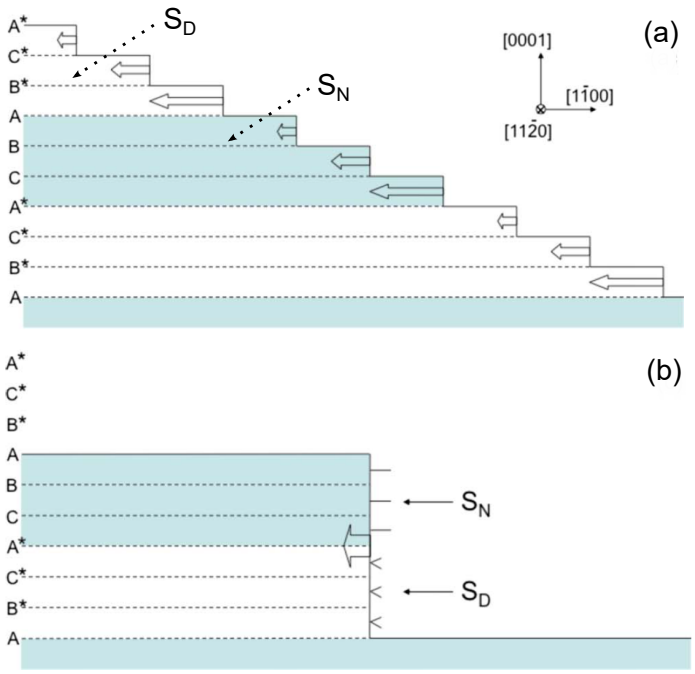

Figure 22: A schematic showing the stepflow process on 6H-SiC(0001): (a) the three inequivalent SiC bi-layers have different stepflow velocities and there are two types of steps S_N and S_D with different edge terminations; (b) the outcome of the stepflow-induced step bunching results in a full unit-cell height step; The figure is adapted from [160].

bilayers [96, 132, 196], which causes the steps to rearrange into a 'hill and valley' structure forming low-index nanofacets during growth or etching to minimize the overall surface energy. It is generally believed that surface energies on C-face are lower than Si-face since C-face are experimentally found much less prone to step bunching [143, 144, 216]. Therefore, in the application of GNR on SiC, Si-face SiC serves as a better candidate substrate for creating higher steps and providing better control of number of graphene layers during growth.

The first sample (25ed30 [223]) studied is from a nominally on-axis conductive (0.015 – 0.028 $\Omega \cdot$ cm) 4H-SiC(0001) substrate, where GNRs are grown directly on the flat surface by annealing at 1500°C for 9 min. Steps on the surface are extensively bunched together during graphene growth. As the substrate has a small miscut angle 0.1° from the $\langle 11\bar{2}0 \rangle$ direction, most bunched step facets have Miller index $(11\bar{2}n)$. As can be seen from AFM images taken on the sample, surface step heights can go up to 20 nm. Moreover, monolayer graphene is mainly found near the step edges as revealed by EFM measurements comparing

before growth and after growth (contributions from the work function change in SiC basal planes is therefore minor), where the contrast differences are mainly caused by the work function change between SiC terraces and graphene-covered sidewall nanofacets. STM and STS measurements are also performed on the sample to investigate the electronic properties of the sidewall graphene which will be explained in detail in later sections.

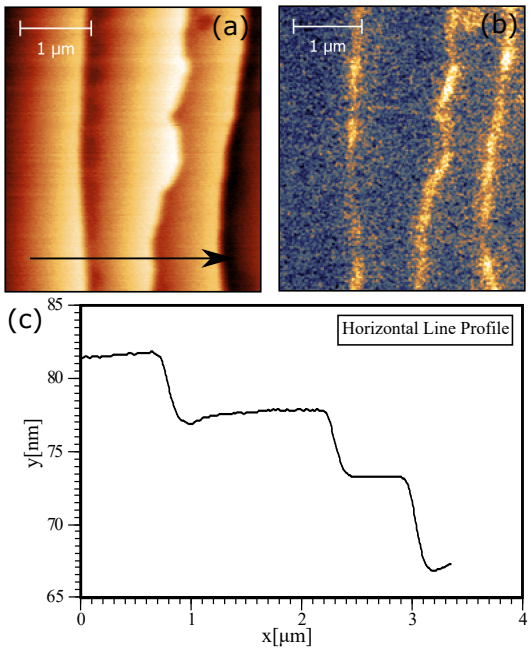

Figure 23: AFM and EFM images from sample 25ed30: (a) AFM image shows the step bunching on the surface, relatively straight bunched steps up to 8-nm high can be seen. (b) EFM image shows that steps edges are higher in electrostatic force signal compared to the rest of the surface, serving as an indication that graphene is only present near the step edges while the terraces are possibly covered with buffer layer. (c) Horizontal line profile across (a) showing the bunched step heights.

Achieving simultaneous step bunching and sidewall graphene formation is convenient and efficient. However, it is difficult to control the exact growth conditions and hence the results may not be reproducible. A different approach would be pre-forming regular step arrays on SiC surface and inducing step bunching through high temperature hydrogen etching which both increases surface smoothness and reduces microsteps on the surface. A second sample, T79 [223], is from an off-axis conductive 6H-SiC(0001) substrate which has a miscut angle of a few degrees towards $(11\bar{2}0)$ (for more details about the four index Miller-Bravais convention, see Refs. [87, 162]). Off-axis SiC surfaces are more prone to step bunching and

can potentially produce high quality large steps [115, 202]. The growth results are consistent with the literatures which shows wide flat terraces connected by single bunched step structures as high as 40 nm under AFM imaging [115, 202]. EFM measurements again show work function changes along the step edges due to sidewall graphene formation.

T79 exhibits promising potential of vicinal SiC substrates in epitaxial GNR growth on large surface steps, however, the miscut angle is fixed which limits the bunched step to similar angles and heights. To form nanofacets on steps of different heights and directions, and study the different GNRs formed there, a vicinal surface that incorporates different miscut angles is necessary. In sample HDS009 (on-axis conductive 6H-SC(0001) [223]), surface grinding is utilized to impose a spherical dimple structure in the substrate, the curve of which gives continuously changing miscut angles. Grinding is done in a TEM dimple grinder (Gatan 656) with the sample mounted on a steel chuck via wax (Crystal Bond 509) and coated with diamond compound (Kay Diamond). Followed by initial dimple formation, subsequent mechanical polishing is performed to reduce grinding damages. The overall procedure produces a 30 μm in depth and 1mm in diameter dimple in the center of HDS009, as shown in Fig. 26a. After high temperature hydrogen etching, extensive step bunching are observed under AFM (shown in Fig. 26b). It is clear that step density changes at different positions in the dimple which lead to bunched steps of different heights and angles, can be useful for exploring the relationship between step bunching/graphene growth and local surface angles. Due to the circular shape of the dimple, step bunching can take place in different directions on the surface and are relatively straight compared to local curvatures, which opens up the opportunity to study GNRs grown along different step edge terminations.

3.1.2 Lithography Patterned GNRs

Self-organized step bunching provides large steps of decent quality through a simple procedure, but they lack the ability to precisely control the height, position, and density of the formed step structures. In contrast, lithography patterning has long been used to define artificial structures on a surface with nanoscale precision. This process can easily create

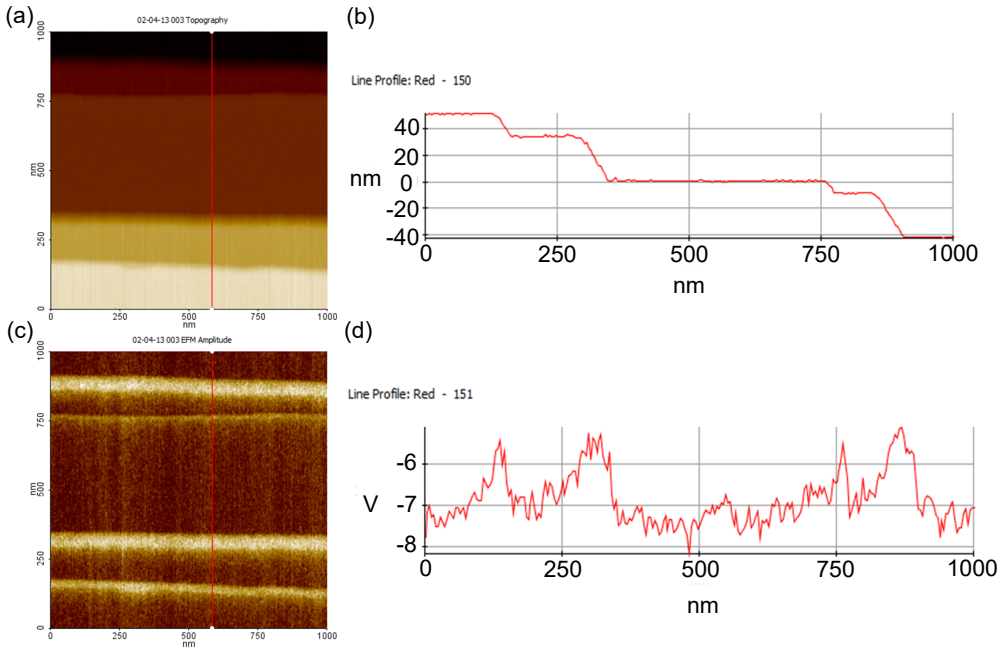

Figure 24: AFM and EFM images from sample T79: (a) AFM image shows the step bunching on the surface, horizontally bunched large steps of 40 nm high with wide flat terraces. (b) Vertical line profile across (a) showing the bunched step heights. (c) EFM image shows that steps edges are about 2V higher in electrostatic force signal, consistent with observations from 25ed30. (d) Line profile across c, showing the signal differences.

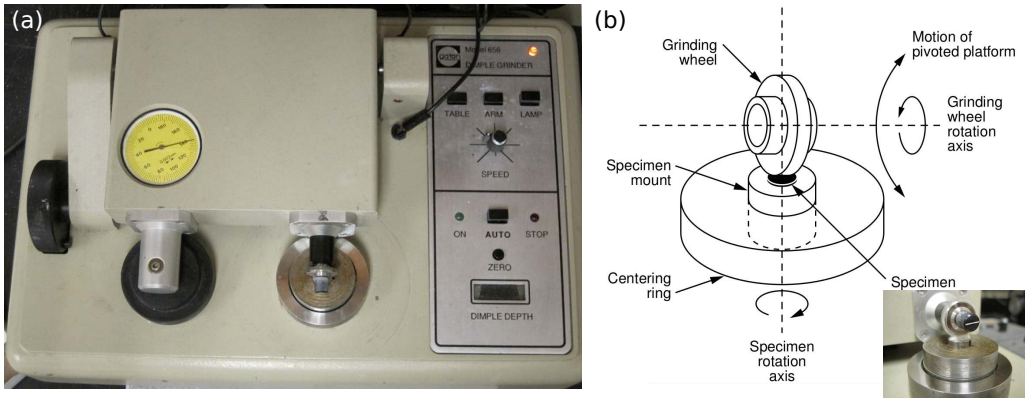

Figure 25: Dimple grinder used for making HDS009 (a) Gatan 656 dimple grinder (grinding speed, force, and wheels can be adjusted; dimple depth can be monitored); (b) Schematic showing the grinding head with a grinding wheel spinning perpendicular to the specimen normal and the stage rotating about the specimen surface normal; the inset shows the actual grinding process, compounds are added between the sample and wheel.

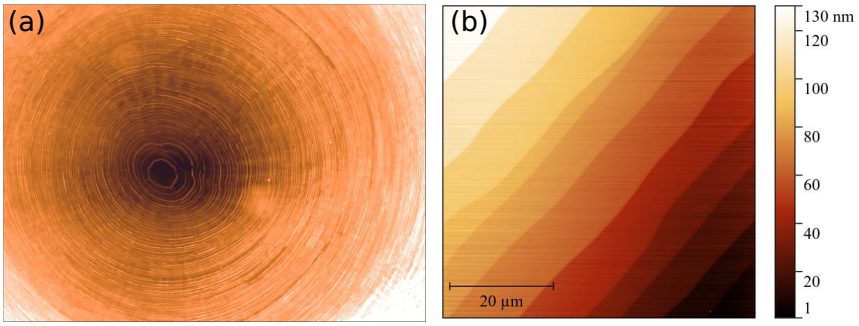

Figure 26: surface characterization of dimpled samples (a) dimple structure under an optical microscope can be readily seen. The surface is relatively smooth and steps circulating around the center can be identified. (b) AFM image of a typical dimpled sample after hydrogen-etching which gives straight and smooth bunched steps. The heights are on average 10 to 15 nm.

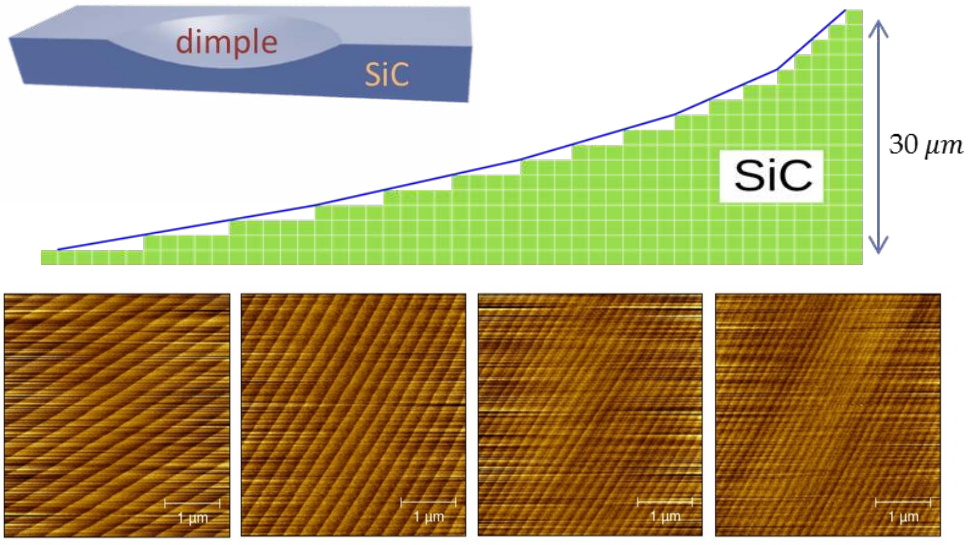

Figure 27: The HDS009 surface. The top pane plots a schematic showing the dimple structure in the center of the sample which is 30 μm in depth and 1 mm in diameter. The bottom pane compares step densities at different locations/heights in the dimple as approximately indicated by the cross-sectional cartoon in the middle; it clearly demonstrates that step density becomes higher and higher while terrace width becomes smaller and smaller as going from the bottom to the top of the dimple.

densely-packed and aligned features on the surface that are ideal for further device fabrication. For this study, electron beam lithography (EBL) and reactive ion etching (RIE) are used for creating arrays of trench structures into the SiC substrate. After removing the residue from the patterning process, the sample is graphitized using the CCS method similar to the self-organized GNRs.

Samples are firstly spin-coated with photoresist and then CAD-designed arrays of lines are patterned by EBL along a particular direction ($\langle 11\bar{2}0\rangle$ or $\langle 1\bar{1}00\rangle$). After exposure and development, samples are transferred into a conventional RIE system with $SF_6 - O_2 - Ar$ plasma for etching away the unmasked regions. Lastly, residual resist is removed by dipping into buffered oxide etch (BOE) and subsequent selective graphitization process follows. Figure 28a shows the schematic and the actual trenches under AFM right after the patterning process. During high temperature growth, the vertical step edges begin flowing and organize into particular higher-order nanofacets, where graphene preferentially forms due to the instabilities of Si atoms with more dangling bonds on these crystal planes. The outcome is examined by EFM measurements, which confirms that graphene only forms along the step edges, and terraces away from them are essentially only covered with buffer layer. Sample EDJP1 (zigzag-direction), 4HNNA (zigzag-direction) [223] are all processed in this manner with slight differences in patterning and growth parameters. Substrates used on these samples are on-axis conductive 4H-SiC(0001).

3.1.3 In-vacuum Preparation

All samples are grown by confinement controlled sublimation (CCS) method in a home-built low-vacuum CCS furnace [182]. 25ed30 and HDS009 are hydrogen etched in the CCS furnace prior to growth; patterned samples are firstly annealed at 1100°C to stabilize the trench facets. To limit graphene formation only along the step edges, growth parameters are carefully tuned. It is found that higher temperature (1500°C– 1570°C) and shorter graphitization time (1 min – 9 min) tend to give both good-quality step bunching and selective graphene formation over the sidewalls.

All samples are kept in air for certain periods from 1 to 30 days before transferred into

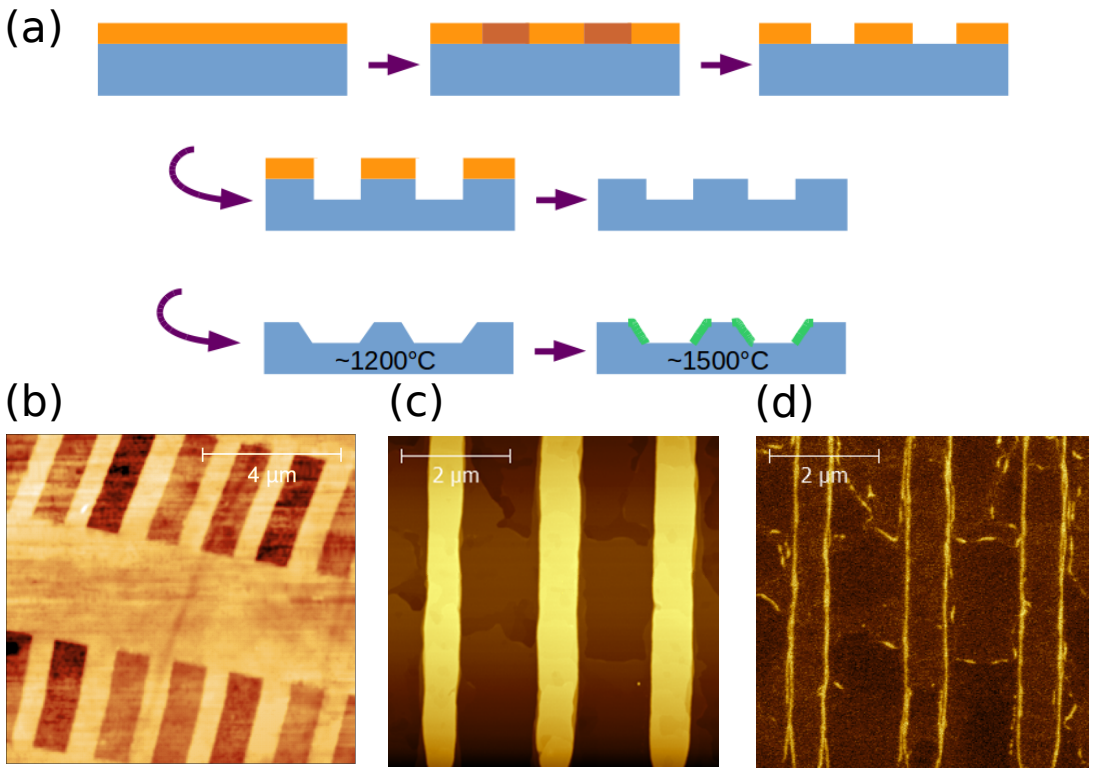

Figure 28: GNR samples using lithography patterning (a) lithography patterning process involves spincoating, development, plasma-etching, lift-off cleaning, nanofaceting, and graphene growth, each corresponding to one of the staged cartoons. (b) AFM image right after the patterning is finished showing rectangular step structures imposed on the surface. (c) AFM image after high temperature growth showing all structures are rounded and the steep step edges are faceted (d) EFM image shows a distinct difference between step edges and the terraces indicating limited graphene growth only near the nanofacets.

a UHV system for further characterizations. Samples are initially outgassed at 500°C for a few hours to eliminate potential water and other molecules picked up from the ambient environment, after which it is annealed again at 800°C to 850°C for 20 minutes. LEED and AES measurement are conducted to characterize the graphene coverage and chemical composition on the surfaces.

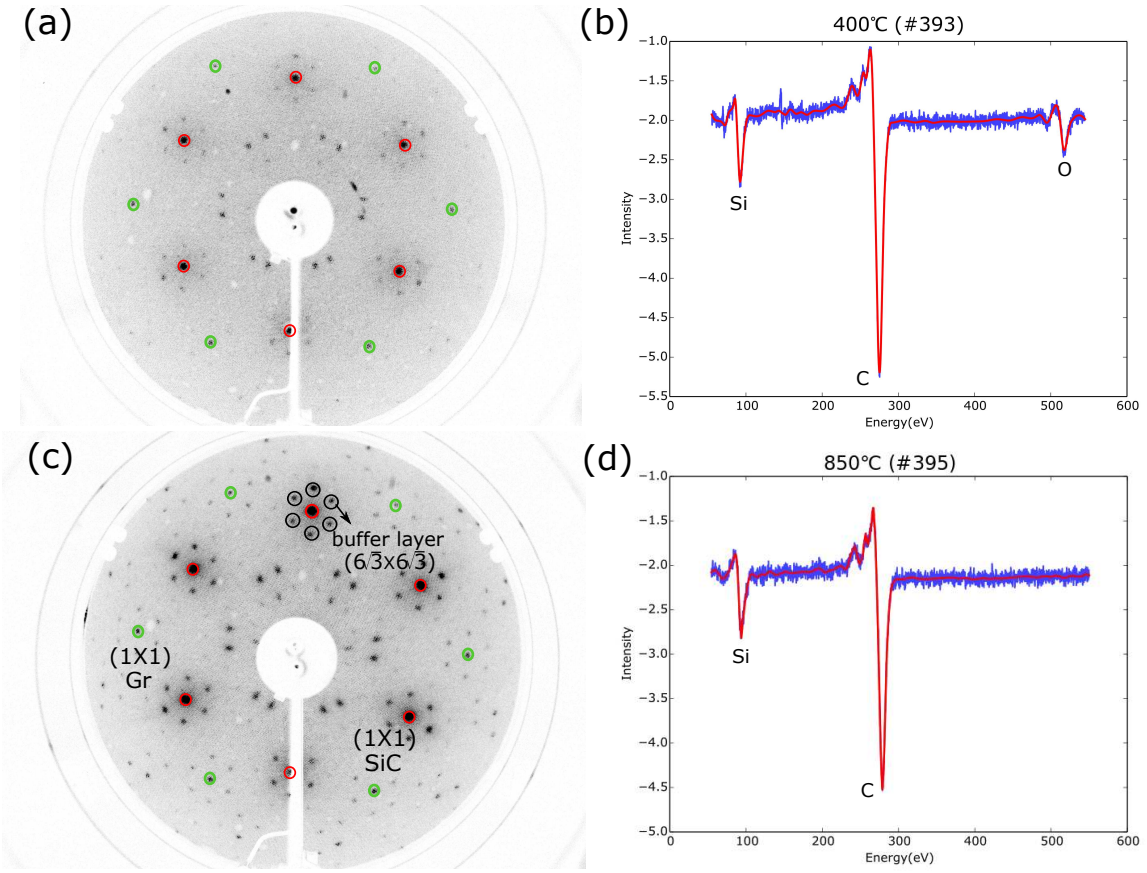

Figure 29: LEED and AES on sample HDS009 after annealing at 400°C in (a),(b) and 850°C in (c),(d). Both LEED images, taken at 106 eV, show SiC(1 × 1) rods with weak Graphene(1 × 1) rods rotated 60deg. SiC($6\sqrt{3} \times 6\sqrt{3}$)R30 pattern can be identified. AES shows clear silicon peaks at 92.5 eV and carbon peaks at 274 eV with shoulder peaks indicating graphene presence. The Si/C ratio is estimated to be (b) 0.257 and (c) 0.286. In addition, oxygen peak is also present in (c).

A typical LEED image taken on sample HDS009 are shown in Fig. 29(a) and (c). 1 × 1 first-order SiC rods (red circles) and $6\sqrt{3} \times 6\sqrt{3}$ reconstructions with weak yet clear 1 × 1 first-order graphene rods (green circles) can be easily identified, which is different from the normal much brighter 1 × 1 graphene rods on multilayer graphene samples and is

similar to the normal weak graphene patterns found on only buffer layer covered samples. Therefore the averaged graphene coverage on the surface should be between zero to one monolayer. Figure 29(b) and (d) are the AES spectra from sample HDS009 after annealing in vacuum, where the shoulder peak to the left of the primary carbon peak at 272 eV is typically attributed to graphitic carbon structures on the surface, in this case mostly buffer layer and monolayer graphene. Si/C ratios calculated from respective elemental peaks are 0.257 and 0.286. From the Auger attenuation model discussed in Chap. 2, graphene thickness is estimated to be equivalently between 0.75 and 0.9 monolayer, consistent with STM observations explained in the later sections. Both LEED and AES results support the sidewall graphene growth model that graphene forms much faster on the sidewall facet near an step edge than it does on the flat terraces resulting in fractional monolayer coverage on the surface.

Samples typically get much cleaner in terms of stable imaging and quiet tunneling current under STM after higher temperature annealing. Comparing 850°C annealing and 400°C annealing, LEED images show better contrast between the SiC/Graphene spots and the background, while AES results show higher Si/C ratios and an absence of Oxygen peaks as can be deduced from Fig. 29 (similar results are observed on other GNR samples as well). This serves as an indication that at around 850°C, oxides and other carbon-rich contaminations can be mostly eliminated from the sample. However, it is worth pointing out that the silicon peak position in the after-annealing AES measurement stays at 89 eV which is a signature of silicon oxide, hence suggesting that residual silicon-related oxide species are still present on the surface, despite of the lack of an obvious oxygen peak in the spectra. Nonetheless, a high temperature annealing is still a necessary step to prepare the sample surface in a fresh and clean, though not to the full extent, starting condition for STM measurements, which indeed has been confirmed by much more stable STM imaging shown in the subsequent sections.

Table 1: Selected List of Samples

Samples	HDS009	HDS002	25ed30	T79	EDJP1	EDJP2	4HNNA	4HPGNR
On-axis	Yes	Yes	Yes	No	Yes	Yes	Yes	Yes
Poly-type	6H	6H	6H	6h	4H	4H	4H	4H
Step Height (nm)	–	–	10 – 15	30	20	20	25	10
Step Direction	ZZ	ZZ	ZZ	ZZ	ZZ	ZZ	ZZ	ZZ
Step Formation	DSB	DSB	SB	SB	Litho	Litho	Litho	Litho

ZZ stands for zigzag; DSB stands for dimpled step-bunching; SB stands for step-bunching; Litho stands for lithography;

3.2 Sidewall Graphene along Zigzag Directions

3.2.1 SiC Sidewall Formation

In this thesis, we focus on the nanofacet and nanoribbon properties after GNR growth, and not refinement of the growth procedures. However, we briefly summarize our observations of the growth from the samples employed for these studies.

Figure 30 shows STM images of SiC sidewalls formed on the differently prepared samples after growth. At a large scale of several hundred nanometers, both on-axis (Fig. 30(a) and off-axis Fig. 30(b)) samples exhibit high order of step bunching leading to large steps of 15 to 40 nm in height. Clearly, T79, the off-axis sample, has a more regular spatial distribution of steps and they tend to be larger and more uniform in height (40 nm), which can be attributed to the much different stepflow velocities on the vicinal facets. Steps on HDS009, the dimpled surface, have more variabilities depending on the local miscut angle in the dimple. It is found that step bunching heights near the top of the dimple with larger miscut angles (4°) tend to be higher (15 to 30 nm) and more variable in directions after growth, while near the center of the dimple with smaller miscut angles, step heights are on the order of 10 nm and usually stay more ordered after the high temperature process. As for the patterned samples, pre-defined trench structures are largely preserved, though more details from ministep formation can be already seen from the large scale images in Fig. 30c. Upon zooming in, more fine structures around the sidewalls are revealed. Firstly, ministeps

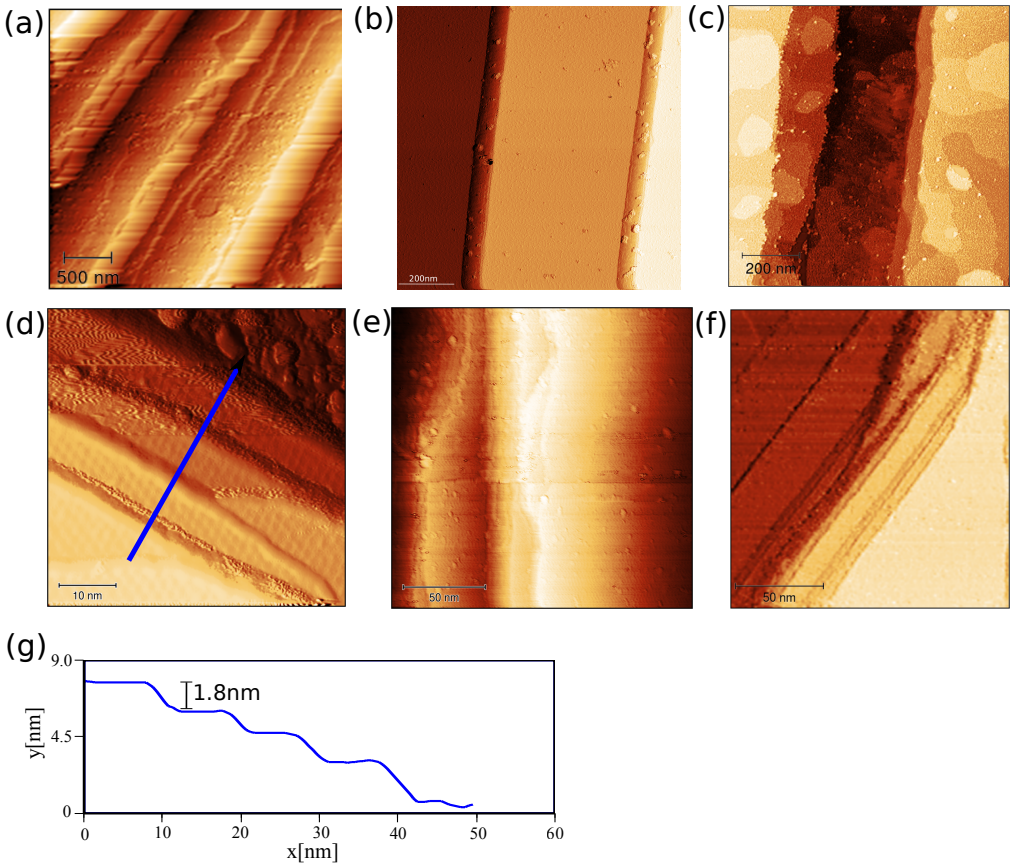

Figure 30: STM images of sidewall formation on different samples. (a) steps in the dimple on HDS009, typical heights are between 10 and 20 nm (4 V, 50 pA). (b) steps on T79, which are regularly spaced with terrace width around 1 μm and step height mostly at 40 nm (3 V, 40 pA). (c) steps on 4HNNA, predefined steps are faceted surrounded with small islands on the top and bottom terraces, the overall height of the faceted step is 15 nm (3 V, 50 pA). (d) tunneling conditions is (−3 V, 20 pA). (e) tunneling condition is (−4 V, 40 pA). (f) tunneling condition is (−2 V, 30 pA). d-f are corresponding zoom-in images of a-c.

formation are commonly observed on all sample surfaces shown in Fig. 30d-f (corresponding to Fig. 30a-c). The ministeps are on average 1 to 2 nm, or several Si-C bilayers, in height. On the self-organized samples, this can be explained as incomplete step bunching which introduces narrow merger regions between the microsteps resulting in multiple staircase-like sidewalls. On the patterned samples, it is possible that both incomplete step bunching and different stepflow velocities and surface energies between different SiC layers lead to step splitting that minimizes the overall surface energy. It is worth noting that ministeps are more common on the patterned samples whereas a large portion of the original steps are completely bunched together on self-organized samples. While this phenomenon is not yet

fully understood, one of the reason could be that step-bunching is a natural self-organizing process without much external intervention while lithography patterning introduces artificial starting points with more variability for step formation that are not stable and are energetically different between different SiC layers. Finally, slight differences in growth conditions and growth furnaces between samples could also lead to different growth results.

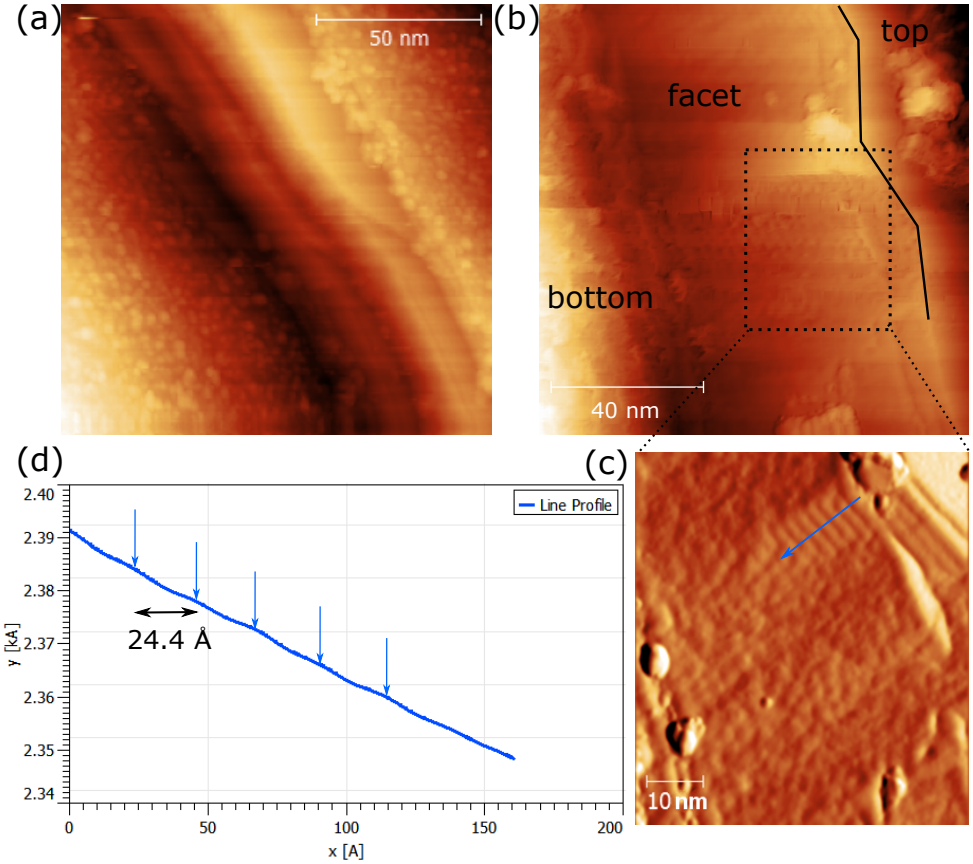

Figure 31: STM images comparing sidewall formation on self-organized (HDS009) and patterned (4HNNA) samples. (a) A typical step formed on HDS009, which is relatively straight despite the sample's macroscopic circular design (−4.5 V, 30 pA). (b) a representative step edge on 4HNNA, which exhibits wandering behavior that switches between zigzag and armchair directions with 30° from each other; the black line highlights the local step directions (1.5 V, 50 pA). (c) Zooming on the sidewall facet in Fig. 31 near the switching point; interesting period features can be seen and the on average 1 Å corrugations on the sidewall are also observed (2.0 V, 50 pA). (d) Line profile taken from the periodic features in Fig. 31d showing a 24.4 Å period that determines the local facet plane

Figure 31 demonstrates two typical step edges found on HDS009 and 4HNNA respectively. It clearly shows that on the dimpled surface (Fig. 31a), regardless of the curvature in the dimple, steps are relatively straight on 100 nm scale. This is also true for the other

two self-organized samples. However, on the samples where trenches are patterned along the zigzag direction (Fig. 31b and c), step edges tend to wander along the predefined direction switching to other directions. From the periodic features observed near the transition region, comparing to possible SiC sidewall facet models, it is found that the sidewall facet changes from being $(11\bar{2}\,16)$ to $(1\bar{1}0\,10)$(periodic features separated by 27.55 Å) which is along the armchair direction. This is likely due to the different facet energies between the two directions and the growth process favors a lower energy configuration. While such phenomenon does not occur on every step structure on the patterned surface, it has indeed been observed multiple times on the sample and could potentially be an important factor in determining the electronic structures of sidewall GNRs grown near such step edges. In fact, since different step termination implies different bonding geometry which can make the selective GNR growth direction-dependent, GNR formation on unstable step edges could exhibit a degraded transport characteristic because of the additional barriers from the wandering steps and altered vertical bonding to the underneath sidewall facets. It has also been recently reported that partial faceting of zigzag facets into armchair ones does happen frequently on lithography patterned step structures along zigzag directions and no electronic graphene is identified on the facet walls [69] which is consistent with our STM images, as well as STS results shown in later sections.

Finally, high resolution STM images in Fig. 32 taken around well-formed sidewalls on the samples reveal that the otherwise steep edges are indeed all relaxed into single low-energy nanofacets. Typical facet angles found on the on-axis samples are 22°, 25°, and 28°, corresponding to SiC $(11\bar{2}0\,16)$, $(11\bar{2}\,14)$, and $(11\bar{2}\,12)$ facets. The dimpled sample gives rise to sidewall facets of variable angles dependent on the location within the dimple. Nanofacets near the top of the dimple are usually shallower than those near the center of the dimple. Facet angles on the patterned samples are correlated to the initial height of the trench structure, for instance, the 25 nm high trench in Fig. 32c results in commonly measured facets of around 20° while a typical step on another patterned sample with 9 nm high trenches exhibits a 13° facet angle approximately. Another important observation on these single nanofacets is that regions close to them (both top and sidewall) are mostly

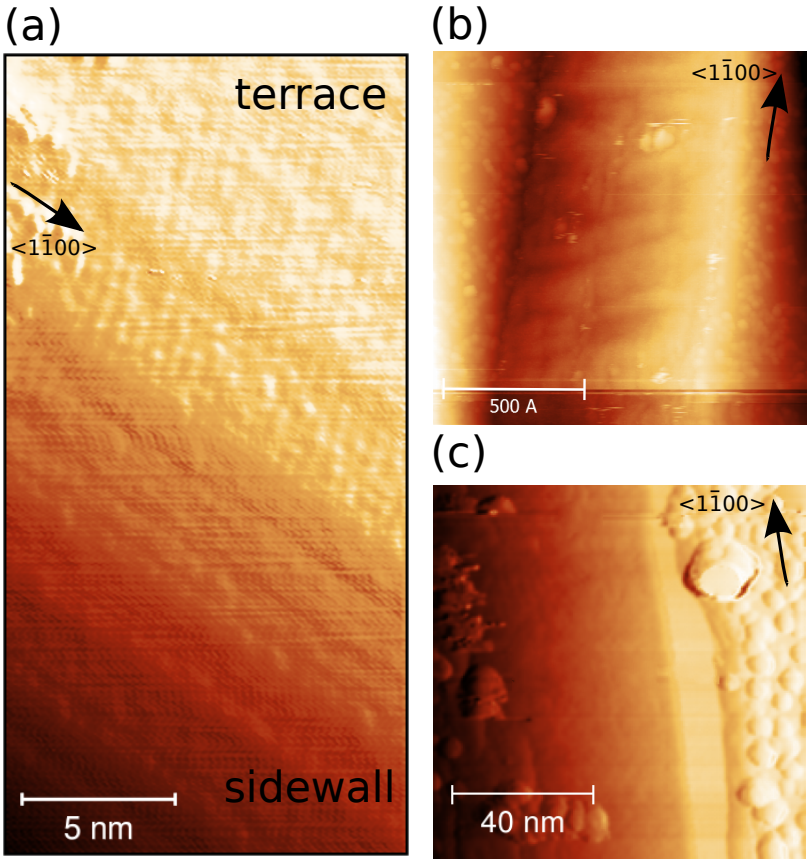

Figure 32: STM image showing topography of well-formed SiC sidewalls on different samples. (a) HDS009, step direction goes from the top left to the lower right of the images; periodic structures can already be identified, continuously covering the entire terrace and sidewall facet; atomic steps are completely bunched into the single uniform facet (0.8 V, 30 pA). (b) T79, a vertical step edge separating the facet and top flat terraces; sidewall facet has some long range corrugations but is generally much smoother than the particle-covered top and bottom of the terraces (−2.5 V, 30 pA). (c) 4HNNA, also showing a vertical step edge with the sidewall facet on the left. Near the step edge, both sidewall facet and top terrace are significantly smoother than the area around them (2.5 V, 50 pA)

significantly smoother than the flat terraces away from them and always stay free from contaminations. As discussed previously, these samples are essentially covered with buffer layer with graphene only forming near the step edges from the AES attenuation model and LEED image comparison, it hence indicates that the smoothness near the step edges are mainly because of graphene presence. Though not a direct evidence of graphene formation, the smooth features serve as a guide for finding sidewall GNR under STM.

3.2.2 Topographic and Atomic Imaging

An STM image taken near a typical step edge on HDS009 is shown in Fig. 33a and its inset. The step bends down along the diagonal direction of the image with a large step height around 15 nm clearly identified from the line profile (Fig. 33c) of the inset in Fig. 33a. As has been discussed before, although the surface away from the steps (on the flat terraces) is often times covered by large and rough features, the top corners of the steps always remain clean and smooth-looking as expected for a graphene or ordered buffer layer covered region. The unique underlying physics that is protecting these areas is going to be studied in the later sections.

With further zooming-in near the top edge of the step (Fig. 33a), graphene lattices can be readily seen, which extend continuously from the top terrace down to the sidewall. In the transition between the top terrace and the sidewall, the imaged lattice is distorted (on the order of 5%) and rotated (10°) even after thermal drift correction, in comparison to the much less deformed graphene lattice imaged on the top terrace away from this region, shown in the inset of Fig. 33b This is a combined consequence of lattice shearing and stretching from the local non-uniform strain. Effects of imaging distortion of the tilted surface can be excluded as well since it only introduces lattice stretching perpendicular to the step direction. Such strain is likely introduced by thermal mismatch (the expansion of graphene [214] and contraction of SiC substrate) [114, 174, 180] during the cooling phase of the growth process and also possibly caused by local defects (which could explain the rotation of the lattice), but more studies are needed to reveal the true origins of the local strain. In contrast, almost undistorted hexagonal lattices can be easily identified in regions away from the step edge as marked by the black hexagon in the inset of Fig. 33b. These results serve as a hint that, although graphene growth is continuous over the step, it would lead to both topographically and electronically different graphene near the step edge as compared to the top flat terrace. Combining the 22.3° facet angle deduced from the line profile (Fig. 33c) with the orientation of the hexagons near the edge, this step reveals itself as the $(11\bar{2}\,16)$ facet with a zigzag edge termination.

More evidence of the presence of graphene is provided in Fig. 33d and Fig. 33e, where

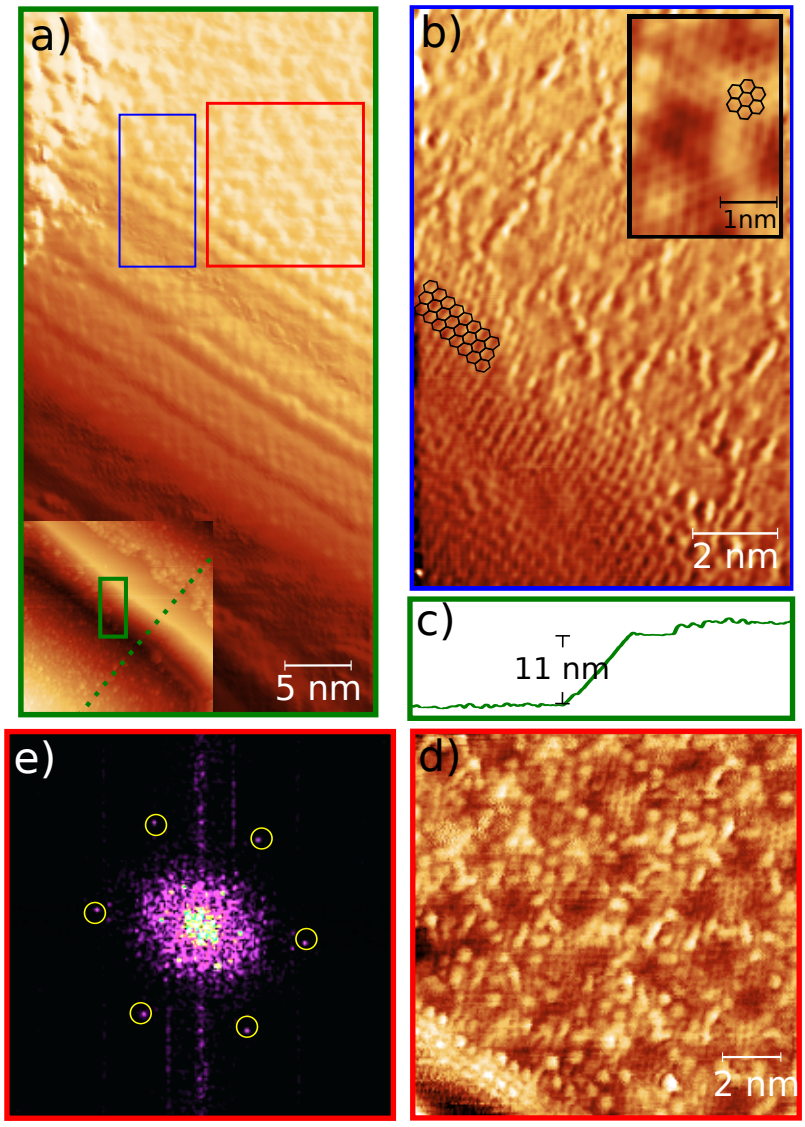

Figure 33: STM image showing topography of a typical sidewall facet on HDS009. (a) an STM image showing the overall step structure from a large step bunch shown in the inset, facet estimated to be $(11\bar{2}\,16)$. (b) On the top terrace of a, near the step edge with both distorted (to the left) and undistorted (inset) graphene lattice present. Graphene lattices near the step edge are stretched and sheared compared to the lattices on the flat terrace farther away from the step edge (inset), with an additional 10° rotation. The two images are not on the same scale. (c) Line profile taken along the dashed green line in the inset of a. (d) top terrace of b, showing the undistorted graphene lattice in this flat region. (e) FFT of d showing the the $(1 \times 1)_{Gr}$ periods (2.34 Å on average). Images are acquired at sample biases (a) −0.6 V, (b) −1.0 V, (e) −0.6 V with tunneling current set at 30 pA.

hexagonal graphene on top of the quasi 6×6 superlattice is clearly imaged, as well as underlying bright protrusions with triangular symmetry resulting from the electron density redistribution between the buffer layer and SiC substrate [84]. Figure 33e, the FFT of Fig. 33d, more clearly shows the graphene 1×1 (2.34 Å on average) periods. Right along the step edge, bright modulated LDOS features are also observed, whose parallel period is 5 Å and perpendicular period is 3.7 Å. Although the origin of this pattern is not yet clear, it is not likely to be the commonly observed ($\sqrt{3} \times \sqrt{3}$R30°) scattering patterns as it is known that zigzag-terminated graphene prohibits such scatterings [154, 171, 200].

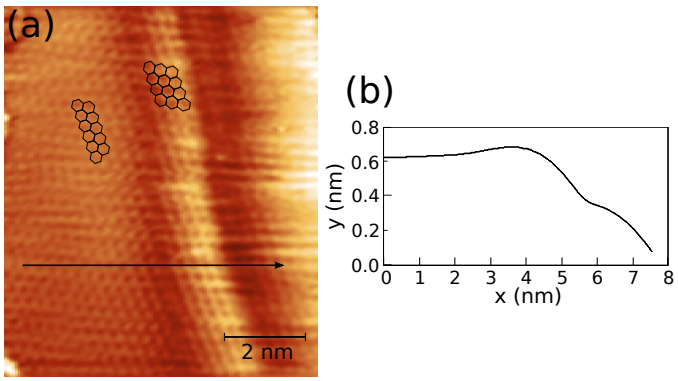

Figure 34: STM image showing topography of a step edge on 25ed30. (a) topography of the step edge lying vertically, a bulge-up structure on the step edge can be seen. (b) horizontal line profile of a.

With more graphitization near the step (25ed30), it is more clear that graphene continuously grows over the edge as shown in Fig. 34 and also in Fig. 38a, which shows a bulge-up (60 pm) near the step edge, lying vertically in the image (total step height 18 nm). Such bulge-up is also found in Fig. 33a and very common near other step bends on both samples. We believe the origin of this feature is the thermal stress from the cooling down after growth, where the SiC substrate contracts while graphene expands. As graphene is more bonded to the substrate on the flat top terrace [201] than on the sidewall facets, it will have to bulge up at the transition region. Similar to Fig. 33b, graphene lattices near the bending regions also appear to be distorted compared to the flat terrace, due to the topographical curvature and the aforementioned thermal stress introducing significant strain in itself. Again the step direction is along the zig-zag direction with respect to the graphene lattice.

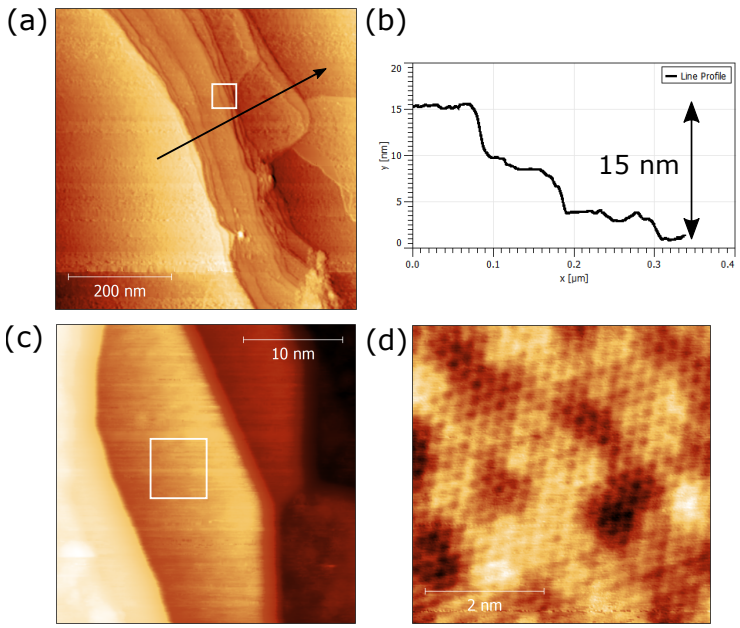

Figure 35: STM image showing step structures on EDJP1 at different scales. (a) Patterned step structure split into multiple ministeps but with smooth-looking flat plateau. (b) A line profile taken along highlighted path in a shows the overall step is 15 nm in height. (c) Zooming onto a small ministep in a which shows weak 6×6 pattern on the narrow terrace. (d) Atomic scale graphene lattice acquired from c with 6×6 corrugation in the background; lattice constant is measured to be 2.48 Å without obvious distortion or strain; tunneling condition is set at 1.5V and 0.5nA.

On the patterned sample EDJP1, shown in Fig. 35, atomic graphene is also resolved near the faceted trench sidewalls. However, it is mostly found on the split narrow ministeps (Fig. 35a) or on the plateau near the top of the trench sidewalls, where the quasi 6×6 reconstruction can be easily seen. Since the ministeps are typically 1 to 2 nm different in height from one to the next, it implies that graphene lattices are most likely extending continuously between them [82], covering the entire sidewall facets. In contrast to the lattice distortion found on HDS009 and 25ed30, such phenomena has not been observed on EDJP1 so far. It is possible that due to the step splitting, graphene lattice experiences a more balanced force on the flat regions and thus can better relax on and between the ministeps resulting in much less strain between the carbon atoms.

It is worth noting that, from Fig. 32, Fig. 33b, Fig. 37, along with other STM images over the sidewall facets, graphene, or at least the smooth-looking material layer, typically

covers the entire sidewall and part of the top flat terrace near the step edge, but terminates right at the bottom of the facet walls. Such overgrowth is observed on all samples meaning that the top terrace is kinetically and/or energetically favored in the selective graphitization. As graphene formed in this particular part of the top terrace is on one side connected to the buffer layer while sidewall graphene on the other, such transitional graphene could be structurally different than normal pristine graphene, and potentially exhibit interesting characteristics. For discussions about sidewall GNRs, contributions from such regions should not be neglected

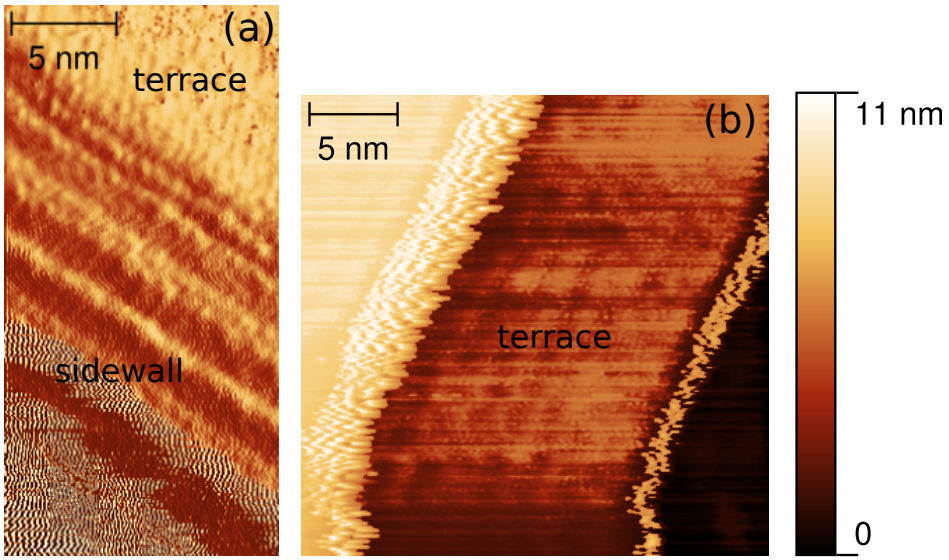

Figure 36: Imaging instability on sidewall facets on HDS009. (a) STM imaging becomes more and more unstable as the tip moves onto the nanofacet while rest of the image exhibits atomic scale details (1.5 V, 30 pA). (b) two steps of roughly 5 nm in height both show instability near the step edges (−2.5 V, 25 pA).

Apart from atomic scale imaging near the step edges, STM tips have frequently experienced imaging instabilities on large facet walls as shown in Fig. 36. While the rest of the images shows decent quality with some of them even achieving atomic details, tunneling current becomes highly unstable when imaging is taking place right in the middle of the sidewalls but fully recovers after the tip leaves those areas. The fact that imaging appears stable and the STM tip doesn't show irregular characteristics after exiting the sidewall

facets suggests that the interaction between surface and tip is mostly mechanical through mechanisms like resonance or vibration [98, 157]. Based on the observation that graphene is present near the step edge and grows seamlessly onto the sidewalls, it is possible that upon extending further down onto large sidewall facets away from the step edge, graphene lattice becomes differently interacting with the underlying SiC nanofacet and therefore turn into a form that is able to easily deflect to external perturbations [86, 100, 157] including electric fields in the case of STM. As a reference, a suspended-graphene resonator about 100 nm in length, in the limit of zero tension, has a resonance frequency on the order of MHz [98] . While a clamped nanomembrane with area size of 10 nm has a basic resonance frequency on the order of GHz. In the case of sidewall graphene, the different structural geometry, stronger interaction with the substrate, and sharp edge terminations can lead to a much lower resonance frequency.

For the other samples (T79, 4HNNA, and other patterned ones), atomic scale graphene lattices were not directly resolved under STM imaging, but their general characteristics are similar to samples HDS009 and 25ed30 (note that the resolution of STM depends on the particular tip in use). Figure 37b and e illustrate structures of two step edges formed on 4HNNA and T79 respectively. Notably smooth regions are found on the top terraces in Fig. 37c and f, where the SiC(6×6) periods are clearly imaged. The sidewall facets also exhibit smoothness of a magnitude higher than the other flat terraces and appear to be continuously connected at the bending edges with the SiC(6×6) periods aforementioned, although no clear atomic structure can be identified. Furthermore, transport measurements (not shown) on the off-axis sample T79 manifest ultra low resistance only along the sidewalls acting as a significant conductive channel, signature of graphene presence on the otherwise insulating SiC substrate [120]. All these facts indicate that graphene may be actually present near the step edges. The reason of graphene lattice being not readily observed could be that such graphene is electronically different from what has been observed on the samples discussed above and thus making it difficult for distinguishing their LDOS from the underlying SiC surface in STM. In fact, Fig. 37a and d show the topography right on the sidewall on 4HNNA and T79, whose long-range corrugation resembles a bare SiC surface,

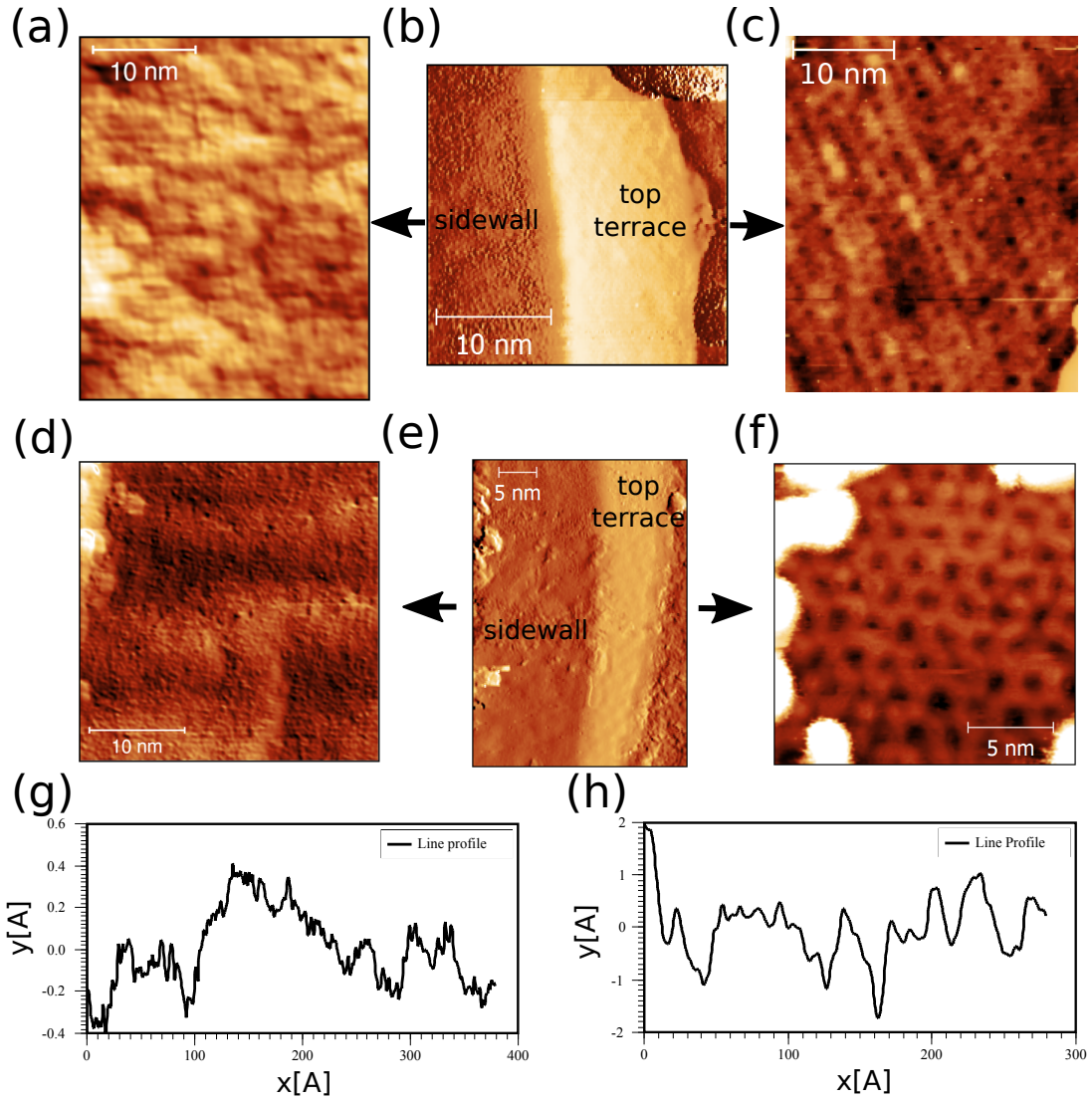

Figure 37: STM images on the sidewall facet and top terrace near the step edge on 4HNNA (a–c) and T79 (d–f). (a) imaging on the sidewall facet in b shows fine structures residing on surface corrugations as the background (2.0 V, 50 pA). (b) Across the step edge on 4HNNA, both sidewall and top terrace are smooth-looking, free from the dense disordered particles seen on other flat regions and seemingly connected continuously (2.5 V, 50 pA). (c) Zooming onto the top terrace reveals SiC(6×6) patterns (2.0 V, 50 pA). (d) imaging on the sidewall facet in e (−1.2 V, 40 pA). (e) Across the step edge on T79 (2.0 V, 40 pA). (f) Top terrace imaging in e (−2.0 V, 30 pA). (g) height profile of the sidewall facet in a with RMS roughness 0.3 Å. (h) height profile of the sidewall facet in d with RMS roughness 1.1 Å.

but with weak fine structures that may be attributed to other origins. RMS roughness on the sidewall (≤1 Å) is also found to be smaller than that from the bare SiC substrate used for this sample (≥2 Å), indicating a possible additional layer over the facet. This conjecture

is further supported by analysis of STS measurements taken in such regions, as will be discussed later.

3.2.3 Electronic Characteristics of Sidewall Graphene

The electronic structures of graphene grown over the step edges is characterized by STS measurements taken both at individual locations and as maps over the scanning area while imaging. Figure 38c shows STS spectra taken at marked spots in Fig. 38a near the bulge on 25ed30, all of which reveal series of discrete LDOS peaks. dI/dV spectra were obtained as the digital derivative of the acquired $I(V)$, using a smoothing width of 0.0625 V. The spectral shapes at positive sample bias, when scaled up and mirrored around zero sample bias axis (black curves), coincide strikingly well with those on the negative bias side. This electron-hole symmetry is a strong indication that the observed features derive from graphene near charge neutrality, and not from SiC electronic states. Note that small voltage shifts to the black curves are included in order to fully align spectral features of the graphene band structure. The amount of shift is determined by maximizing the normalized cross-correlation coefficients that matches the peak positions between the negative and positive side of the spectra manifesting the electron-hole symmetry. Physically, the shifts correspond to the Dirac point energy with respect to the Fermi level (zero sample bias) in each spectra which all turn out to be positive and smaller than 50 mV indicating slight p-doping of graphene near the step edges, in agreement with recent transport and ARPES measurements [11] (although the ARPES was done on armchair-oriented sidewalls). The asymmetry of the intensities of the peaks on the two sides can be attributed to the non-equivalence of the tunneling matrix in STM at positive and negative biases which depends on the specific tip.

In order to interpret these energy states, we start by indexing them from low to high biases with increasing integers $\pm N$. It is found then that the peak energies linearly scale up with the square root of the absolute integer index values. The least square fitting results are shown in Fig. 40b and they clearly confirm the $\sqrt{|N|}$ dependence of the peak positions. Moreover, averaged STS measurement along different regions of interest near a second step

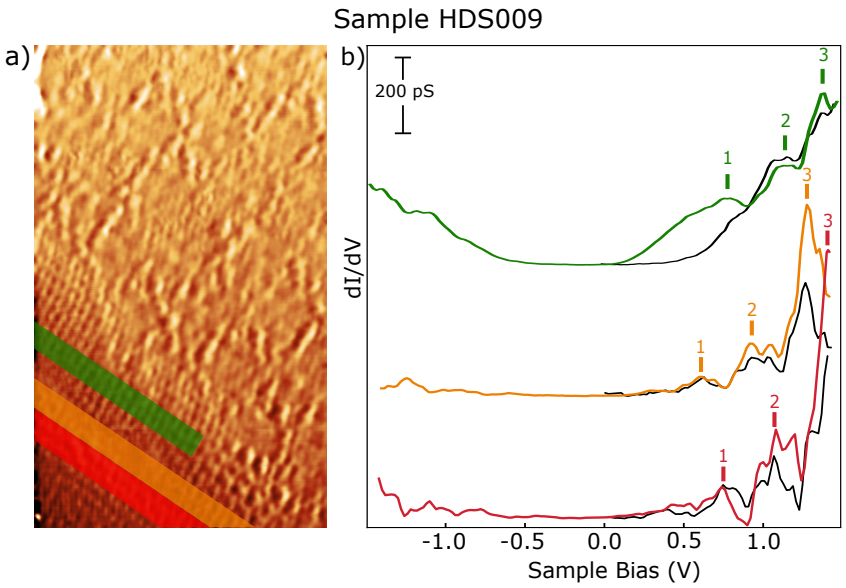

Figure 38: (a) STM image of a step edge on HDS009, showing the continuous graphene growth over the step, graphene lattices are distorted at the bending edge (−0.6 V, 30 pA). (b) Averaged STS measurement along different regions of interest indicated in a) (the same area in Fig. 33a). The black curves are the scaled mirror of the negative bias side in each spectra.

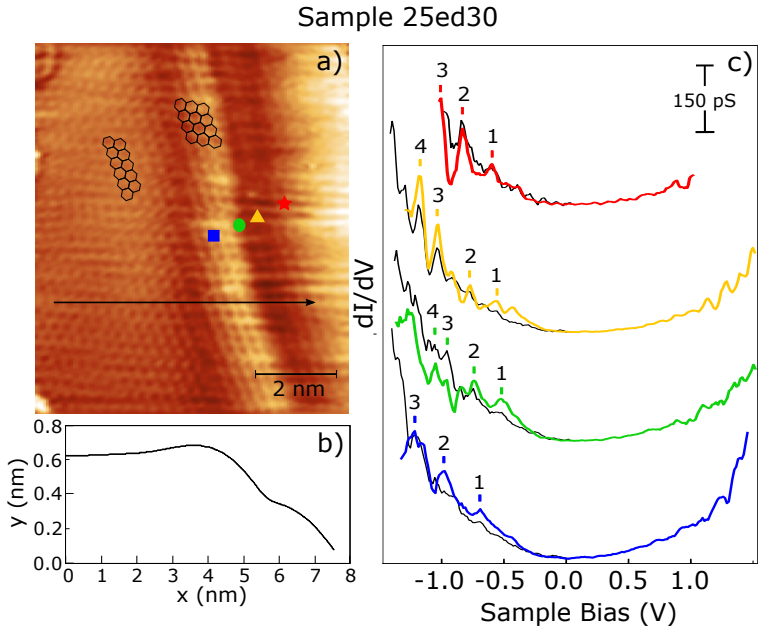

Figure 39: STM image of an over-graphitized step edge on 25ed30 and STS measurements. (a) Atomic graphene lattice, acquired at sample bias of 1.0 V with tunneling current 30 pA (total step height is 18 nm, along the zigzag direction of graphene). b) Line profile showing the curvature near the step. c) Point STS measurement at locations marked in a) near the step bulge with peak indices labeled by the dashed lines. The black curves are the scaled mirror of the negative bias side in each spectra.

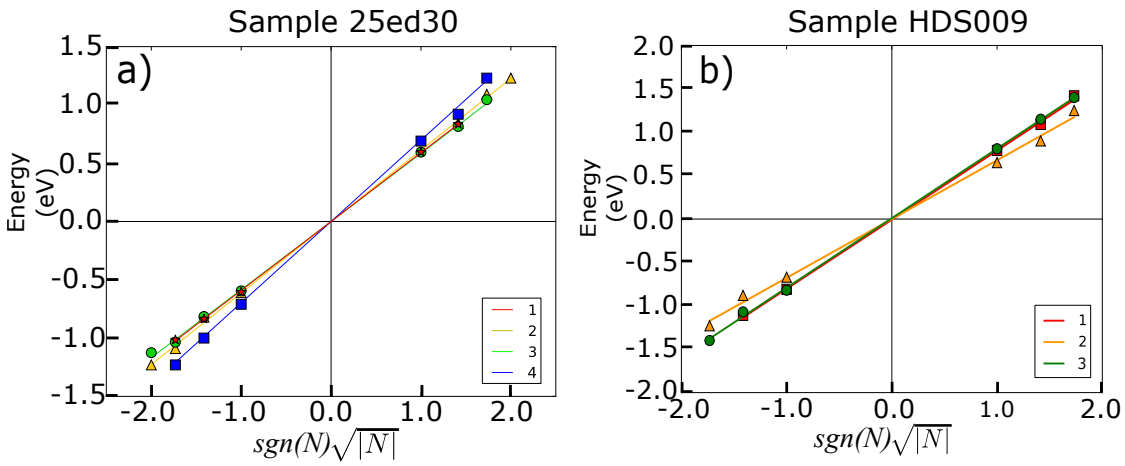

Figure 40: (a) Linear fit results of peak energies with the square root of their indices from the spectra in Fig. 38b. (b) shows the similar linear trend found in averaged STS spectra in Fig. 39c.

edge on HDS009, indicated in the lower left inset in Fig. 38a, also exhibits similar LDOS peaks and the least square fit results of peak energies over square root follows the same linear trend.

The $\sqrt{|N|}$ scaling of localized electronic states are commonly observed in Landau Levels in monolayer graphene under perpendicular magnetic fields as $E_N = \lambda\sqrt{2e\hbar v_F^2 B|N|}$ with $\lambda = \pm 1$ representing the electron and hole states [121, 139] . However, it is theoretically predicted [23] as well as experimentally observed [21, 25] that non-uniform strain in graphene produces pseudo–Landau levels (pLLs) in the absence of magnetic field, with the same mathematical formulation except that B is replaced by the pseudo magnetic field B_p, as discussed in Chap. 1. Therefore, after comparing the $\sqrt{|N|}$ scaling in our STS data with the theoretical pLL model, the observed discrete energy states are indeed the pLLs resulting from significant strain in the sidewall graphene near the top corner with the estimated pseudo magnetic fields of, respectively, 266 T, 286 T, 260 T for the first three spectral locations in Fig. 39a, and 371 T at the location marked blue, assuming $v_F \sim 1 \times 10^6$ m/s. These effective magnetic fields, on the order of 200–300 T, correspond to a significant amount of strain in the graphene near the step edge which well explains why the associated graphene lattice appears to be distorted in Fig. 33a. However, it has to be noted that it is the spatial gradient of the strain that plays the key role giving rise to pseudo magnetic fields, the

mathematical details of which can be found in Chap. 1. Since the first three locations are spatially close, it is not surprising to find the pseudo magnetic fields and consequently the strain roughly the same with each other. However, the fact that the blue region exhibits much higher pseudo magnetic field implies the bending region where the step just starts to curve down onto the sidewall carries the largest strain and hence graphene grown over there should have the most altered electronic structures. In contrast, the estimated pseudo magnetic fields in Fig. 38a are 483 T, 349 T and 489 T from averaging area G to E. Compared to the the previous results, these values are much larger indicating a larger strain variations within this area, which is consistent with the much more distorted graphene lattice near the step edge in Fig. 33a.

The pseudo magnetic field can also be estimated by evaluating the apparent displacement in atomic positions from the STM images. Figure 41b plots the displacement field (deformed and undeformed lattice sites), from which the $\mathbf{u}(\mathbf{r})$ can be calculated and interpolated over the 2D area. The undeformed lattice constant is chosen as the spacing between centers of hexagons imaged on the top terrace to the far left where the hexagons is by large undeformed, therefore the displacement field is only showing the relative change in graphene lattice between the transition region and the flat top terrace. Using Eq. 43, the averaged pseudo magnetic field is on the order of 500 T, in good agreement with the results extracted from the STS spectrum. More accurate calculation would need to account for the discreteness of the lattice sites and actual local bonding environment that affects the hopping amplitude and its dependence on the bond length.

A significant result of this work is the discovery that strain in the vicinity of the nanofacet transition is not only due to curvature of the graphene. In fact, the strain appears to be predominantly bond stretching and shear which apparently results from thermal distortions during growth, and a change in the epitaxial constraint from the top terrace to the nanofacet. In order to better understand the origin and the potential implications of the observed strain effects, experimental results are compared to Molecular Dynamics simulations constructed to broadly mimic the experimental system, but with a focus on strain effects. Simulations were performed by S. Zhu and Prof. Teng Li in the Mechanical Engineering department

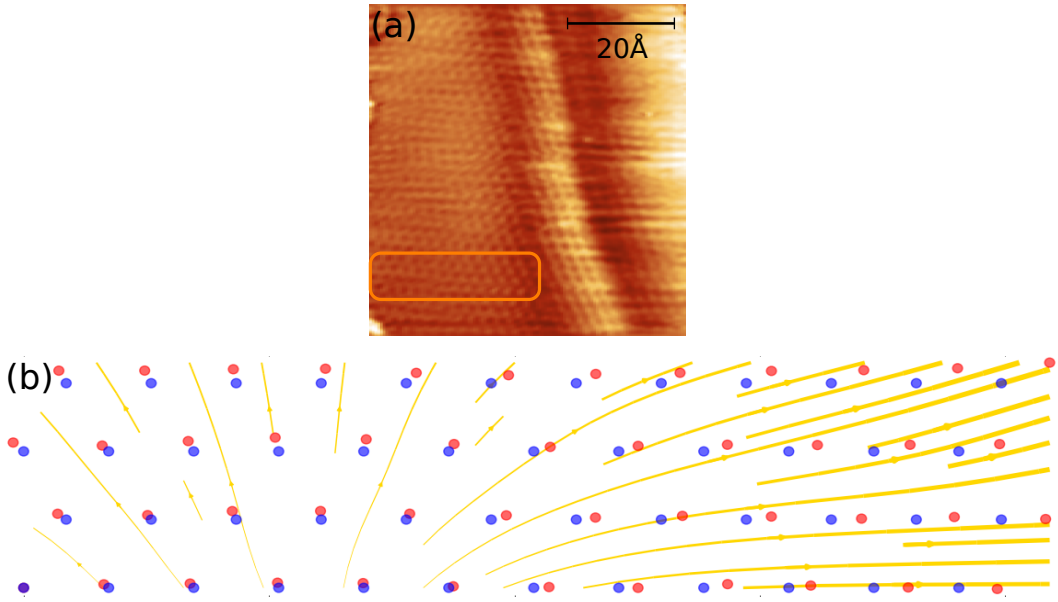

Figure 41: Estimate of pseudo magnetic field from topography. (a) atomic STM image near the step edge, the same area where the STS is taken in Fig. 39. (b) deformed (red) and undeformed (blue) lattice sites measured from a, along with the interpolated displacement field $\mathbf{u}(\mathbf{r})$, which shows the relative change in graphene lattice between the transition region and the flat top terrace. The yellow lines denote the apparent displacement field $\mathbf{u}(\mathbf{r})$ with the line thickness representing the magnitude of apparent distortion, ranging from 0.7% to 9.5% approximately.

at the University of Maryland (see, e.g., Refs. [219, 221]). The model setup is shown in Fig. 42a, where graphene bends over a rigid substrate. The substrate is modeled by a layer of graphene with zero degree of freedom for its atoms. Periodic boundary conditions are imposed in x direction. A sharp bending with an assigned angle is imposed at $y = 0$. The second-generation reactive empirical bond order potential [195] is adopted to describe the carbon-carbon covalent interaction in graphene. The initial flat configuration of graphene has a width of 20 nm along the y direction. Each carbon atom in the graphene interacts with substrate atoms via the Lennard-Jones potential $V_{gs}(r) = 4\varepsilon_{gs}(\frac{\sigma_{gs}^{12}}{r^{12}} - \frac{\sigma_{gs}^{6}}{r^{6}})$, where $\varepsilon_{gs} =$ 0.00284 eV, $\sigma_{gs} = 0.34$ nm, corresponding to a typical interlayer interaction in graphitic systems. The graphene initially evolves freely to accommodate the bending feature while trying to conform onto the entire substrate. The simulation is carried out using large-scale atomic/molecular massively parallel simulator (LAMMPS)[173] with canonical ensemble at a temperature of 5 K and a time step of 0.0005 picosecond. After the graphene has

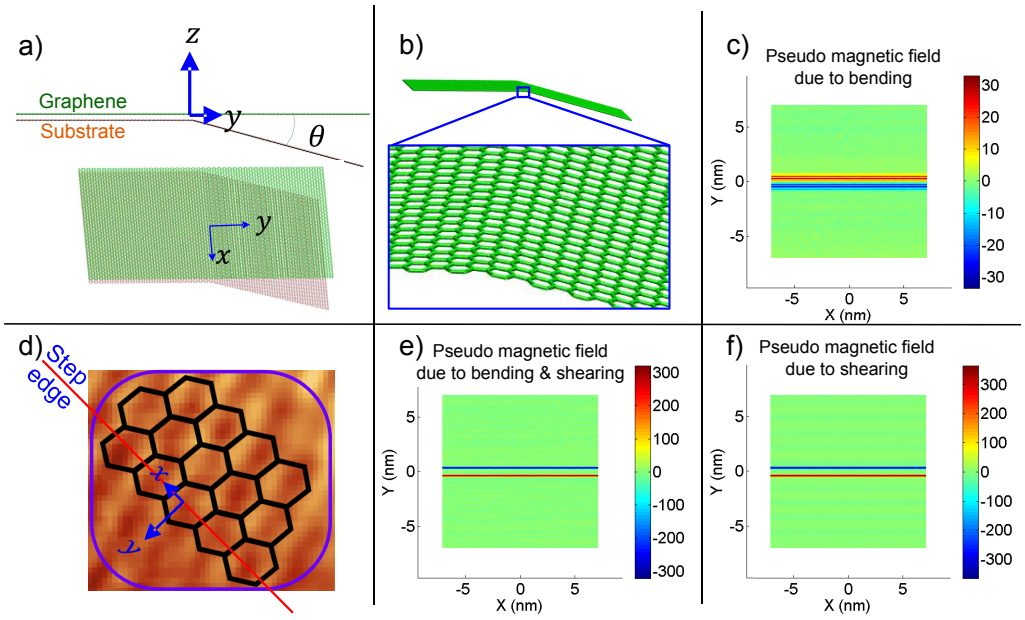

Figure 42: Molecular dynamics simulation results. a) initial model consists of a 20×20 nm rigid substrate including a 10 nm flat terrace on the left and a 10 nm facet at an angle θ on the right, and another 2020 nm graphene on top of the substrate. Periodical boundary condition is imposed along x direction. b) morphology of graphene conformed to the SiC substrate after energy minimization. The substrate is not shown for visual clarity. c) pseudo magnetic field in graphene due to bending at the step edge. Here $\theta = 45°$ d) STM image suggests a shearing deformation in graphene lattice at the step edge, as illustrated by the overlaid lattice. e) pseudo magnetic field in graphene due to bending and shearing at the step edge. Here $\theta = 45°$. f) pseudo magnetic field in graphene due to shearing at the step edge. Here $\theta = 0°$

maintained a stable conforming morphology over the bending feature, the energy of the system is first minimized using the conjugate gradient algorithm until either the total energy change between successive iterations divided by the energy magnitude is less than or equal to 10^{-20} or the total force is less than 10^{-10} eV/Å. Fig. 42b shows the energy-minimized morphology of graphene on the bending feature. Given such deformation from simulation, the Lagrange strain tensor is used to calculate the resulting pseudomagnetic field. Fig. 42c shows that for a conformable bending deformation, the resulting pseudo magnetic field in the graphene assumes a two-line distribution, consistent with other reports in literature [161]. For a bending angle of 45° (even larger than the experimental setup), the field intensity reaches 20 T. The field intensity decreases as the bending angle diminishes. Therefore it is evident that the bending deformation alone is not sufficient to account for the measured

high intensity pseudo magnetic field in the experiments. As shown in Fig. 42d, a closer view of the deformed lattice of graphene in the STM image offers evidence of significant shear deformation in the vicinity of the bending edge, with some bonds also stretched. In fact, the shearing effect is readily visible from the lattice distortion in Fig. 33, where a sheared hexagonal lattice frame is overlaid on top for better visualization. To clarify the effect of such shearing deformation on the resulting pseudo magnetic field, we impose a shearing deformation to the graphene along the step edge by shifting the position of all carbon atoms on the step along 45° direction by 0.1 Å, which introduces a narrow shearing band in the graphene at the step edge, similar to the overlaid lattice in Fig. 42d. Fig. 42e plots the pseudo magnetic field in the graphene resulting from both bending and shearing deformation at the step edge. The peak values of such a pseudo magnetic field is as high as 300 T, comparable to the experimental results. These results suggest that the highly localized shearing deformation near the step edge plays a dominant role for the significant pseudo magnetic field in our epitaxially grown graphene nanoribbons. This argument is supported by further simulations of a flat graphene nanoribbon only subject to a similar localized shearing band deformation (e.g., no bending, Fig. 42f), which yields a pseudo magnetic field of similar intensity as in Fig. 42e.

Strain effect is only one of the factors that are present in the sidewall graphene system on SiC, modifying its electronic structures. Figure 43a shows an STM image from HDS009, containing two steps of 20 nm and 40 nm in width, 5 nm and 8 nm in height respectively, of which imaging on the sidewall and the top terraces near the bending edges is much smoother than the buffer layer next to them. STS measurement further confirms the presence of graphene by showing the linear dispersion at low sample biases. Averaged STS in Fig. 43c along the step near the wide step (40 nm) edge shows the evolution of the Dirac point energy with respect to the spatial position. The Dirac point minimum on the negative sample bias side gradually moves from −0.6 V to −0.5 V as the averaging area moves from the flat top terrace towards the step edge. However, a dramatic change from −0.5 V to approximately zero is observed as the averaging goes across the step edge. The evolution of the Dirac point indicates a significant shift in the doping levels of the graphene layer on

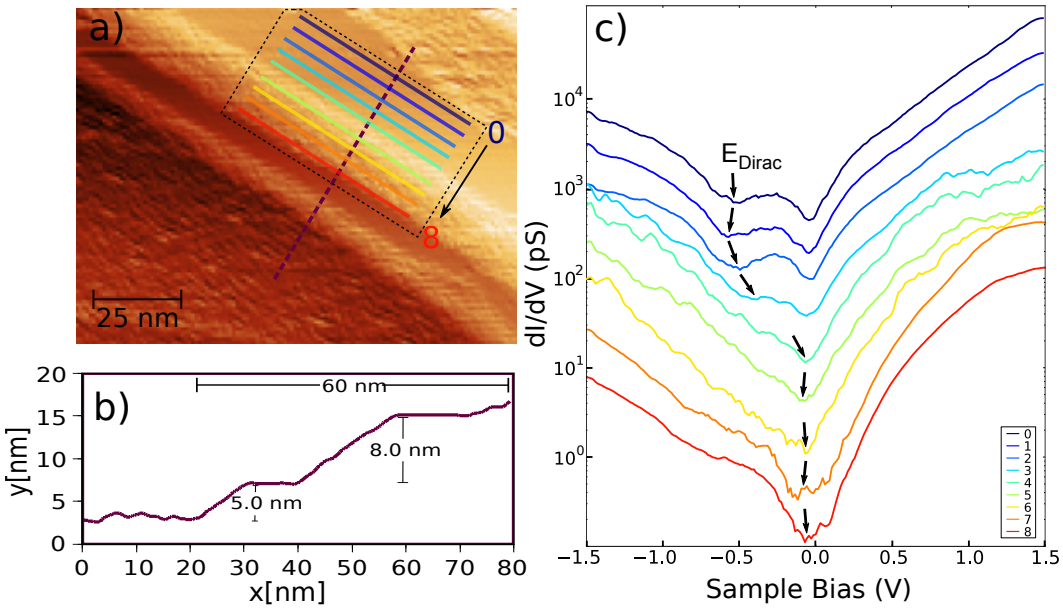

Figure 43: (a) STM image showing two steps. The narrow step is 20 nm wide and 5 nm high; the wide step is 40 nm wide and 8 nm high (sample bias −2.0 V, tunneling current 30 pA). (b) Line profile taken along the dashed purple line in a showing the step structure. (c) Averaged STS along the 40-nm step (log scale). Colors correspond to the averaging regions marked in a. The averaging areas are taken as rectangles adjacent to each other with an averaging width of 3 image pixels, corresponding to approximately 30 Å. Arrows indicate the Dirac point as the spectra cross over the top corner of the nanofacet. An abrupt 0.45V shift in is observed between spectra near the corner and those below it.

the wide step which appears to be highly n-doped far away from the step edge and nearly undoped across the step edge. Although this doping change takes place over the whole step region, the dominant change arises right near the edge, and hence implies unique physics present in this transition region. The origin of the doping change is not yet known, but it could have at least three contributions: 1) The graphene transitions from SiC-bound on the flat terrace to unbound (or at least differently-bound) over the sidewall facet leading to a varying potential from the interaction between graphene and the SiC substrate; 2) the effective vector potential due to non-uniform local strain could introduce a scalar potential [4, 23]; 3) local defects that may be present near the step edge (such as the bright features in Fig. 38a and the kink in the step direction in Fig. 39a) may also contribute to the doping levels. From the abrupt change in doping levels, an in-plane electric field across the 40-Å region can be estimated, which is on the order of 0.01 V/Å. The value should be regarded

as a lower limit of the actual effective electric field because the averaging length is limited by the spatial resolution of the data (10 Å). Such field could potentially lead to Rashba-type spin polarization in the local region if an enhanced spin-orbit coupling either from the substrate or the edge passivation is present [110].

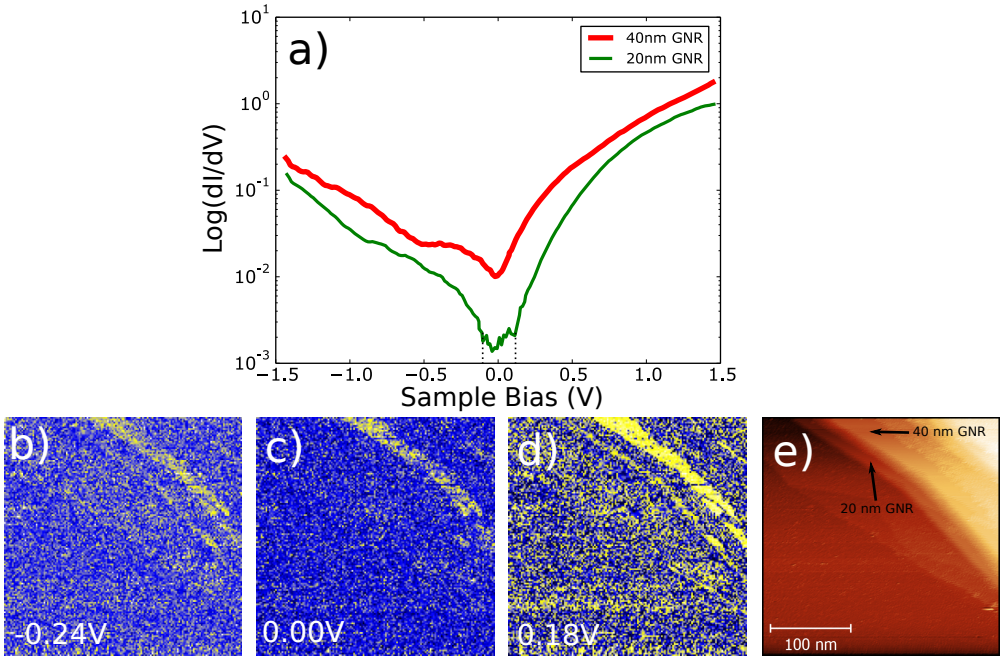

Figure 44: (a) Averages STS spectra over two steps shown in Fig. 43a, data are displayed in log base; STS on the 20 nm GNR (green line) shows almost three orders of magnitudes lower LDOS around 0.0 eV compared to the average on the 40 nm GNR drawn in red line. STS mapping at different energies better illustrated the difference in LDOS on the two ribbons, (b) -0.24 eV, (c) 0.00 eV, (d) 0.18 eV. (e) topography image taken simultaneously with the spectroscopy

Additionally, averaged STS spectra along the (0001 terraces are plotted in Fig. 44a (log scale). The thin green curve is the average of all STS measurements on the narrow terrace (20 nm), which shows conductance gap between -0.1 V and 0.1 V. The thick red dashed curve is the averaged STS over the wide terrace (40 nm), which shows the typical linear dispersion around zero sample bias. The dip around -0.6 V is understood to be the Dirac point, which is shifted with respect to the Fermi energy due to the strong electron transfer from SiC to graphene [84]. The distinct LDOS behavior in these two ribbons demonstrate that the narrow graphene nanoribbon (20 nm) shows significant confinement effects due to

its small size as compared to the 20 nm-wide graphene nanoribbon since the two ribbons appear to be identical under topographic imaging, except for their widths. Furthermore, the conductance gap is throughout the entire 20 nm-wide ribbon regardless of the slight change in its orientation from the lower right to the top left. Quantum confinement in a local area of graphene is known to be able to greatly alter the material's band structure [67] . The effect, in its simplest version, can be expressed as $E = \hbar v_F \pi \sqrt{(n/W)^2 + (m/L)^2}$ [30] , where W and L denote the width and length of the graphene area with n and m the quantum numbers. In the case of graphene nanoribbons, L approaches infinity leading the formula further simplified as $E = \hbar v_F \pi n/W$. Substitution of $v_F \sim 1 \times 10^6$ m/s and $W \sim 20$ nm results in the spacing of the quantized energy levels being on the order of 0.1 eV, which well agrees with the 0.2 eV bandgap feature observed in our data.

For T79 and 4HNNA, where the graphene lattice is not directly imaged, STS provides an alternative to probe the electronic properties of those regions as well. On 4HNNA, Fig. 45b shows averaged STS spectra from the nanofacet shown in Fig. 45a. The asymmetry in the conductance intensity from the negative bias side to the positive bias side can be attributed to the inequivalence in tunneling matrix between the electron and hole and also partly to the band bending caused by stronger electric field near the STM tip. It can be seen that from -0.2 eV to 0.2 eV, there is a gap in the differential conductance. Figure 46 shows STS spectra taken at different locations across a 30 nm step on T79. It is readily seen that at the bottom and top of the step, STS spectra resembles measurements from plain monolayer graphene on SiC [82, 187] indicating graphene formed at those locations are close to that formed on a flat SiC substrate. However, spectra in the center of the nanofacet reveals significantly lower LDOS between -0.7 V and 0.7 V in sample bias, even when the scanning probe is pushed in up to 0.5 Å towards the surface. The actual bandgap appears to extend from about -0.3 V to 0.2 V. As the STM tip approaches the step edge, distinct kinks in the spectra can be identified which can be attributed to localized electronic states in the system. Finally, spectra on top of the step edge show very similar characteristics of monolayer graphene which again illustrates graphene in this region is void of intervention from effects near the step edge. Such transitions in electronic states across the sidewall facets indeed suggests

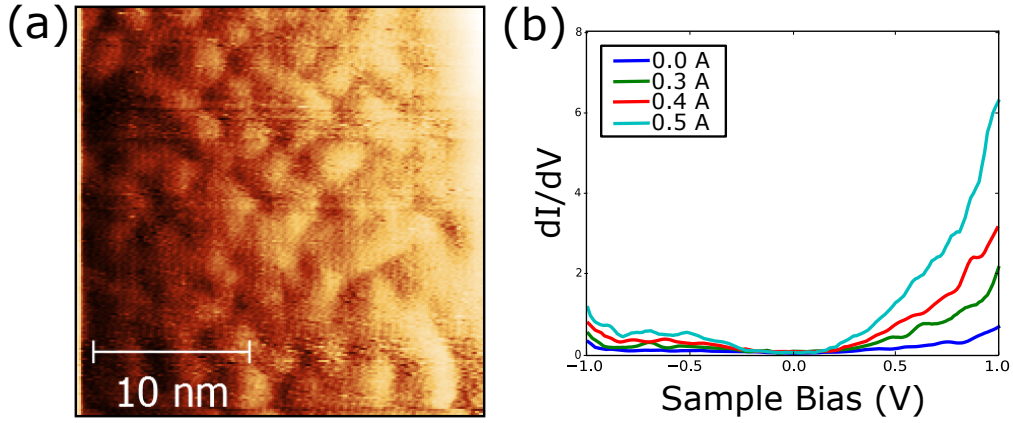

Figure 45: Averaged STS on a sidewall facet from 4HNNA. (a) Zooming in onto the sidewall facet, showing surface corrugations. (2.0 V, 50 pA). (b) Averaged spectra over the facet, which shows low differential conductance near the center roughly between -0.2 V and 0.2 V.

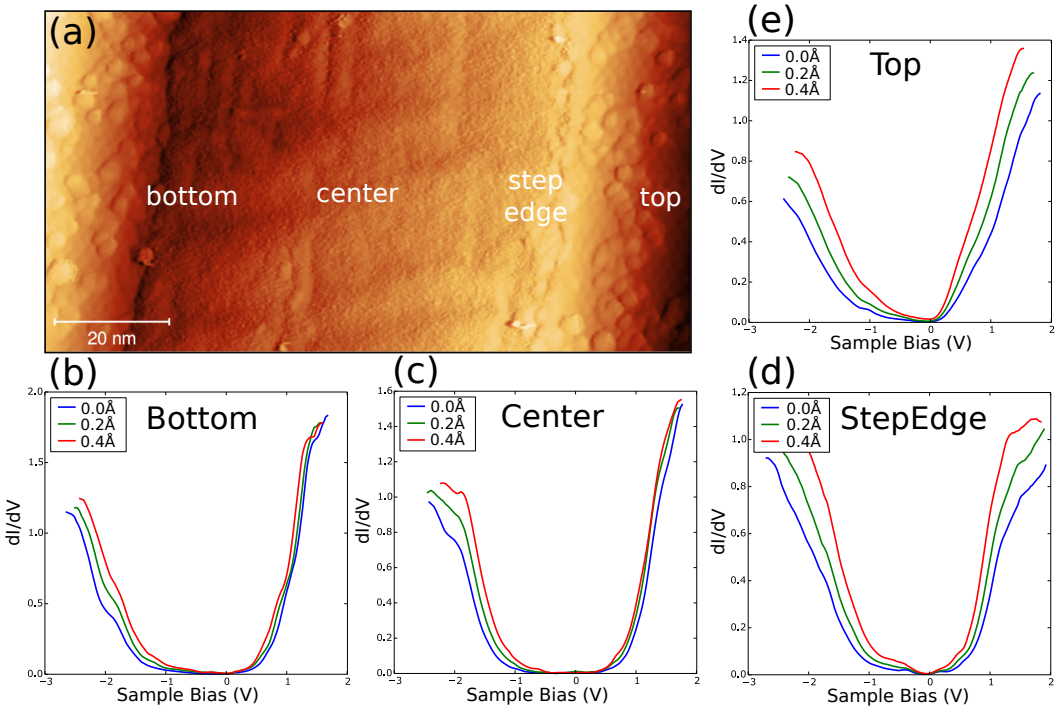

Figure 46: Averaged STS on a sidewall facet from T79. (a) A sidewall facet showing the bottom, center of the step, step edge, and the top terrace; facet appears to be smoother than the bottom and top of the step. (−2.5 V, 30 pA) (b) Averaged spectra near the bottom of the step, in similar shape to bulk graphene; (c) Averaged spectra in the middle of the step, showing ultra low LDOS around 0.0 eV. (d) Averaged spectra near the step edge, showing some kink features that indicate localized electronic states. (e) Averaged spectra over the top terrace near the step edge, it very much resembles data from a undoped monolayer graphene.

that graphene is electronically different on the sidewalls becoming more semiconducting; while away from the center of the nanofacets, their electronic properties convert to bulk graphene layers formed on SiC flat terraces possibly due to the different bonding with the substrate, strain, as well as confinement effects found near the step edges.

3.3 Buffer Layer

3.3.1 Surface Disordering

As most samples have only buffer layer graphene coverage except near the step edges, confirmed by the ($6\sqrt{3} \times 6\sqrt{3}\,\mathrm{R}30^\circ$) pattern in LEED and 6×6 reconstruction in STM, it is of great importance to understand the characteristics of such interfacial layer. However, it has been experimentally found that buffer layer graphene is usually bonded to the SiC substrate and insulating, it is usually difficult to directly image the buffer layer structures with high resolutions under STM [82, 83, 127, 187]. As can be seen in Fig. 33b, Fig. 31b, and Fig. 32c, buffer-layer regions (flat terraces away from the step edge) are usually covered with a disordered distribution of three-dimensional islands; more detailed images across different samples are listed in Fig. 47. It is important to note that such features are observed on all samples and they appear similarly in a more or less spherical shape and apparently sit on top of the buffer layer, although the density can vary from sample to sample and also region by region. On average each individual feature is around 2–6 nm in size laterally and 1–2 nm vertically. The best STM images so far seem to indicate that they are pretty uniformly formed (approximately) hemispheres and can be clustered together (Fig. 47b) scaling up to a few tens of nanometer in lateral size. Interestingly, these disordered features are not commonly seen near the step edges on the GNR samples where our measurements show graphene. While it is not yet clear what they consist of, AES results show carbon, silicon and some residual oxygen are the only chemical elements on the surface. Furthermore, XPS does not show exotic bond information either [222]. Therefore, the possible candidates are only among disordered silicon, silicon-related oxide, silicon carbide, special forms of carbon such as fullerene, and/or mixtures of all of them.

STS measurements are taken over such regions on HDS009, shown in Fig. 48. Figure 48a

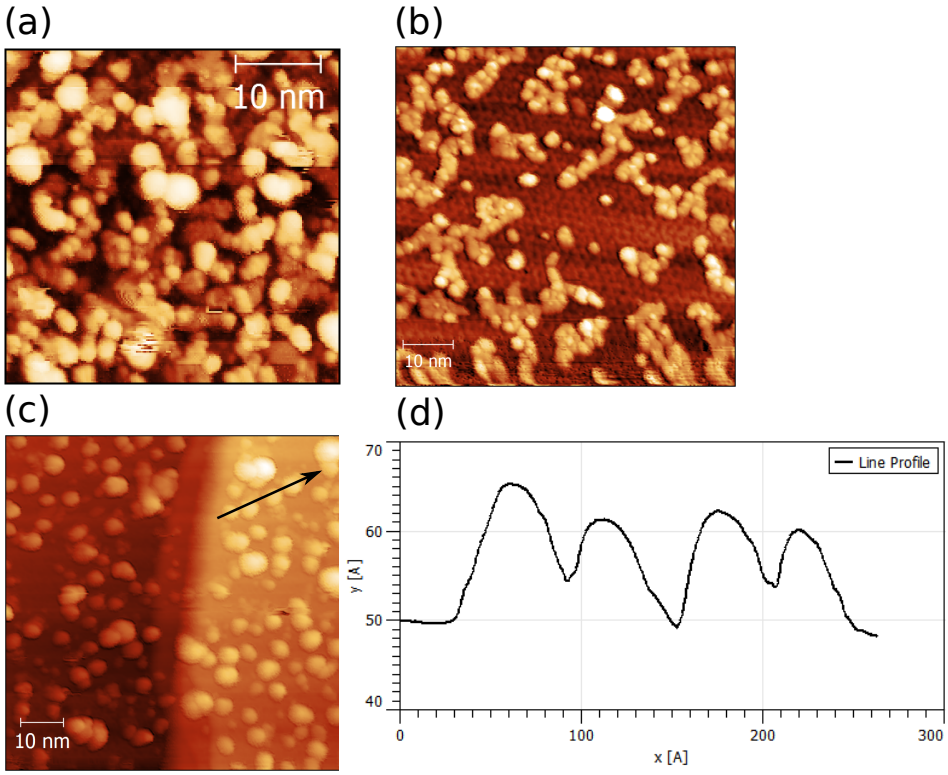

Figure 47: STM imaging on disordered buffer graphene layer across different samples. (a) Buffer layer on HDS009, density of particles is higher than the other samples. ($-1.0\,\mathrm{V}$, $50\,\mathrm{pA}$). (b) Buffer layer on T79, which appears to be clustered together and floating on top of clear SiC(6×6) patterns. ($-1.5\,\mathrm{V}$, $40\,\mathrm{pA}$). (c) Buffer layer on 4HNNA, particles are more separated from each other and the step edge in the middle has much lower density of particles ($2.0\,\mathrm{V}$, $50\,\mathrm{pA}$). (d) Line profile over the particles in c, showing their height and width roughly $1.5\,\mathrm{nm}$ and $5\,\mathrm{nm}$ respectively.

shows averaged STS spectra over all data points in the region shown in Fig. 48c. The spectra can be thought of as a mixture of two main types of spectrum observed on the surface shown in Fig. 48b. The red curve is more frequently observed which shows a shoulder around -0.7 eV, a signature of the Dirac point position, indicating a local n-type doping, whereas the blue curve shows a parabolic shape that resembles data from reconstructed SiC surface in ref.[84] and is often found right on the small spherical particles. If we map the averaged density of states around -0.7 eV into a 2D image (Figure 48d) and compare it with the topography (Figure 48c) taken simultaneously with the spectral data, it immediately shows that the shoulder feature(higher differential conductance colored in yellow) dominantly takes place in the interstices between particles and becomes weaker where those spheres reside.

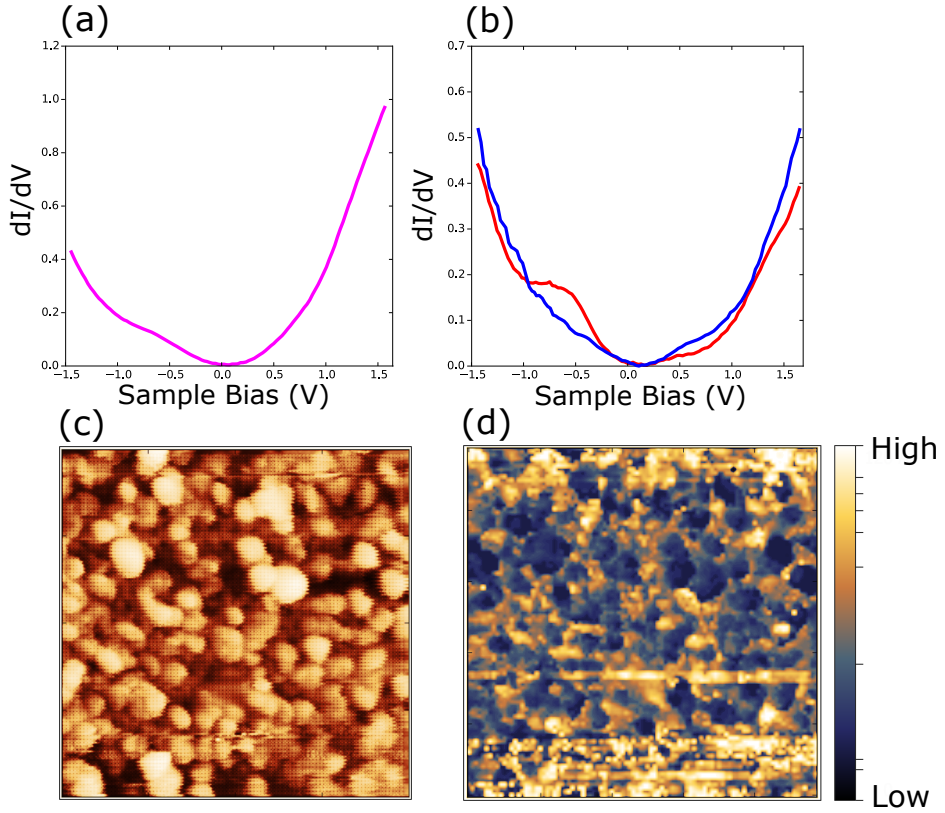

Figure 48: STS spectral mapping on a flat terrace on HDS009 covered with disordered particles. (a) Averaged STS spectra over the entire image show in c, a slight kink around -0.7 eV is observed. (b) Two main types of spectrum observed on the surface. The red curve exhibits a clear shoulder around -0.7 eV and is more frequently seen in this data set, while the blue curve follows a parabolic shape which is typically seen on top of the small particles in the topographic in c. (c) topography image, which is taken simultaneously as the STS spectrum are recorded at every other pixel locations. (d) Averaged STS spectral map between -0.6 V and -0.8 V corresponding to the dIdV shoulder just mentioned. Pixel intensity is proportional to the differential conductance measured by the dI/dV curves show in b. Apparently higher dI/dV conductance is mostly seen between the particle sites indicating that such shoulder feature is more prominent away from the particles.

Thus, it is reasonable to presume that the red curve in Fig. 48b is associated with the buffer layer graphene buried underneath and the blue curve is mostly from the particles implying SiC being one of their compositions.

STS measurements taken on other samples usually exhibits insulating characteristics with extremely low differential conductance between -1.0 eV and 1.0 eV in sample bias, without any anomaly features in the spectrum. It is possible that STM tip is not close enough to probe the LDOS with higher resolution since such data is usually taken at a fixed

height from the surface when the sample bias is higher than 2.5 V. In addition, STM imaging is only stable at such high sample biases. At low biases, significant tunneling noises are observed and the STM tip becomes highly unstable, an indication of touching the surface or picking up non-conductive molecules. At times, the ball-shaped features seems mobile as previously scanned square areas are seen from larger scale images and aggregations of them are also observed.

3.3.2 Further Discussions

Apparently, the additional layer of discorded covering is undesirable and could potentially affect the electronic behaviors of sidewall graphene in a unpredictable way. In order to reduce/eliminate such features, several experiments have been carried out. Although the efforts has not been successful in completely getting rid of the disordered layers, the results provides further understanding of them. Firstly, some samples are put into hydrofluoric acid in the aim of cleaning off silicon oxides, but no obvious changes are observed after the treatment. Samples also undergo different stages of heating from 500°C to 850°C and then up to 1300°C in the UHV system. It is found that all the disordered features after 850°C annealing for 20min become immobile on the surface and STM imaging becomes more stable while their density and size has not changed much. LEED measurements shows less diffusive background and AES results show that the previous residual oxygen peak is eliminated leaving only carbon and silicon signatures in the spectra. However, no further surface improvement is noticed for higher temperature annealing. Two different furnaces are used for graphitization, both showing such features on the surface although the density is a little different. Comparing to UHV grown buffer layer graphene, these samples are much more disordered whereas triangular symmetry and 6×6 reconstructions can be easily identified on the clean UHV buffer layers with very sparsely distributed sphere features. Despite of lack of strong evidence for revealing the true nature of the undesirable disorders introduced on the GNR samples, it is, based on the above experiments, believed that a mixture of different species are present on the surface with insulating properties. Oxide-related components and mobile molecules are avoidable after high temperature annealing,

but the leftover is stable on the surface and can not be easily etched away by HF. At this stage, a plausible conjecture is that atomic Si and C sublimated during graphene growth may reform small SiC molecules back deposited onto the surface and other C atoms could cluster together forming fullerene-like nano-particles sticking to the chemically reactive buffer layers [159]. For lithography-patterned GNR samples, residuals from the patterning process may contribute to formations of carbon-rich components on the surface. Unfortunately, it is difficult to identify the structure and composition of these features because it is highly likely that carbon and silicon are buried inside the particles while the substrate and graphene on top also contain substantial amount of those two species. In addition, some of the particles may well be similarly structured to SiC or sp^2-bonded graphitic carbon making it even more challenging to distinguish them from the rest of the surface. Therefore, normal macroscopic techniques will be unlikely to provide more information.

To further identify the structural details and reduce the coverage of these disordered features, additional microscopic measurements will be very helpful due to the non-uniform coverage of sidewall graphene, buffer layer, and the disordered phase. Micro-XPS and tip-enhanced Raman spectroscopy would be promising techniques that are able to provide local bonding and crystalline information on the surface. Careful preparation in the growth furnace like pre-growth high temperature outgassing and fine pressure control during the cooling process can possibly help to reduce formation of some of the undesirable disordering. Since the particles is not very conductive, HR-AFM is an option to directly probe its atomic structures without damaging the probe. Such measurement mode is available in the LT-STM system, but needs more calibration to be fully functional. TEM can also be helpful in looking at the cross sections of the surface to look for more structural information to see if there is any ordering within the individual particles. Another alternative would be pre-forming large step structures on the SiC substrate through either step-bunching in hydrogen etching or lithography patterning with careful subsequent cleaning and then in-situ growing GNRs in a UHV system integrated with STM and other measurement capabilities. However, graphene growth in UHV is known to be highly non-uniform due to the non-equilibrium sublimation process, therefore could lead to overgrown graphene layers near the step edges.

CHAPTER IV

CONCLUDING REMARKS

4.1 Summary of Results

In this thesis, I have introduced a unique 2D material, graphene. Its exceptional electronic properties have great potential in next generation semiconductor device applications, mainly due to its sp^2 hybridization and unique cone-shaped band structures at low energies. Based on literature review and experimental results, I have demonstrated that a particular form of graphene, namely the graphene nanoribbons, provides a promising route to introduce band gaps into the system with the ability to precisely control their size with the ribbon width and edge terminations, which is a crucial step before graphene can be commercially integrated into device fabrications. To better understand the physics involved in epitaxial graphene nanoribbons grown on SiC surfaces, I utilized several techniques for forming large step structures on SiC(0001) substrate including self-organized step-bunching on both on-axis and off-axis samples and lithography patterning of on-axis samples. Electrostatic Force Microscopy and Atomic Force Microscopy measurements confirm the formation of higher-than-10-nm sidewall facets on the surfaces. I have shown that Confinement Controlled Sublimation method, with tuned temperature and pressure parameters, limits graphene growth to only near the step edges while buffer layer graphene is mostly covering the rest of the sample surface. Low Energy Electron Diffraction patterns confirm good ordering on the samples up to 500 μm scale, with Auger Electron Spectroscopy estimating the thickness of graphene coverage to be mostly less than a monolayer. I conducted Scanning Tunneling Microscopy to study the structural details of sidewall formation and graphene growth which shows that the resulted large steps tend to consist of ministeps and graphene are typically found near the step edges growing continuously from the top terrace onto the faceted sidewalls, though with observable distortions in the lattice right on the edges. Flat

surfaces away from the step edges are typically covered by buffer layer graphene with significant disordered features formed on top. Scanning Tunneling Spectroscopy are utilized to study the electronic behaviors of different forms of graphene present on the samples. The detected discrete electronic states in the local density of states are associated with the strain effects present in the distorted graphene lattice. Additional results from other sidewall facets are also presented implying semiconducting properties of graphene formed there. Although strain effects and semiconducting graphene have been observed before, it has not been directly seen on the epitaxial sidewall Gr/SiC system at room temperatures. Results presented in this thesis demonstrate the rich physics underlying the epitaxial graphene on SiC that could lead to a better understanding of such system and bring alternative ways to controllably modify graphene's electronic properties.

Graphene typically grows faster on sidewall facets on the SiC surface serving as the foundation of utilizing this property for GNR formation. Self-organized step-bunching has proven to be able to reform surface steps into large sidewall structures which usually gives uniform, straight sidewall facets, although it produces a more uniformly distributed both in height and spatial locations on the off-axis substrates than on the on-axis ones. Lithography patterning is good for easily imposing large step structures with controllable heights, but usually suffers from more severe ministep formation and step direction wandering after high temperature annealing as shown by our STM results. Indeed, for well-formed sidewalls, they all relax into low energy facets with typical angles between 20° and 28° corresponding to low-index SiC crystal planes. Our results imply that self-organized step-bunching tend to give better sidewall formations with regard to completeness of faceting and stability of facet directions. Sidewall graphene is more easily identified by STM imaging on self-organized on-axis samples, where the imaged atomic lattices have confirmed continuous graphene formation from the top terrace onto the sidewall with significant distortions right near the bending edges. Such observations indicate a large amount of non-uniform strain present in these regions which is confirmed by local STS measurements. Series of discrete LDOS peaks are observed across different samples in graphene covered step edges, giving rise to the pseudo landau levels as strain introduces a pseudo magnetic field in graphene,

up to 400 T. Molecular Dynamics simulations further identify such strain effects coming dominantly from shearing and stretching of graphene lattice, rather than the curvature near the step edge. Additional observations of a large doping change of 0.4 eV over a 4 nm region giving a strong in-plane electric field about 0.01 V/Å near the step edge can also be partly attributed to the present strain since it is predicted to introduce extra electrostatic potential in graphene while another possibility is from the region-dependent interactions between graphene and the SiC substrate. Nonetheless, the varying doping level is potentially an important effect as a graphene $p-n$ junction near the step edge can be formed and lead to interesting transport characteristics. We also observed confinement effects in some of the GNRs implying a potentially bandgap feature in the STS spectra. Consistently, extremely low LDOS between -0.2 eV and 0.2 eV is found on sidewalls from off-axis and patterned surfaces, though no atomic images are obtained from these samples. Efforts are also put into characterizing the buffer layer region on flat terraces. However, disorders possibly from the high temperature growth process and exposure to ambient environment prohibits quantitative data collection and are difficult to eliminate in post-growth treatments.

Based on all the observations, we can conclude that sidewall graphene can grow continuously connecting the sidewall facets and the top flat terraces formed in multiple ways, resulting in atomically smooth edge terminations. In terms of step quality, natural step bunching seems to provide more uniform, larger step structures and sidewall graphene near the step edges can be more easily identified, in comparison to artificially imposed trench structures by e-beam lithography. Graphitization favors a narrow strip of the top terraces near step edges where the surface appear to be as smooth as the sidewall and graphene lattice has been directly imaged, but rough surface morphology on the bottom terrace connecting the sidewall facet suggests graphene growth may terminate at the connection region. Sidewall graphene, especially near the step edge, is electronically distinct from normal flat graphene systems. Effects including strain, confinement, substrate electrostatic potential, edge scattering, as well as interfacial buffer layer, all contribute to the unique electronic behaviors of graphene in such regions. The rich physics buried in this system opens up a variety of opportunities to manipulate the electronic structure of sidewall GNRs such

as bandgap engineering, strain engineering, and spin hall state engineering [207], just to name a few. Deviations in electronic structures from normal graphene to sidewall graphene might be able to explain the physical origins of the mysterious ballistic transport results along sidewall GNRs [5], despite that the phenomenon could be a mixture of various effects taking place both on the top terrace and the sidewall facts adjacent to the step edges. Strain effects in zigzag-terminated graphene may play an important role in lifting the spin degeneracy in the band structures. In the presence of enhanced spin-orbit coupling, spin is directly tied to the electron momentum which means edge channels propagating in different directions (clockwise and counter-clockwise) will have different spin orientations. As strain introduces a valley-dependent pseudo-magnetic field (opposite sign in K and K'), it increases the energy in one direction of edge channels while lowers the energy in the other, lifting the spin-degeneracy.

4.2 Future work

In future works, graphene will continue to be an active research field. Large-scale graphene growth with single/few domains and less defects, integration of graphene into current industry platforms, and further investigation of graphene's electronic structures proposing new analog device applications will be some of the most outstanding aspects of graphene-based research. In particular, epitaxial GNRs, as an important branch, suggests possibilities of making use of various quantum phenomenon in designing semiconductor devices. Further understanding of origins of GNRs' ballistic transport properties will be important in guiding novel device designs. Consistent bandgap engineering will be crucial in GNR-based device performances. Finally, high-density and high-quality GNR production will be the key to large scale commercial applications.

Based on the results from this thesis, several directions can be taken to better investigate the physical system. For the disorders on the buffer layer, a direct in-vacuum transfer of freshly prepared GNR sample for low-temperature STM would be extremely helpful in ruling out possibilities of contaminations from ambient environment. Low-temperature UHV system also helps to maintain a clean surface with minimal external deposition/adsorption

that could greatly affect imaging. In addition, growing graphene on the patterned or already step-bunched substrate in a UHV system would enable the comparison between UHV-grown and furnace-grown GNRs as UHV-grown buffer layer is known to be ordered and clean. Even with the already-grown samples, hydrogen intercalation can lift up the buffer layer saturating the dangling bonds to the substrate. A subsequent STM study could potentially show whether the observed large features will come off since now they are essentially attached to a quasi freestanding graphene layer which is chemically stable and usually stays clean. To reveal more detailed information about the sidewall graphene, HRTEM can help to provide atomic layer structures over the sidewall facets from thin sample slices, that way it can be easily seen how the top graphene layer changes from the top terraces all the way to the bottom of the step and also provide information about how the large features is connected to the underneath buffer layer. Adding light sources and collectors to the low-temperature STM makes possible tip-enhanced Raman spectroscopy measurements, which can provide nanometer-scale chemical and structural information that helps to identify what is covered on the surface. Raman spectral mapping is also possible with the STM imaging system that maps the phase distribution on samples.

More insights into the selective graphene growth on differently prepared surfaces are essential for achieving high-quality large-scale sidewall GNRs production. In particular, studying how natural step-bunching changes with respect to the surface starting condition, vicinal miscut angle, and growth temperature and time would help explain the variabilities in step heights and step splitting observed on sample HDS009 and T79, thus leading to reproducible uniform sidewall facets with controllable heights. Furthermore, it would also help to separate the growth process into two stages, hydrogen etching with step bunching and graphene growth respectively. This way it leaves more degrees of freedom to the latter growth stage. In addition, more careful design of the lithography process in terms of e-beam energy and direction, mask materials, and reactive etching conditions can greatly help to mitigate damages to the facet walls which is potentially affecting the graphene formation by changing the bonding geometry on the facets, and also to reduce carbon-rich residuals on the surface which partly contribute to the disorders on the terraces.

Apart from more detailed characterization of graphene formation, further experiments studying the electronic structures would also be important. As pseudo magnetic fields are observed on sidewall graphene, it would be very interesting to see their interaction with real magnetic field using STM equipped with superconducting magnets. Switching the direction of the magnetic field from being perpendicular to the substrate basal plane to the sidewall facets can record the changes in interaction between pseudo Landau levels. As the directions of the pseudo magnetic fields are opposite between the two valleys in reciprocal space, a potential splitting of the low-index Landau levels can be expected due to the valley polarization and the extrema magnitude of splitting can be possibly correlated to extrema of local strain gradient. Local transport measurement along the GNRs with multi-probe STM can potentially provide insightful understanding of the conducting channels in the system. A possible setup would be connecting the two ends of a GNR with two STM probes supplying current flow with a third tip in the middle changing both it lateral and horizontal positions to track the changes in current. Spin-polarized STM is another interesting measurement to consider. By injecting spin-polarized current into the sidewall GNRs, it is possible to find the magnetic states in the system and study the interaction between normal carrier transport and spin polarization.

APPENDIX A

PSXM FOR STM DATA ANALYSIS

The PSXM package is developed primarily for processing data collected from the room-temperature STM system using the *Python* programming language. It has capabilities to transform single data set for visualization, processing and analysis, but also supports processing data sets in batch mode for browsing through single image and spectroscopy data quickly. PSXM is command-line based so that functional calling and data transformation are fast and efficient. The *IPython Notebook* loaded with `matplotlib` and `numpy` is recommended as the best working environment. In addition, PSXM can also be easily extended by writing python scripts to facilitate processing a particular set of data.

A.1 Dependencies

The package is heavily dependent on various packages for array manipulation, visualization, image processing, and statistical analysis. The dependent packages needed to successfully run PSXM are listed as follows:

- `python 2`
- `numpy`
- `scipy`
- `matplotlib`
- `scikit-image`
- `ScientificPython` or `netCDF4`
- Bulit-in pakcages: `os, platform, system, time, pdb, math`

The code is written in python 2, although it should mostly working under python 3. Names and styles of functions of the dependent packages can be changing over time, therefore

it is worthwhile to look into the printed warnings when packages are firstly loaded. On Ubuntu Linux, it is recommended to use the *apt-get* command to install all needed packages. While on Windows, it is recommended to use the Anaconda distribution (free version) to automatically manage all package installations.

A.2 STM Data

All STM data are stored in the *.netcdf* format which provides self-description and efficient disk usage. Upon loaded into python via the netCDF interface, the data is stored as a python `dictionary` whose values can be accessed by the existing `keys`. The detailed structure and all relevant attributes of this data format can be found in the Excel table (*ncdata_struct.xls*) within the package directory. The actual numeric data points are all converted into `numpy.ndarray` in PSXM. It is worth pointing out that the meaning of each array dimension in the commonly used STM data types:

- image: `numpy.ndarray([biases, scan_direction, x, y])`
- spectroscopy: `numpy.ndarray([z_layers, scan_direction, pixel_location, current])`

A.3 Code Structure

Most useful codes are available from the root directory while customizable initialization and setup codes are stored in the *./shared* directory. Most of the time, the user will be interacting with the three most useful pieces of code:

- *./shared/setup.py*, for setting up raw data and processed data directories, data file naming conventions.
- *./view_spm.py*, for loading all relevant packages and the data set into the corresponding class under the PSXM framework.
- *./classes.py*, for accessing data information and calling analysis functions under different classes (STM data types).

A more detailed description of the code structure is listed in Fig. 49.

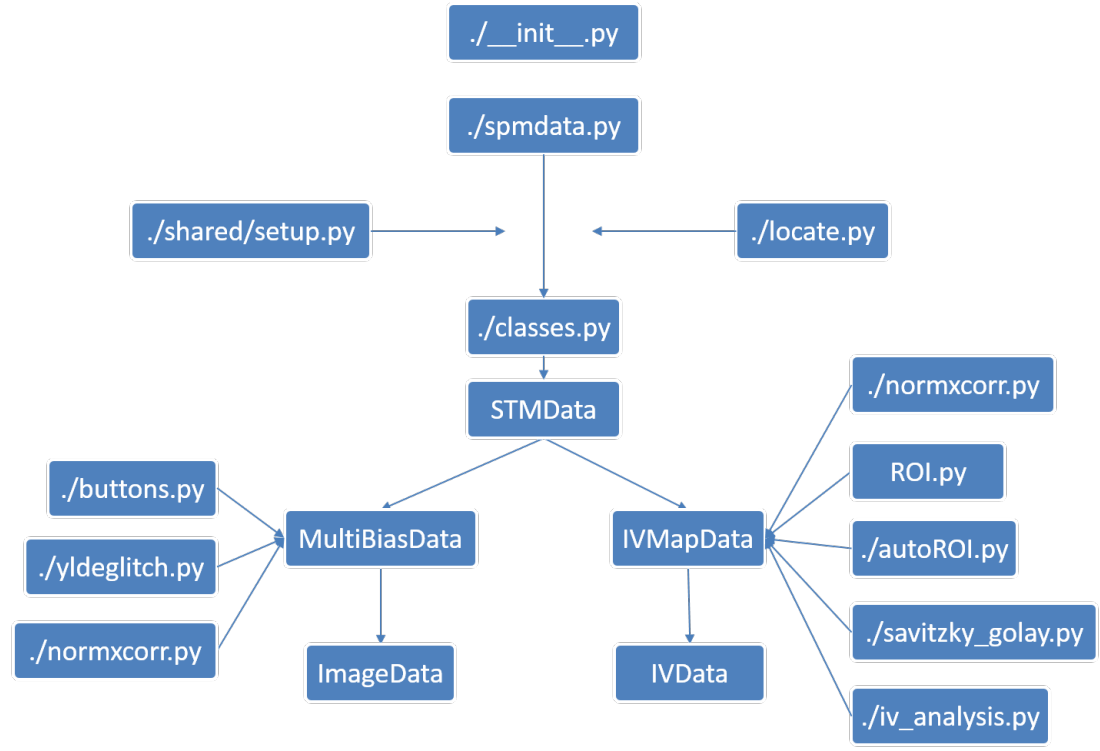

Figure 49: Code structure of the PSXM package. Arrows stand for `import` or class inheritance.

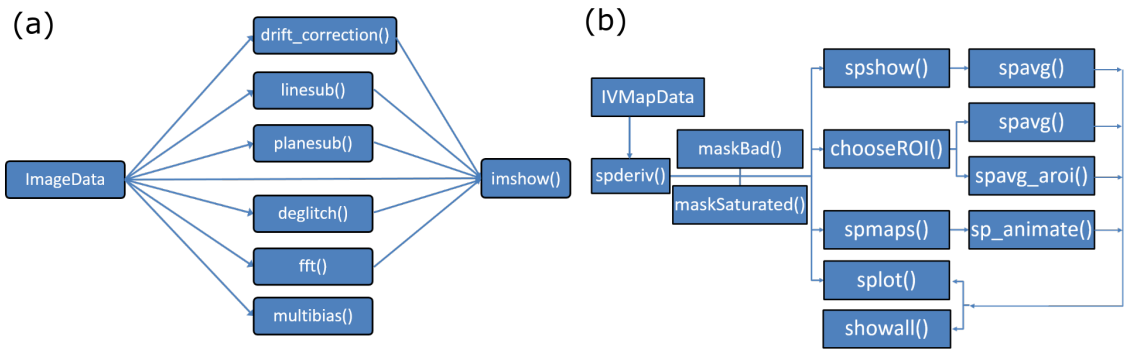

Figure 50: Workflow in PSXM. (a) to analyze image data, images are instantiated as the `ImageData` class, where different filtering and background fitting can be performed before viewing with `imshow()`. (b) dI/dV map data are instantiated as the `IVMapData` class, where different ways of analysis can be performed, as shown in the different paths in the figure.

A.4 Usage

The PSXM directory should be appended to the system path of python so that it can be easily accessed independent of the working directory under command line. Raw data

and processed data directories should be set up prior to loading the PSXM package. A particularly useful demonstration code `demo.py` can be found under the *./scripts/* directory. Other useful scripts for generating some of the results in this thesis is also included in the same directory.

the PSXM package should be first imported in order to use it. A file handler is then created by calling the `spmdata` function passing the numeric data ID. Entering the file handler by default prints relevant information about the data set. For example:

```
import view_spm as vs
f12345 = vs.spmdata(12345)
f12345
```

For image data, various basic processing functions are available such as plane subtraction (`planesub`), line subtraction (`linesub`), Fourier transformation (`fft`), scar removal (`deglitch`). The image can be visualized by the `imshow` function. In addition, for images taken at various biases at the same time, the `multibias` function generates a GUI that is designed to browse through the different biases and compare their differences. The workflow for processing image data is shown in Fig. 50a. More sophisticated image analysis can be acheived by combining PSXM and the Gwyddion software.

Point spectroscopy and dI/dV mapping can be processed easily with the `IVMapData` class. Since the RT-STM system only records $I-V$ data, numeric derivatives and smoothing have to be calculated using the $Savitizky-Golay$ filter (`spderiv()`). Inconsistent data points can be removed by `maskBad()` and `maskSaturated()`. Location-dependent spectroscopy data can be visualized by `spshow()`, where as the mouse moves around the topography image window, corresponding dI/dV and $I-V$ curves are rendered in a separate window, and LDOS map can also be separately plotted by clicking on specific energy positions. Averaging over regions of interest can be achieved by calling `chooseROI()` to draw the interested areas on screen and then using `spavg()` or `spavg_aroi()` to find the averaged spectra within the selected area. In addition, spectrum in the selected region of interest can be visualized against each other by `showall()`, which is also able to manually

remove individual bad data points and print their spatial locations. Spatial LDOS maps can be created by use of `spmaps()` and `sp_animate()`, which can average over a specified energy range and generate an animated window flipping through the different energies. `splot()` is particularly useful for plotting single spectra that results from the previous averaging procedures and different display modes can be specified. Possible workflow of analyzing spectroscopy data is shown in Fig. 50b.

More detailed documentations can be found in the source code of `classes.py`, or by simply typing `function_name?` in *IPython Notebook*.

A.5 Version Control

Currently, a Mercurial repository is set up for PSXM, one should have a local copy of the repository by cloning before starting extending its functionalities. For details of using Mercurial, please visit https://www.mercurial-scm.org/wiki/Mercurial. Simple and thorough tutorials can be found at URLs: http://hgbook.red-bean.com/ and http://hginit.com/.

Bibliography

[1] M. Schulz. "The end of the road for silicon?" *Nature* **399** (6738), 729–730 (1999).

[2] A. C. Ferrari, F. Bonaccorso, V. Fal'ko, K. S. Novoselov, S. Roche, P. Boggild, S. Borini, F. H. L. Koppens, V. Palermo, N. Pugno, J. A. Garrido, R. Sordan, A. Bianco, L. Ballerini, M. Prato, E. Lidorikis, J. Kivioja, C. Marinelli, T. Ryhanen, A. Morpurgo, J. N. Coleman, V. Nicolosi, L. Colombo, A. Fert, M. Garcia-Hernandez, A. Bachtold, G. F. Schneider, F. Guinea, C. Dekker, M. Barbone, Z. Sun, C. Galiotis, A. N. Grigorenko, G. Konstantatos, A. Kis, M. Katsnelson, L. Vandersypen, A. Loiseau, V. Morandi, D. Neumaier, E. Treossi, V. Pellegrini, M. Polini, A. Tredicucci, G. M. Williams, B. Hee Hong, J.-H. Ahn, J. Min Kim, H. Zirath, B. J. van Wees, H. van der Zant, L. Occhipinti, A. Di Matteo, I. A. Kinloch, T. Seyller, E. Quesnel, X. Feng, K. Teo, N. Rupesinghe, P. Hakonen, S. R. T. Neil, Q. Tannock, T. Lofwander, and J. Kinaret. "Science and technology roadmap for graphene, related two-dimensional crystals, and hybrid systems." *Nanoscale* **7**, 4598–4810 (2015).

[3] R. Mas-Balleste, C. Gomez-Navarro, J. Gomez-Herrero, and F. Zamora. "2D materials: to graphene and beyond." *Nanoscale* **3**, 20–30 (2011).

[4] A. H. Castro Neto, F. Guinea, N. M. R. Peres, K. S. Novoselov, and A. K. Geim. "The electronic properties of graphene." *Rev. Mod. Phys.* **81**, 109–162 (2009).

[5] J. Baringhaus, M. Ruan, F. Edler, A. Tejeda, M. Sicot, AminaTaleb-Ibrahimi, A.-P. Li, Z. Jiang, E. H. Conrad, C. Berger, C. Tegenkamp, and W. A. de Heer. "Exceptional ballistic transport in epitaxial graphene nanoribbons." *Nature* **506**, 349–354 (2014).

[6] K. S. Kim, Y. Zhao, H. Jang, S. Y. Lee, J. M. Kim, K. S. Kim, J.-H. Ahn, P. Kim, J.-Y. Choi, and B. H. Hong. "Large-scale pattern growth of graphene films for stretchable transparent electrodes." *Nature* **457** (7230), 706–710 (2009).

[7] K. P. Loh, Q. Bao, G. Eda, and M. Chhowalla. "Graphene oxide as a chemically tunable platform for optical applications." *Nature Chem.* **2** (12), 1015–1024 (2010).

[8] J.-H. Lee, E. K. Lee, W.-J. Joo, Y. Jang, B.-S. Kim, J. Y. Lim, S.-H. Choi, S. J. Ahn, J. R. Ahn, M.-H. Park, C.-W. Yang, B. L. Choi, S.-W. Hwang, and D. Whang. "Wafer-scale growth of single-crystal monolayer graphene on reusable hydrogen-terminated germanium." *Science* (2014).

[9] European Commission. "Graphene Flagship Project." `http://graphene-flagship.eu/`.

[10] K. S. Novoselov, V. I. Fal[prime]ko, L. Colombo, P. R. Gellert, M. G. Schwab, and K. Kim. "A roadmap for graphene." *Nature* **490** (7419), 192–200 (2012).

[11] J. Hicks, A. Tejeda, A. Taleb-Ibrahimi, M. S. Nevius, F. Wang, K. Shepperd, J. Palmer, F. Bertran, P. Le Fevre, J. Kunc, W. A. de Heer, C. Berger, and E. H. Conrad. "A wide-bandgap metal-semiconductor-metal nanostructure made entirely from graphene." *Nature Phys.* **9** (1), 49–54 (2013).

[12] M. S. Nevius, M. Conrad, F. Wang, A. Celis, M. N. Nair, A. Taleb-Ibrahimi, A. Tejeda, and E. H. Conrad. "Semiconducting graphene from highly ordered substrate interactions." *Phys. Rev. Lett.* **115**, 136 802 (2015).

[13] P. R. Wallace. "The band theory of graphite." *Phys. Rev.* **71** (9), 622–634 (1947).

[14] A. K. Geim and K. S. Novoselov. "The rise of graphene." *Nat. Mater.* **6** (3), 183–191 (2007).

[15] C. Berger, Z. Song, T. Li, X. Li, A. Y. Ogbazghi, R. Feng, Z. Dai, A. N. Marchenkov, E. H. Conrad, P. N. First, and W. A. de Heer. "Ultrathin epitaxial graphite: 2D electron gas properties and a route toward graphene-based nanoelectronics." *J. Phys. Chem. B* **108**, 19 912 (2004).

[16] M. S. D. R Saito, G Dresselhaus. *Physical Properties of Carbon Nanotubes* (Imperial College Press, 1998).

[17] R. C. Tatar and S. Rabii. "Electronic properties of graphite: A unified theoretical study." *Phys. Rev. B* **25**, 4126–4141 (1982).

[18] A. Bostwick, T. Ohta, T. Seyller, K. Horn, and E. Rotenberg. "Quasiparticle dynamics in graphene." *Nature Phys.* **3** (1), 36–40 (2007).

[19] V. W. Brar. *Scanning Tunneling Spectroscopy of Graphene and Magnetic Nanostructures.* Ph.D. thesis, UC Berkeley (2010).

[20] K. F. Mak, C. H. Lui, J. Shan, and T. F. Heinz. "Observation of an electric-field-induced band gap in bilayer graphene by infrared spectroscopy." *Phys. Rev. Lett.* **102**, 256 405 (2009).

[21] N. Levy, S. A. Burke, K. L. Meaker, M. Panlasigui, A. Zettl, F. Guinea, A. H. C. Neto, and M. F. Crommie. "Strain-induced pseudo-magnetic fields greater than 300 Tesla in graphene nanobubbles." *Science* **329** (5991), 544–547 (2010).

[22] A. L. Kitt, V. M. Pereira, A. K. Swan, and B. B. Goldberg. "Lattice-corrected strain-induced vector potentials in graphene." *Phys. Rev. B* **85**, 115 432 (2012).

[23] M. Vozmediano, M. Katsnelson, and F. Guinea. "Gauge fields in graphene." *Phys. Rep.* **496** (45), 109 – 148 (2010).

[24] J. V. Sloan, A. A. P. Sanjuan, Z. Wang, C. Horvath, and S. Barraza-Lopez. "Strain gauge fields for rippled graphene membranes under central mechanical load: An approach beyond first-order continuum elasticity." *Phys. Rev. B* **87**, 155 436 (2013).

[25] H. Yan, Y. Sun, L. He, J. C. Nie, and M. H. W. Chan. "Observation of Landau-level-like quantization at 77 K along a strained-induced graphene ridge." *Phys. Rev. B* **85** (3), 035 422 (2012).

[26] K. S. Novoselov, A. K. Geim, S. V. Morozov, D. Jiang, Y. Zhang, S. V. Dubonos, I. V. Grigorieva, and A. A. Firsov. "Electric field effect in atomically thin carbon films." *Science* **306** (5696), 666–669 (2004).

[27] M. Ishigami, J. H. Chen, W. G. Cullen, M. S. Fuhrer, , and E. D. Williams. "Atomic structure of graphene on SiO_2." *Nano Lett.* **7** (6), 1643–1648 (2007). PMID: 17497819.

[28] M. Yi and Z. Shen. "A review on mechanical exfoliation for the scalable production of graphene." *J. Mater. Chem. A* **3**, 11 700–11 715 (2015).

[29] Y. Zhang, V. W. Brar, C. Girit, A. Zettl, and M. F. Crommie. "Origin of spatial charge inhomogeneity in graphene." *Nature Phys.* **5** (10), 722–726 (2009).

[30] S. Cho and M. Fuhrer. "Massless and massive particle-in-a-box states in single- and bi-layer graphene." *Nano Research* **4** (4), 385–392 (2011).

[31] K. I. Bolotin, F. Ghahari, M. D. Shulman, H. L. Stormer, and P. Kim. "Observation of the fractional quantum hall effect in graphene." *Nature* **462** (7270), 196–199 (2009).

[32] C. R. Dean, A. F. Young, P. Cadden-Zimansky, L. Wang, H. Ren, K. Watanabe, T. Taniguchi, P. Kim, J. Hone, and K. L. Shepard. "Multicomponent fractional quantum hall effect in graphene." *Nature Phys.* **7** (9), 693–696 (2011).

[33] L. Wang, I. Meric, P. Y. Huang, Q. Gao, Y. Gao, H. Tran, T. Taniguchi, K. Watanabe, L. M. Campos, D. A. Muller, J. Guo, P. Kim, J. Hone, K. L. Shepard, and C. R. Dean. "One-dimensional electrical contact to a two-dimensional material." *Science* **342** (6158), 614–617 (2013).

[34] M. Batzill. "The surface science of graphene: Metal interfaces, CVD synthesis, nanoribbons, chemical modifications, and defects." *Surf. Sci. Rep.* **67** (34), 83 – 115 (2012).

[35] European Commission. "GRAFOL Project." `http://www.grafol.eu/`.

[36] D. R. Cooper, B. DAnjou, N. Ghattamaneni, B. Harack, M. Hilke, A. Horth, N. Majlis, M. Massicotte, L. Vandsburger, E. Whiteway, and V. Yu. "Experimental review of graphene." (2012).

[37] D. C. Marcano, D. V. Kosynkin, J. M. Berlin, A. Sinitskii, Z. Sun, A. Slesarev, L. B. Alemany, W. Lu, and J. M. Tour. "Improved synthesis of graphene oxide." *ACS Nano* **4** (8), 4806–4814 (2010). PMID: 20731455.

[38] C. K. Chua and M. Pumera. "Chemical reduction of graphene oxide: a synthetic chemistry viewpoint." *Chem. Soc. Rev.* **43**, 291–312 (2014).

[39] D. A. Sokolov. *Investigation Of Graphene Formation From Graphite Oxide And Silicon Carbide*. Ph.D. thesis, Georgia Institute of Technology (2013).

[40] M. Ruan, Y. Hu, Z. Guo, R. Dong, J. Palmer, J. Hankinson, C. Berger, and W. A. de Heer. "Epitaxial graphene on silicon carbide: Introduction to structured graphene." *MRS Bulletin* **37**, 1138–1147 (2012).

[41] J. Wood (2011). Lyding Research Group, Beckman Institute.

[42] H.-W. Chu. *Development Of Solution-Processed Methods For Graphene Synthesis And Device Fabrication*. Ph.D. thesis, Georgia Institute of Technology (2011).

[43] A. V. Bommel, J. Crombeen, and A. V. Tooren. "LEED and Auger electron observations of the SiC(0001) surface." *Surf. Sci.* **48** (2), 463 – 472 (1975).

[44] A. Bostwick, F. Speck, T. Seyller, K. Horn, M. Polini, R. Asgari, A. H. MacDonald, and E. Rotenberg. "Observation of plasmarons in quasi-freestanding doped graphene." *Science* **328** (5981), 999–1002 (2010).

[45] A. Bostwick, T. Ohta, J. L. McChesney, T. Seyller, K. Horn, and E. Rotenberg. "Renormalization of graphene bands by many-body interactions." *Solid State Commun.* **143** (1-2), 63–71 (2007).

[46] A. Bostwick, T. Ohta, J. L. McChesney, T. Seyller, K. Horn, and E. Rotenberg. "Band structure and many body effects in graphene." *European Physical Journal-Special Topics* **148**, 5–13 (2007).

[47] A. Bostwick, T. Ohta, J. L. McChesney, K. V. Emtsev, T. Seyller, K. Horn, and E. Rotenberg. "Symmetry breaking in few layer graphene films." *New J. Phys.* **9**, 385 (2007).

[48] A. Bostwick, T. Ohta, T. Seyller, K. Horn, and E. Rotenberg. "Experimental determination of the spectral function of graphene." *arXiv* (2007).

[49] C. Dimitrakopoulos, Y.-M. Lin, A. Grill, D. B. Farmer, M. Freitag, Y. Sun, S.-J. Han, Z. Chen, K. A. Jenkins, Y. Zhu, Z. Liu, T. J. McArdle, J. A. Ott, R. Wisnieff, and P. Avouris. "Wafer-scale epitaxial graphene growth on the Si-face of hexagonal SiC(0001) for high frequency transistors." *Journal of Vacuum Science & Technology B* **28** (5), 985–992 (2010).

[50] E. Pallecchi, F. Lafont, V. Cavaliere, F. Schopfer, D. Mailly, W. Poirier, and A. Ouerghi. "High electron mobility in epitaxial graphene on 4H-SiC(0001) via post-growth annealing under hydrogen." *Sci. Rep.* **4**, 4558– (2014).

[51] X. Wu, Y. Hu, M. Ruan, N. K. Madiomanana, J. Hankinson, M. Sprinkle, C. Berger, and W. A. de Heer. "Anomalous quantum hall effect in epitaxial graphene." *arXiv* (2009).

[52] P. N. First, W. A. de Heer, T. Seyller, C. Berger, J. A. Stroscio, and J.-S. Moon. "Epitaxial graphenes on silicon carbide." *MRS Bulletin* **35**, 296–305 (2010).

[53] Y.-W. Son, M. L. Cohen, and S. G. Louie. "Energy gaps in graphene nanoribbons." *Phys. Rev. Lett.* **97**, 216 803 (2006).

[54] V. Barone, O. Hod, and G. E. Scuseria. "Electronic structure and stability of semiconducting graphene nanoribbons." *Nano Lett.* **6** (12), 2748–2754 (2006). PMID: 17163699.

[55] M. Fujita, K. Wakabayashi, K. Nakada, and K. Kusakabe. "Peculiar localized state at zigzag graphite edge." *J. Phys. Soc. Jpn.* **65**, 1920 (1996).

[56] K. Nakada, M. Fujita, G. Dresselhaus, and M. S. Dresselhaus. "Edge state in graphene ribbons: Nanometer size effect and edge shape dependence." *Phys. Rev. B* **54** (24), 17 954–17 961 (1996).

[57] O. V. Yazyev. "A guide to the design of electronic properties of graphene nanoribbons." *Acc. Chem. Res.* **46** (10), 2319–2328 (2013). PMID: 23282074.

[58] D. S. L. Abergel, V. Apalkov, J. Berashevich, K. Ziegler, and T. Chakraborty. "Properties of graphene: a theoretical perspective." *Adv. Phys.* **59** (4), 261–482 (2010).

[59] A. R. Akhmerov, J. H. Bardarson, A. Rycerz, and C. W. J. Beenakker. "Theory of the valley-valve effect in graphene nanoribbons." *Phys. Rev. B* **77**, 205 416 (2008).

[60] G. Z. Magda, X. Jin, I. Hagymasi, P. Vancso, Z. Osvath, P. Nemes-Incze, C. Hwang, L. P. Biro, and L. Tapaszto. "Room-temperature magnetic order on zigzag edges of narrow graphene nanoribbons." *Nature* **514** (7524), 608–611 (2014).

[61] L. Tapaszto, G. Dobrik, P. Lambin, and L. P. Biro. "Tailoring the atomic structure of graphene nanoribbons by scanning tunnelling microscope lithography." *Nat Nano* **3** (7), 397–401 (2008).

[62] L. Jiao, L. Zhang, X. Wang, G. Diankov, and H. Dai. "Narrow graphene nanoribbons from carbon nanotubes." *Nature* **458** (7240), 877–880 (2009).

[63] M. Y. Han, J. C. Brant, and P. Kim. "Electron transport in disordered graphene nanoribbons." *Phys. Rev. Lett.* **104**, 056 801 (2010).

[64] D. V. Kosynkin, A. L. Higginbotham, A. Sinitskii, J. R. Lomeda, A. Dimiev, B. K. Price, and J. M. Tour. "Longitudinal unzipping of carbon nanotubes to form graphene nanoribbons." *Nature* **458** (7240), 872–876 (2009).

[65] R. M. Jacobberger, B. Kiraly, M. Fortin-Deschenes, P. L. Levesque, K. M. McElhinny, G. J. Brady, R. Rojas Delgado, S. Singha Roy, A. Mannix, M. G. Lagally, P. G. Evans, P. Desjardins, R. Martel, M. C. Hersam, N. P. Guisinger, and M. S. Arnold. "Direct oriented growth of armchair graphene nanoribbons on germanium." *Nature Comm.* **6**, – (2015).

[66] C. Tao, L. Jiao, v. O. V. Yazye, Y.-C. Chen, J. Feng, X. Zhang, R. B. Capaz, J. M. Tour, A. Zettl, S. G. Louie, H. Dai, and M. F. Crommie. "Spatially resolving edge states of chiral graphene nanoribbons." *Nature Phys.* **7**, 616 (2011).

[67] Y.-C. Chen, D. G. De Oteyza, Z. Pedramrazi, C. Chen, F. R. Fischer, and M. F. Crommie. "Tuning the band gap of graphene nanoribbons synthesized from molecular precursors." *ACS nano* **7** (7), 6123–6128 (2013).

[68] M. Sprinkle, M. Ruan, Y. Hu, J. Hankinson, M. Rubio-Roy, B. Zhang, X. Wu, C. Berger, and W. A. de Heer. "Scalable templated growth of graphene nanoribbons on SiC." *Nat Nano* **5** (10), 727–731 (2010).

[69] M. S. Nevius, F. Wang, C. Mathieu, N. Barrett, A. Sala, T. O. Mente, A. Locatelli, and E. H. Conrad. "The bottom-up growth of edge specific graphene nanoribbons." *Nano Lett.* **14** (11), 6080–6086 (2014). PMID: 25254434.

[70] C. Davisson and L. H. Germer. "Diffraction of electrons by a crystal of nickel." *Phys. Rev.* **30**, 705–740 (1927).

[71] N. J. Taylor. "Resolution and sensitivity considerations of an Auger electron spectrometer based on display LEED optics." *Rev. Sci. Instrum.* **40** (6), 792–804 (1969).

[72] J. Hass, W. A. de Heer, and E. H. Conrad. "The growth and morphology of epitaxial multilayer graphene." *J. Phys.: Condens. Matter* **20** (32), 323 202 (2008).

[73] T. Li. *Characteristics Of Graphite Films On Silicon- And Carbon- Terminated Faces Of Silicon Carbide*. Ph.D. thesis, Georgia Institute of Technology (2006).

[74] L. Scudiero. "MatS571-Lecture - Auger Electron Spectroscopy (AES) Scanning Auger Microscopy (SAM)." Technical report, Washington State University (2014).

[75] P. E. Industries. *Handbook of Auger Electron Spectroscopy* (Physical Electronics, 1972).

[76] RHK-Technology. *User's Guides - SPM 1000, XPM Pro, PPC 200*. RHK, http://www.rhk-tech.com/r9/.

[77] D. L. Miller. *Atomic-Scale Spectroscopy and Mapping of Magnetic States in Epitaxial Graphene*. Ph.D. thesis, Georgia Institute of Technology (2010). Thesis should be available online Spring, 2011.

[78] A. J. Melmed. "The art and science and other aspects of making sharp tips." *Journal of Vacuum Science & Technology B* **9** (2), 601–608 (1991).

[79] M. Kulawik, M. Nowicki, G. Thielsch, L. Cramer, H.-P. Rust, H.-J. Freund, T. P. Pearl, and P. S. Weiss. "A double lamellae dropoff etching procedure for tungsten tips attached to tuning fork atomic force microscopy/scanning tunneling microscopy sensors." *Rev. Sci. Instrum.* **74** (2), 1027–1030 (2003).

[80] A. N. Chaika, N. N. Orlova, V. N. Semenov, E. Y. Postnova, S. A. Krasnikov, M. G. Lazarev, S. V. Chekmazov, V. Y. Aristov, V. G. Glebovsky, S. I. Bozhko, and I. V. Shvets. "Fabrication of [001]-oriented tungsten tips for high resolution scanning tunneling microscopy." *Sci. Rep.* **4**, 3742– (2014).

[81] M. MORGENSTERN. "Probing the local density of states of dilute electron systems in different dimensions." *Surf. Rev. Lett.* **10** (06), 933–962 (2003).

[82] N. Sharma. *Microscopic and Spectroscopic Studies of Growth and Electronic Structure of Epitaxial Graphene*. Ph.D. thesis, Georgia Institute of Technology (2009).

[83] S. Goler, C. Coletti, V. Piazza, P. Pingue, F. Colangelo, V. Pellegrini, K. V. Emtsev, S. Forti, U. Starke, F. Beltram, and S. Heun. "Revealing the atomic structure of the buffer layer between SiC(0001) and epitaxial graphene." *Carbon* **51**, 249 – 254 (2013).

[84] G. M. Rutter, N. P. Guisinger, J. N. Crain, P. N. First, and J. A. Stroscio. "Edge structure of epitaxial graphene islands." *Phys. Rev. B* **81** (24), 245 408– (2010).

[85] S. Nie and R. M. Feenstra. "Tunneling spectroscopy of graphene and related reconstructions on SiC(0001)." *Journal of Vacuum Science & Technology A* **27** (4), 1052–1057 (2009).

[86] J. S. Alden, A. W. Tsen, P. Y. Huang, R. Hovden, L. Brown, J. Park, D. A. Muller, and P. L. McEuen. "Strain solitons and topological defects in bilayer graphene." *Proceedings of the National Academy of Sciences* **110** (28), 11 256–11 260 (2013).

[87] P. B. Allen. "Interpreting the 4-index notation for hexagonal systems." (2010).

[88] T. Ando. "Exotic electronic and transport properties of graphene." *Physica E-Low-Dimensional Systems & Nanostructures* **40** (2), 213–227 (2007).

[89] T. Ando. "Screening effect and impurity scattering in monolayer graphene." *J. Phys. Soc. Jpn.* **75** (7), 074 716 (2006).

[90] D. A. Areshkin, D. Gunlycke, and C. T. White. "Ballistic transport in graphene nanostrips in the presence of disorder: Importance of edge effects." *Nano Lett.* **7**, 204 (2007).

[91] S. Bala Kumar, T. Fujita, and G. Liang. "Conductance modulation in graphene nanoribbon under transverse asymmetric electric potential." *J. Appl. Phys.* **109** (7), 073704 (2011).

[92] E. Bekyarova, M. E. Itkis, P. Ramesh, C. Berger, M. Sprinkle, W. A. De Heer, and R. C. Haddon. "Chemical modification of epitaxial graphene: Spontaneous grafting of aryl groups." *J. Am. Chem. Soc.* **131** (4), 1336–1337 (2009).

[93] C. Berger, Z. Song, X. Li, X. Wu, N. Brown, C. Naud, D. Mayou, T. Li, J. Hass, A. N. Marchenkov, E. H. Conrad, P. N. First, and W. A. de Heer. "Electronic confinement and coherence in patterned epitaxial graphene." *Science* **312** (5777), 1191–1196 (2006).

[94] F. Bonaccorso, Z. Sun, T. Hasan, and A. C. Ferrari. "Graphene photonics and optoelectronics." *Nat. Photonics* **4**, 611 (2010).

[95] V. Borovikov and A. Zangwill. "Step bunching of vicinal 6H-SiC{0001} surfaces." *Phys. Rev. B* **79** (24), 245 413–9 (2009).

[96] V. Borovikov and A. Zangwill. "Step-edge instability during epitaxial growth of graphene from SiC(0001)." *Phys. Rev. B* **80** (12), 121 406–4 (2009).

[97] L. Britnell, R. V. Gorbachev, R. Jalil, B. D. Belle, F. Schedin, A. Mishchenko, T. Georgiou, M. I. Katsnelson, L. Eaves, and S. V. Morozov. "Field-effect tunneling transistor based on vertical graphene heterostructures." *Science* **335**, 947 (2012).

[98] J. S. Bunch, A. M. van der Zande, S. S. Verbridge, I. W. Frank, D. M. Tanenbaum, J. M. Parpia, H. G. Craighead, and P. L. McEuen. "Electromechanical resonators from graphene sheets." *Science* **315** (5811), 490–493 (2007).

[99] J. Cai, P. Ruffieux, R. Jaafar, M. Bieri, T. Braun, S. Blankenburg, M. Muoth, A. P. Seitsonen, M. Saleh, X. Feng, K. Mullen, and R. Fasel. "Atomically precise bottom-up fabrication of graphene nanoribbons." *Nature* **466** (7305), 470–473 (2010).

[100] C. Chen, S. Lee, V. V. Deshpande, G.-H. Lee, M. Lekas, K. Shepard, and J. Hone. "Graphene mechanical oscillators with tunable frequency." *Nat Nano* **8** (12), 923–927 (2013).

[101] C. J. Chen. *Introduction to Scanning Tunneling Microscopy* (Oxford University Press, 1993).

[102] Y. Chen, T. Jayasekera, and A. Calzolari. "Thermoelectric properties of graphene nanoribbons, junctions and superlattices." *J. Phys.: Condens. Matter* **22**, 372 202 (2010).

[103] Z. Chen, Y. M. Lin, M. J. Rooks, and P. Avouris. "Graphene nano-ribbon electronics." *Physica E* **40**, 228 (2007).

[104] J. Chung, J. Chen, P.-K. Ko, C. Hu, and M. Levi. "The effects of low-angle off-axis substrate orientation on mosfet performance and reliability." *Electron Devices, IEEE Transactions on* **38** (3), 627–633 (1991).

[105] C. Cocchi, A. Ruini, D. Prezzi, M. J. Caldas, and E. Molinari. "Designing all-graphene nanojunctions by covalent functionalization." *J. Phys. Chem. C* **115**, 2969 (2011).

[106] A. Cresti and S. Roche. "Edge-disorder-dependent transport length scales in graphene nanoribbons: From Klein defects to the superlattice limit." *Phys. Rev. B* **79**, 233 404 (2009).

[107] P. Darancet, N. Wipf, C. Berger, W. A. de Heer, and D. Mayou. "Quenching of the quantum Hall effect in multilayered epitaxial graphene: The role of undoped planes." *Phys. Rev. Lett.* **101** (11), 116806 (2008).

[108] S. Das Sarma, S. Adam, E. H. Hwang, and E. Rossi. "Electronic transport in two-dimensional graphene." *Rev. Mod. Phys.* **83**, 407–470 (2011).

[109] W. DeHeer, C. Berger, and P. First. "Patterned thin film graphite devices and method for making same." (2006). US Patent 7,015,142.

[110] A. Dyrdał, J. Barnaś, and V. K. Dugaev. "Current-induced spin polarization in graphene due to Rashba spin-orbit interaction." *Phys. Rev. B* **89**, 075 422 (2014).

[111] K. V. Emtsev, A. Bostwick, K. Horn, J. Jobst, G. L. Kellogg, L. Ley, J. L. McChesney, T. Ohta, S. A. Reshanov, J. Rohrl, E. Rotenberg, A. K. Schmid, D. Waldmann, H. B. Weber, and T. Seyller. "Towards wafer-size graphene layers by atmospheric pressure graphitization of silicon carbide." *Nat. Mater.* **8** (3), 203–207 (2009).

[112] K. V. Emtsev, F. Speck, T. Seyller, L. Ley, and J. D. Riley. "Interaction, growth, and ordering of epitaxial graphene on SiC{0001} surfaces: A comparative photoelectron spectroscopy study." *Phys. Rev. B* **77**, 155 303 (2008).

[113] D. Faria, A. Latgé, S. E. Ulloa, and N. Sandler. "Currents and pseudomagnetic fields in strained graphene rings." *Phys. Rev. B* **87**, 241 403 (2013).

[114] N. Ferralis, R. Maboudian, and C. Carraro. "Evidence of structural strain in epitaxial graphene layers on 6h-sic(0001)." *Phys. Rev. Lett.* **101**, 156 801 (2008).

[115] F. Giannazzo, I. Deretzis, G. Nicotra, G. Fisichella, Q. Ramasse, C. Spinella, F. Roccaforte, and A. L. Magna. "High resolution study of structural and electronic properties of epitaxial graphene grown on off-axis 4H-SiC (0001)." *Journal of Crystal Growth* **393**, 150 – 155 (2014). The 19th American Conference on Crystal Growth and Epitaxy in conjunction with The 16th {US} Biennial Workshop on Organometallic Vapor Phase Epitaxy.

[116] G. Giavaras, P. Maksym, and M. Roy. "Electron confinement in single layer graphene quantum dots: Semiclassical approach." *Physica E* **42** (4), 715 – 718 (2010). 18th International Conference on Electron Properties of Two-Dimensional Systems.

[117] F. Guinea. "Charge distribution and screening in layered graphene systems." *Phys. Rev. B* **75** (23), 235 433 (2007).

[118] F. Guinea, M. I. Katsnelson, and M. A. H. Vozmediano. "Midgap states and charge inhomogeneities in corrugated graphene." *Phys. Rev. B* **77**, 075 422 (2008).

[119] N. P. Guisinger, G. M. Rutter, J. N. Crain, C. Heiliger, P. N. First, and J. A. Stroscio. "Atomic-scale investigation of graphene formation on 6H-SiC(0001)." *J. Vac. Sci. Technol. A* **26** (4), 932–937 (2008).

[120] Z. Guo. "graphene transport measurement on T79." Unpublished.

[121] V. P. Gusynin and S. G. Sharapov. "Unconventional integer quantum Hall effect in graphene." *Phys. Rev. Lett.* **95** (14), 146801 (2005).

[122] S. K. Hämäläinen, Z. Sun, M. P. Boneschanscher, A. Uppstu, M. Ijäs, A. Harju, D. Vanmaekelbergh, and P. Liljeroth. "Quantum-confined electronic states in atomically well-defined graphene nanostructures." *Phys. Rev. Lett.* **107**, 236 803 (2011).

[123] M. Y. Han, B. zyilmaz, Y. Zhang, and P. Kim. "Energy band-gap engineering of graphene nanoribbons." *Phys. Rev. Lett.* **98**, 206 805 (2007).

[124] J. B. Hannon and R. M. Tromp. "Pit formation during graphene synthesis on SiC(0001): In situ electron microscopy." *Phys. Rev. B* **77** (24), 241 404–4 (2008).

[125] J. Hass, R. Feng, T. Li, X. Li, Z. Song, W. A. de Heer, P. N. First, E. H. Conrad, C. A. Jeffrey, and C. Berger. "Highly ordered graphene for two dimensional electronics." *Appl. Phys. Lett.* **89** (14), 143106 (2006).

[126] J. Hass, F. Varchon, J. E. Millán-Otoya, M. Sprinkle, W. A. de Heer, C. Berger, P. N. First, L. Magaud, and E. H. Conrad. "Rotational stacking and its electronic effects on graphene films grown on 4H-SiC(000$\bar{1}$)." *Phys. Rev. Lett.* (2007).

[127] J. R. Hass. *Structural Characterization of Epitaxial Graphene on Silicon Carbide.* Ph.D. thesis, Georgia Institute of Technology (2008).

[128] W. A. de Heer. "The development of epitaxial graphene for 21st century electronics." *MRS Bulletin* **36** (633) (2011).

[129] W. A. de Heer, C. Berger, M. Ruan, M. Sprinkle, X. Li, Y. Hu, B. Zhang, J. Hankinson, and E. Conrad. "Large area and structured epitaxial graphene produced by confinement controlled sublimation of silicon carbide." *Proceedings of the National Academy of Sciences* **108** (41), 16 900–16 905 (2011).

[130] W. A. de Heer, C. Berger, X. Wu, P. N. First, E. H. Conrad, X. Li, T. Li, M. Sprinkle, J. Hass, M. L. Sadowski, M. Potemski, and G. Martinez. "Epitaxial graphene." *Solid State Commun.* **143**, 92–100 (2007).

[131] W. A. de Heer, C. Berger, X. Wu, M. Sprinkle, Y. Hu, M. Ruan, J. A. Stroscio, P. N. First, R. Haddon, B. Piot, C. Faugeras, M. Potemski, and J.-S. Moon. "Epitaxial graphene electronic structure and transport." *J. Phys. D* **43** (37), 374 007 (2010).

[132] V. Heine, C. Cheng, and R. J. Needs. "The preference of silicon carbide for growth in the metastable cubic form." *J. Am. Ceram. Soc.* **74** (10), 2630–2633 (1991).

[133] D. J. Hornbaker. *Electronic Structure of Carbon Nanotube Systems Measured with Scanning Tunneling Microscopy.* Ph.D. thesis, University of Illinois at Urbana-Champaign (2003).

[134] T. W. Hu, F. Ma, D. Y. Ma, D. Yang, X. T. Liu, K. W. Xu, and P. K. Chu. "Evidence of atomically resolved 6×6 buffer layer with long-range order and short-range disorder during formation of graphene on 6H-SiC by thermal decomposition." *Appl. Phys. Lett.* **102** (17), 171910 (2013).

[135] B. Huang, Q.-m. Yan, Z.-y. Li, and W.-h. Duan. "Towards graphene nanoribbon-based electronics." *Frontiers of Physics in China* **4** (3), 269–279 (2009).

[136] H. Huang, D. Wei, J. Sun, S. L. Wong, Y. P. Feng, A. H. C. Neto, and A. T. S. Wee. "Spatially resolved electronic structures of atomically precise armchair graphene nanoribbons." *Sci. Rep.* **2**, – (2012).

[137] A. Jablonski and C. J. Powell. "The electron attenuation length revisited." *Surf. Sci. Rep.* **47** (2), 33–91 (2002).

[138] N. Jain. "Sensitivity factors for $kl2,3l2,3$ transitions for light elements in *auger* electron spectroscopy." *J. Electron Spectrosc. Relat. Phenom.* **48** (1), 203–208 (1989).

[139] Z. Jiang, E. A. Henriksen, L. C. Tung, Y.-J. Wang, M. E. Schwartz, M. Y. Han, P. Kim, and H. L. Stormer. "Infrared Spectroscopy of Landau Levels of Graphene." *Phys. Rev. Lett.* **98** (19), 197403 (2007).

[140] W. Jolie, F. Craes, M. Petrović, N. Atodiresei, V. Caciuc, S. Blügel, M. Kralj, T. Michely, and C. Busse. "Confinement of Dirac electrons in graphene quantum dots." *Phys. Rev. B* **89**, 155 435 (2014).

[141] R. B. Kaner. "Honeycomb carbon: A review of graphene." *Chem. Rev.* **110**, 132 – 145 (2010).

[142] J. Kedzierski, P. L. Hsu, P. Healey, P. W. Wyatt, C. L. Keast, M. Sprinkle, C. Berger, and W. A. de Heer. "Epitaxial graphene transistors on SiC substrates." **55** (8), 2078–2085 (2008).

[143] T. Kimoto, A. Itoh, and H. Matsunami. "Step bunching in chemical vapor deposition of 6H- and 4H-SiC on vicinal SiC(0001) faces." *Appl. Phys. Lett.* **66** (26), 3645–3647 (1995).

[144] T. Kimoto, A. Itoh, H. Matsunami, and T. Okano. "Step bunching mechanism in chemical vapor deposition of 6H- and 4H-SiC{0001}." *J. Appl. Phys.* **81** (8), 3494–3500 (1997).

[145] M. Kindermann and P. N. First. "Local sublattice-symmetry breaking in rotationally faulted multilayer graphene." *Phys. Rev. B* **83** (4), 045 425 (2011).

[146] Y. Kopelevich and P. Esquinazi. "Graphene physics in graphite." *Adv. Mat.* **19** (24), 4559–4563 (2007).

[147] K. D. Kubista. *Local Measurements of Cyclotron States In Graphene*. Ph.d., Georgia Institute of Technology, Physics (2011).

[148] P. Lauffer, K. V. Emtsev, R. Graupner, T. Seyller, L. Ley, S. A. Reshanov, and H. B. Weber. "Atomic and electronic structure of few-layer graphene on SiC(0001) studied with scanning tunneling microscopy and spectroscopy." *Phys. Rev. B* **77**, 155 426 (2008).

[149] X. Li, X. Wu, M. Sprinkle, F. Ming, M. Ruan, Y. Hu, C. Berger, and W. A. de Heer. "Top and side gated epitaxial graphene field effect transistors." *Phys. Status Solidi A* **207** (2), 286–290 (2010).

[150] Y. Y. Li, M. X. Chen, t. M. Weiner, and L. Li. "Direct experimental determination of onset of electronelectron interactions in gap opening of zigzag graphene nanoribbons." *Nature Comm.* **5**, 4311 (2014).

[151] M. F. Lin and K. W. K. Shung. "Screening of charged impurities in graphite-intercalation compounds." *Phys. Rev. B* **46** (19), 12 656–12 663 (1992).

[152] T. Low and F. Guinea. "Strain-induced pseudomagnetic field for novel graphene electronics." *Nano Lett.* **10** (9), 3551–3554 (2010). PMID: 20715802.

[153] J. L. Mañes. "Symmetry-based approach to electron-phonon interactions in graphene." *Phys. Rev. B* **76**, 045 430 (2007).

[154] A. Mahmood, P. Mallet, and J.-Y. Veuillen. "Quasiparticle scattering off phase boundaries in epitaxial graphene." *Nanotechnology* **23** (5), 055 706 (2012).

[155] P. Mallet, F. Varchon, C. Naud, L. Magaud, C. Berger, and J.-Y. Veuillen. "Electron states of mono- and bilayer graphene on SiC probed by scanning-tunneling microscopy." *Phys. Rev. B* **76**, 041 403 (2007).

[156] T. Maruyama and S. Naritsuka. "Initial growth process of carbon nanotubes in surface decomposition of SiC." In D. S. Yellampalli, editor, "Carbon Nanotubes - Synthesis, Characterization, Applications," p. 999 (InTech, 2011).

[157] T. Mashoff, M. Pratzer, V. Geringer, T. J. Echtermeyer, M. C. Lemme, M. Liebmann, and M. Morgenstern. "Bistability and oscillatory motion of natural nanomembranes appearing within monolayer graphene on silicon dioxide." *Nano Letters* **10** (2), 461–465 (2010). PMID: 20058873.

[158] M. R. Masir, D. Moldovan, and F. Peeters. "Pseudo magnetic field in strained graphene: Revisited." *Solid State Communications* **175176**, 76 – 82 (2013). Special Issue: Graphene V: Recent Advances in Studies of Graphene and Graphene analogues.

[159] P. Merino, M. vec, J. Martinez, P. Jelinek, P. Lacovig, M. Dalmiglio, S. Lizzit, P. Soukiassian, J. Cernicharo, and J. Martin-Gago. "Graphene etching on SiC grains as a path to interstellar polycyclic aromatic hydrocarbons formation." *Nature Comm.* **5**, – (2014).

[160] F. Ming and A. Zangwill. "Model and simulations of the epitaxial growth of graphene on non-planar 6H-SiC surfaces." *J. Phys. D: Appl. Phys.* **45** (15), 154 007 (2012).

[161] M. Neek-Amal and F. M. Peeters. "Strain-engineered graphene through a nanostructured substrate. i. deformations." *Phys. Rev. B* **85**, 195 445 (2012).

[162] J. F. Nicholas. "The indexing of hexagonal crystals." *Phys. Status Solidi A* **1** (3), 563–571 (1970).

[163] S. Nie and R. Feenstra. "Scanning tunnenling spectroscopy of oxidized 6H-SiC surfaces." *Materials Science Forum* **527-529**, 1023–1026 (2006).

[164] S. Nie, C. Lee, R. Feenstra, Y. Ke, R. Devaty, W. Choyke, C. Inoki, T. Kuan, and G. Gu. "Step formation on hydrogen-etched 6H-SiC{0001} surfaces." *Surf. Sci.* **602** (17), 2936 – 2942 (2008).

[165] W. Norimatsu and M. Kusunoki. "Transitional structures of the interface between graphene and 6H-SiC(0001)." *Chem. Phys. Lett.* **468**, 52 (2009).

[166] A. Y. Ogbazghi. *Conductance through Nanometer-scale Metal-to-Graphite Contacts.* Ph.D. thesis, Georgia Institute of Technology (2005).

[167] N. Ohtani, M. Katsuno, J. Takahashi, H. Yashiro, and M. Kanaya. "Evolution of macrosteps on $6H-\mathrm{SiC}(0001)$: impurity-induced morphological instability of step trains." *Phys. Rev. B* **59**, 4592–4595 (1999).

[168] M. H. Oliveira, T. Schumann, M. Ramsteiner, J. M. J. Lopes, and H. Riechert. "Influence of the silicon carbide surface morphology on the epitaxial graphene formation." *Appl. Phys. Lett.* **99** (11), 111901 (2011).

[169] M. Ostler, I. Deretzis, S. Mammadov, F. Giannazzo, G. Nicotra, C. Spinella, T. Seyller, and A. La Magna. "Direct growth of quasi-free-standing epitaxial graphene on nonpolar SiC surfaces." *Phys. Rev. B* **88**, 085 408 (2013).

[170] I. Palacio, A. Celis, M. N. Nair, A. Gloter, A. Zobelli, M. Sicot, D. Malterre, M. S. Nevius, W. A. de Heer, C. Berger, E. H. Conrad, A. Taleb-Ibrahimi, and A. Tejeda. "Atomic structure of epitaxial graphene sidewall nanoribbons: Flat graphene, miniribbons, and the confinement gap." *Nano Lett.* **15** (1), 182–189 (2015). PMID: 25457853.

[171] C. Park, H. Yang, A. J. Mayne, G. Dujardin, S. Seo, Y. Kuk, J. Ihm, and G. Kim. "Formation of unconventional standing waves at graphene edges by valley mixing and pseudospin rotation." *Proceedings of the National Academy of Sciences* **108** (46), 18 622–18 625 (2011).

[172] V. M. Pereira, A. H. Castro Neto, and N. M. R. Peres. "Tight-binding approach to uniaxial strain in graphene." *Phys. Rev. B* **80**, 045 401 (2009).

[173] S. Plimpton. "Fast parallel algorithms for short-range molecular dynamics." *Journal of Computational Physics* **117** (1), 1 – 19 (1995).

[174] G. Prakash, M. A. Capano, M. L. Bolen, D. Zemlyanov, and R. G. Reifenberger. "{AFM} study of ridges in few-layer epitaxial graphene grown on the carbon-face of 4hsic." *Carbon* **48** (9), 2383 – 2393 (2010).

[175] D. Prezzi, D. Varsano, A. Ruini, and E. Molinari. "Quantum dot states and optical excitations of edge modulated graphene nanoribbons." *Phys. Rev. B* **84**, 041 401 (2011).

[176] D. Querlioz, Y. Apertet, A. Valentin, K. Huet, A. Bournel, S. Galdin-Retailleau, and P. Dollfus. "Suppression of the orientation effects on bandgap in graphene nanoribbons in the presence of edge disorder." *Appl. Phys. Lett.* **92**, 042 108 (2008).

[177] M. Ridene, T. Wassmann, E. Pallecchi, G. Rodary, J. C. Girard, and A. Ouerghi. "Epitaxial graphene on step bunching of a 6H-SiC(0001) substrate: Aromatic ring pattern and van hove singularities." *Appl. Phys. Lett.* **102** (11), 111610 (2013).

[178] C. Riedl, U. Starke, J. Bernhardt, and M. Franke. "Structural properties of the graphene-SiC(0001) interface as a key for the preparation of homogeneous large-terrace graphene surfaces." *Phys. Rev. B* **76**, 245 406 (2007).

[179] J. Robinson, X. Weng, K. Trumbull, R. Cavalero, M. Wetherington, E. Frantz, M. LaBella, Z. Hughes, M. Fanton, and D. Snyder. "Nucleation of epitaxial graphene on SiC(0001)." *ACS Nano* **4** (1), 153–158 (2010). PMID: 20000439.

[180] J. Rhrl, M. Hundhausen, K. V. Emtsev, T. Seyller, R. Graupner, and L. Ley. "Raman spectra of epitaxial graphene on sic(0001)." *Applied Physics Letters* **92** (20), 201918 (2008).

[181] E. Rotenberg. "Electronic structure of graphene on single-crystal copper substrates." *Phys. Rev. B* **84**, 195 443 (2011).

[182] M. Ruan. *Structured Epitaxial Graphene for Electronics.* Ph.D. thesis, Georgia Institute of Technology (2013).

[183] P. Ruffieux, J. Cai, N. C. Plumb, L. Patthey, D. Prezzi, A. Ferretti, E. Molinari, X. Feng, K. Mllen, C. A. Pignedoli, and R. Fasel. "Electronic structure of atomically precise graphene nanoribbons." *ACS Nano* **6** (8), 6930–6935 (2012). PMID: 22853456.

[184] G. M. Rutter. *Atomic Scale Properties of Epitaxial Graphene grown on SiC(0001).* Ph.D. thesis, Georgia Institute of Technology (2008).

[185] G. M. Rutter, J. N. Crain, N. P. Guisinger, P. N. First, and J. A. Stroscio. "Structural and electronic properties of bilayer epitaxial graphene." *J. Vac. Sci. Technol. A* **26** (4), 938–943 (2008).

[186] G. M. Rutter, J. N. Crain, N. P. Guisinger, T. Li, P. N. First, and J. A. Stroscio. "Scattering and interference in epitaxial graphene." *Science* **317**, 219–22 (2007).

[187] G. M. Rutter, N. P. Guisinger, J. N. Crain, E. A. A. Jarvis, M. D. Stiles, T. Li, P. N. First, and J. A. Stroscio. "Imaging the interface of epitaxial graphene with silicon carbide via scanning tunneling microscopy." *Phys. Rev. B* **76**, 235 416 (2007).

[188] J. Sabio, C. Seoanez, S. Fratini, F. Guinea, A. H. C. Neto, and F. Sols. "Electrostatic interactions between graphene layers and their environment." *Phys. Rev. B* **77** (19), 195 409–8 (2008).

[189] N. Sharma, D. Oh, H. Abernathy, M. Liu, P. N. First, and T. M. Orlando. "Signatures of epitaxial graphene grown on Si-terminated 6H-SiC(0001)." *Surf. Sci.* **604** (2), 84 – 88 (2010).

[190] F. Sols, F. Guinea, and A. H. CastroNeto. "Coulomb blockade in graphene nanoribbons." *Phys. Rev. Lett.* **99**, 166 803 (2007).

[191] Y. Son, M. Cohen, and S. Louie. "Half-metallic graphene nanoribbons." *Nature* **444**, 347 (2006).

[192] Y. L. Song, Y. Zhang, J. M. Zhang, and D. B. Lu. "Effects of the edge shape and the width on the structural and electronic properties of silicene nanoribbons." *Appl. Surf. Sci.* **256** (21), 6313–6317 (2010).

[193] M. Sprinkle, D. Siegel, Y. Hu, J. Hicks, A. Tejeda, A. Taleb-Ibrahimi, P. Le Fevre, F. Bertran, S. Vizzini, H. Enriquez, S. Chiang, P. Soukiassian, C. Berger, W. A. de Heer, A. Lanzara, and E. H. Conrad. "First direct observation of a nearly ideal graphene band structure." *Phys. Rev. Lett.* **103** (22), 226 803 (2009).

[194] M. Sprinkle, P. Soukiassian, W. A. de Heer, C. Berger, and E. H. Conrad. "Epitaxial graphene: the material for graphene electronics." *Phys. Status Solidi Rapid Res. Lett.* **3** (6), A91–A94 (2009).

[195] S. J. Stuart, A. B. Tutein, and J. A. Harrison. "A reactive potential for hydrocarbons with intermolecular interactions." *The Journal of Chemical Physics* **112** (14), 6472–6486 (2000).

[196] M. Syvjrvi, R. Yakimova, and E. Janzn. "Step-bunching in SiC epitaxy: anisotropy and influence of growth temperature." *Journal of Crystal Growth* **236** (13), 297 – 304 (2002).

[197] M. L. Teague, A. P. Lai, J. Velasco, C. R. Hughes, A. D. Beyer, M. W. Bockrath, C. N. Lau, and N. C. Yeh. "Evidence for strain-induced local conductance modulations in single-layer graphene on SiO_2." *Nano Lett.* **9** (7), 2542–2546 (2009).

[198] A. Tejeda, A. Taleb-Ibrahimi, W. de Heer, C. Berger, and E. H. Conrad. "Electronic structure of epitaxial graphene grown on the C-face of SiC and its relation to the structure." *New J. Phys.* **14**, 125 007 (2012).

[199] J. Tersoff and D. R. Hamann. "Theory of the scanning tunneling microscope." *Phys. Rev. B* **31**, 805–813 (1985).

[200] J. Tian, H. Cao, W. Wu, Q. Yu, and Y. P. Chen. "Direct imaging of graphene edges: Atomic structure and electronic scattering." *Nano Lett.* **11** (9), 3663–3668 (2011). PMID: 21806044.

[201] A. Tiberj, J.-R. Huntzinger, J. Camassel, F. Hiebel, A. Mahmood, P. Mallet, C. Naud, and J.-Y. Veuillen. "Multiscale investigation of graphene layers on 6H-SiC(000-1)." *Nanoscale Research Letters* **6** (1), 171 (2011).

[202] C. Vecchio, S. Sonde, C. Bongiorno, M. Rambach, R. Yakimova, V. Raineri, and F. Giannazzo. "Nanoscale structural characterization of epitaxial graphene grown on off-axis 4H-SiC(0001)." *Nanoscale Research Letters* **6** (1), 1–7 (2011).

[203] M. A. H. Vozmediano, F. de Juan, and A. Cortijo. "Gauge fields and curvature in graphene." *Journal of Phys.-Conf.* **129** (1), 012 001 (2008).

[204] P. Wagner, C. Ewels, V. Ivanovskaya, P. Briddon, A. Pateau, and B. Humbert. "Ripple edge engineering of graphene nanoribbons." *Phys. Rev. B* **84**, 134 110 (2011).

[205] K. Wakabayashi, M. Fujita, H. Ajiki, and M. Sigrist. "Electronic and magnetic properties of nanographite ribbons." *Phys. Rev. B* **59**, 8271 (1999).

[206] F. Wang, K. Shepperd, J. Hicks, M. S. Nevius, H. Tinkey, A. Tejeda, A. Taleb-Ibrahimi, F. Bertran, P. Le Fvre, D. B. Torrance, P. N. First, W. A. de Heer, A. A. Zakharov, and E. H. Conrad. "Silicon intercalation into the graphene-SiC interface." *Phys. Rev. B* **85** (16), 165 449– (2012).

[207] C. Weeks, J. Hu, J. Alicea, M. Franz, and R. Wu. "Publisher's note: Engineering a robust quantum spin hall state in graphene via adatom deposition." *Phys. Rev. X* **2**, 029 901 (2012).

[208] J.-H. Wong, B.-R. Wu, and M.-F. Lin. "Strain effect on the electronic properties of single layer and bilayer graphene." *J. Phys. Chem. C* **116**, 8271 (2012).

[209] W. Wulfhekel, D. Sander, S. Nitsche, F. Dulot, A. Leycuras, and M. Hanbücken. "Regular step formation on concave-shaped surfaces on 6H-SiC(0001)." *Surf. Sci.* **550**, 8–14 (2004).

[210] W. Wulfhekel, D. Sander, S. Nitsche, F. Dulot, A. Leycuras, and M. Hanbücken. "Structural reorganisation of vicinal surfaces on 6H-SiC(0001) induced by hot hydrogen etching." *Appl. Surf. Sci.* **234**, 251–255 (2004).

[211] Z. Yan, J. Lin, Z. Peng, Z. Sun, Y. Zhu, L. Li, C. Xiang, E. L. Samuel, C. Kittrell, and J. M. Tour. "Toward the synthesis of wafer-scale single-crystal graphene on copper foils." *ACS Nano* **6**, 9110 (2012).

[212] H. Yang, A. J. Mayne, M. Boucherit, G. Comtet, G. Dujardin, and Y. Kuk. "Quantum interference channeling at graphene edges." *Nano Lett.* **0** (proofing), null (2010).

[213] N.-C. Yeh, M.-L. Teague, S. Yeom, B. Standley, R.-P. Wu, D. Boyd, and M. Bockrath. "Strain-induced pseudo-magnetic fields and charging effects on CVD-grown graphene." *Surf. Sci.* **605** (1718), 1649 – 1656 (2011). Graphene Surfaces and Interfaces.

[214] D. Yoon, Y.-W. Son, and H. Cheong. "Negative thermal expansion coefficient of graphene measured by raman spectroscopy." *Nano Letters* **11** (8), 3227–3231 (2011). PMID: 21728349.

[215] L. M. Zhang and M. M. Fogler. "Nonlinear screening and ballistic transport in a graphene p-n junction." *Phys. Rev. Lett.* **100** (11), 116 804 (2008).

[216] R. Zhang, Y. Dong, W. Kong, W. Han, P. Tan, Z. Liao, X. Wu, and D. Yu. "Growth of large domain epitaxial graphene on the C-face of SiC." *J. Appl. Phys.* **112** (10), 104307 (2012).

[217] Y. Zhang, L. Zhang, and C. Zhou. "Review of chemical vapor deposition of graphene and related applications." *Acc. Chem. Res.* **46** (10), 2329–2339 (2013). PMID: 23480816.

[218] S. Y. Zhou, G.-H. Gweon, A. V. Fedorov, P. N. First, W. A. de Heer, D.-H. Lee, F. Guinea, A. H. Castro Neto, and A. Lanzara. "Substrate-induced bandgap opening in epitaxial graphene." *Nat. Mater.* **6** (10), 770–775 (2007).

[219] S. Zhu, Y. Huang, N. N. Klimov, D. B. Newell, N. B. Zhitenev, J. A. Stroscio, S. D. Solares, and T. Li. "Pseudomagnetic fields in a locally strained graphene drumhead." *Phys. Rev. B* **90**, 075 426 (2014).

[220] S. Zhu and T. Li. "Molecular dynamics simulation studying the origins of pseudo magnetic fields in sidewall graphene." Unpublished.

[221] S. Zhu, J. A. Stroscio, and T. Li. "Programmable extreme pseudomagnetic fields in graphene by a uniaxial stretch." *Phys. Rev. Lett.* **115**, 245 501 (2015).

[222] Matthew Conrad conducted the measurement.

[223] Samples were patterned by Jeremy Hicks (4HPGNR), Meredith Nevius (4HNNA), James Palmer (EDJP1, EDJP2). Graphene growth was done by Jeremy Hicks (4HPGNR), Meredith Nevius (HDS009, HDS002, 4HNNA), James Palmer (EDJP1, EDJP2), Baiqian Zhang (25ed30), Zelei Guo (T79).

VITA

Yuntao Li was born in Wuhan, China. As a naughty kid, he enjoyed playing hard on the soccer field, in the swimming pool, and on the stage along with his fellow clarinet enthusiasts. He only started feeling related to science when he accidentally participated in a provincial level physics contest and luckily got a prize. Ever since then, he has been eager to study every new concept in the textbook and took every chance to break into the high school physics lab to play with what he believed the 'big toys'. After the National College Entrance Exam, he enrolled as a freshman in physics at University of Science and Technology of China. In college, two important courses, computational physics and modern experimental techniques in condensed matter physics, made profound influences on Yuntao when he became intrigued in the idea of combining experiments and computers, though he wasn't even sure what that actually meant. Curious about what real research looks like and what the western world stands for, he joined Dr. First's lab in School of Physics at Georgia Tech shortly after his undergraduate study. He spent five years trying to identify atoms on various kinds of surfaces and enjoyed the process of uncovering anomaly features and fixing equipments, though not always as exciting and successful as expected. After his PhD, Yuntao will move to Chicago beginning a brand new endeavor exploring what would happen when data meets science.